DOCTORAL THESIS

Simulation and Modeling of Droplet Formation in Flash Atomization of Cryogenic Rocket Propellants

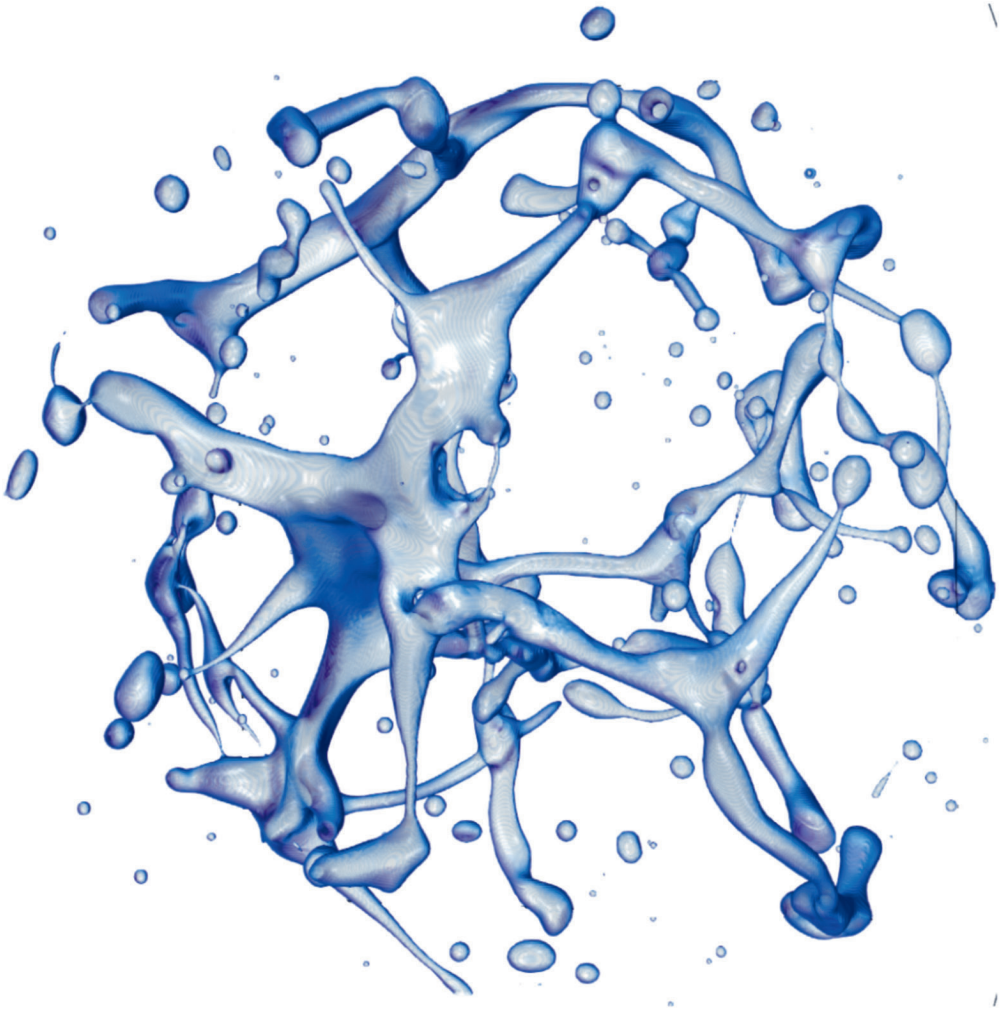

Daniel Dias Loureiro

2024

University of Stuttgart
Institute for Combustion Technology (ITV)

Simulation and Modeling of Droplet Formation in Flash Atomization of Cryogenic Rocket Propellants

von der
Fakultät Energie-, Verfahrens- und Biotechnik
der Universität Stuttgart
zur Erlangung der Würde eines
Doktors der Ingenieurwissenschaften
(Dr.-Ing.) genehmigte Abhandlung

vorgelegt von
Daniel Dias Loureiro
aus Espinho, Portugal

Hauptberichter:	Prof. Dr. Andreas Kronenburg
Mitberichter:	Prof. Dr.-Ing. Bernhard Weigand
Tag der mündlichen Prüfung:	10. Juni 2024

Institut für Technische Verbrennung
der Universität Stuttgart
2024

Dedicated to the love of my life Yulia, and the amazing Zimnitskiy family.

In loving memory of Alexey Zimnitskiy.

Abstract

A critical step for rocket engine operation in the vacuum of space is the efficient atomization, mixing and ignition of the liquid propellants. In the case of cryogenic fluids the atomization process is driven by flash boiling as the fluid exits the injectors. It is well known that the flash boiling process is caused by the nucleation of microscopic vapour bubbles in the superheated liquid that drive the jet expansion and an intense phase change process. This work investigates the primary breakup mechanisms at the micro-scale that are currently not well understood, due to limited empirical data. For this, direct numerical simulations (DNS) are performed using a multi-phase solver with interface capturing, providing a level of detail not previously achieved for this type of atomization process.

The ab-initio methodology relies on first computing exact solutions for spherical bubble growth in superheated liquid, capturing compressibility and interface cooling effects. This reference data is then used to calibrate the fluid properties and vaporization rate on larger scale DNS that focus on the pure fluid-mechanical processes. These simulations are able to fully capture the hydrodynamic interactions between a large number of bubbles, as they grow, deform and coalesce, leading to the breakup of the liquid matrix into a spray of small droplets.

The high level of resolution requires the use of high performance computing techniques with an in-house developed DNS solver. Significant effort was also invested in the development of an efficient post-processing algorithm that captures surface area of individual droplets in addition to their volume, thus avoiding limiting assumptions of droplet sphericity that are necessary in most experimental and theoretical modelling approaches.

A series of test cases with regular bubble arrays demonstrates how, by varying the thermodynamic conditions and nuclei number density, various breakup mechanisms are observed resulting in distinct droplet patterns. These are systematically correlated to a range of Weber and Ohnesorge numbers, providing a predictive model for breakup classification and droplet size estimation. These breakup patterns extend beyond common assumptions and hypotheses previously suggested in the literature. Further DNS using randomized bubble clusters confirm the initial observations and provide statistical data on the spray composition. The results obtained include droplet size distributions and time-resolved evolution of total spray surface area, across a range of Weber numbers.

A droplet size estimator is proposed, uncovering a minimum for the mean droplet size that is expected for each given level of local superheat, in spite of the nuclei number density being generally unknown. The DNS data is then used to calibrate and improve on this model, from which the expected area-weighted (Sauter) mean diameter of the spray can be inferred and interpolated for various cryogenic fluids. Similarly, a DNS-calibrated model for peak surface area generation rate is proposed. The models and data provided can be used for the development of sub-grid scale models for fluid simulations in engineering applications, namely source terms for surface area generation and liquid-vapour mass fractions or transported stochastic variables for droplet size.

The DNS-calibrated models suggest that for relatively high fluid temperatures, or locally high levels of superheat, droplets can be formed in the sub-micron range and at equally small time scales, which are beyond the range accessible by common experimental methods. At more conservative levels of superheat, the method suggests droplets in the one to ten micron range, which is compatible with empirical evidence.

This work complements experimental studies that are often limited to measurements of the global spray characteristics and lack insight into the conditions and processes in the dense regions of the spray or near the nozzle. The level of physical detail and accuracy of the DNS method is, however, still limited by computational constraints. Nonetheless, the findings of this work provide a clear path for further refinement of the technique, as well as suggestions for further investigations, both numerical and experimental.

Kurzfassung

Ein entscheidender Schritt für den Betrieb von Raketentriebwerken im Vakuum des Weltraums ist die effiziente Zerstäubung, Mischung und Zündung der flüssigen Treibstoffe. Bei kryogenen Flüssigkeiten wird der Zerstäubungsprozess durch Flashboiling an den Injektoren ausgelöst. Es ist bekannt, dass der Flashboiling-Prozess durch die Keimbildung von mikroskopisch kleinen Dampfblasen in der überhitzten Flüssigkeit verursacht wird, die die Strahlausdehnung und einen intensiven Phasenwechselprozess bewirken. Diese Arbeit beleuchtet die primären Zerfallsmechanismen auf der Mikroskala, die derzeit aufgrund begrenzter empirischer Daten nicht hinreichend verstanden sind. Zu diesem Zweck werden Direkte Numerische Simulationen (DNS) unter Verwendung eines Mehrphasen-Lösers mit Grenzflächenerfassung durchgeführt, die einen für diese Art von Zerstäubungsprozess bisher nicht erreichten Detaillierungsgrad bieten.

Die ab-initio-Methode beruht darauf, dass zunächst exakte Lösungen für das Wachstum sphärischer Blasen in überhitzter Flüssigkeit berechnet werden, die die Effekte der Kompressibilität und der Grenzflächenkühlung einbeziehen. Diese Referenzdaten werden dann zur Kalibrierung der Flüssigkeitseigenschaften und der Verdampfungsrate in DNS-Simulationen größeren Maßstabs verwendet, die sich auf die rein fluidmechanischen Prozesse konzentrieren. Diese Simulationen sind in der Lage, die hydrodynamischen Wechselwirkungen zwischen einer großen Anzahl von Blasen vollständig zu erfassen, während sie wachsen, sich verformen und koaleszieren, was zum Aufbrechen der Flüssigkeitsmatrix zu einem Sprühnebel aus kleinen Tröpfchen führt.

Der hohe Auflösungsgrad erfordert den Einsatz von Hochleistungsrechenverfahren mit einem eigenentwickelten DNS-Solver. Ein erheblicher Aufwand wurde auch in die Entwicklung eines effizienten Post-Processing-Algorithmus getätigt, der neben dem Volumen auch die Oberfläche der einzelnen Tröpfchen erfasst und damit die einschränkenden Annahmen zur Sphärizität der Tröpfchen vermeidet, die bei den meisten experimentellen und theoretischen Modellierungsansätzen notwendig sind.

Eine Reihe von Testfällen mit regelmäßigen Blasenanordnungen zeigt, wie durch Variation der thermodynamischen Bedingungen und der Keimzahldichte verschiedene Zerfallsmechanismen beobachtet werden können, die zu unterschiedlichen Tröpfchenmustern führen. Diese werden systematisch mit einer Spanne von Weber- und Ohnesorge-Werten

korreliert, wodurch ein Vorhersagemodell für die Klassifizierung des Aufbrechens und die Schätzung der Tröpfchengröße entsteht. Diese Zerfallsmuster gehen über die üblichen Annahmen und Hypothesen hinaus, die zuvor in der Literatur beschrieben wurden. Weitere DNS-Untersuchungen, bei denen zufällig angeordnete Blasencluster verwendet werden, bestätigen die anfänglichen Beobachtungen und liefern statistische Daten über die Zusammensetzung des Sprühnebels. Die Ergebnisse umfassen die Verteilung der Tröpfchengröße und die zeitliche Entwicklung der Gesamtoberfläche des Sprays über eine Spanne von Weber-Werten.

Es wird eine Abschätzung für die Tröpfchengröße vorgeschlagen, die ein Minimum für die durchschnittliche Tröpfchengröße ermittelt, die für jedes gegebene Stadium der lokalen Überhitzung zu erwarten ist, obwohl die Anzahl der Keime im Allgemeinen unbekannt ist. Die DNS-Daten werden dann zur Kalibrierung und Verbesserung dieses Modells verwendet, aus dem der erwartete flächengewichtete (Sauter) mittlere Durchmesser des Sprühnebels abgeleitet und für verschiedene kryogene Flüssigkeiten interpoliert werden kann. In ähnlicher Weise wird ein DNS-kalibriertes Modell für die Erzeugungsrate der Peakfläche vorgeschlagen. Die bereitgestellten Modelle und Daten können für die Entwicklung von Sub-Grid-Scale-Modellen für Strömungssimulationen in technischen Anwendungen verwendet werden, insbesondere für Quellterme für die Oberflächenerzeugung und Flüssigkeits-Dampf-Massenanteile oder transportierte stochastische Variablen für die Tröpfchengröße.

Die DNS-kalibrierten Modelle deuten darauf hin, dass sich bei relativ hohen Strömungstemperaturen oder lokal hohen Überhitzungsgraden Tröpfchen im Submikronbereich und auf ebenso kleinen Zeitskalen bilden können, die außerhalb des Bereichs liegen, der mit üblichen experimentellen Methoden erreichbar ist. Bei konservativeren Überhitzungswerten deutet die Methode auf Tröpfchen im Bereich von ein bis zehn Mikrometer Durchmesser hin, was mit empirischen Erkentnissen vereinbar ist.

Diese Arbeit ergänzt experimentelle Studien, die sich häufig auf Messungen der globalen Sprüheigenschaften beschränken und keinen Einblick in die Bedingungen und Prozesse in den dichten Bereichen des Sprühnebels oder in der Nähe der Düse geben. Der physikalische Detaillierungsgrad und die Genauigkeit der DNS-Methode sind jedoch nach wie vor durch Beschränkungen des Rechenaufwands begrenzt. Nichtsdestotrotz bieten die Ergebnisse dieser Arbeit einen klaren Ausgangspunkt für eine weitere Verfeinerung der Technik, sowie Vorschläge für weitere numerische als auch experimentelle Studien.

Preface

Parts of this thesis have been presented at conferences and published in the archival literature. The background and theoretical developments given in chapters 2, 3, 4 and 6 have been modified with respect to the originally published texts and been significantly extended to ensure completeness, coherence and consistency of the present manuscript. The authors contributions are listed in accordance to the CRediT[1] definitions. The relevant papers are:

Loureiro et al. [1]: D. D.Loureiro, J. Reutzsch, D. Dietzel, A. Kronenburg, B. Weigand, K. Vogiatzaki "DNS of Multiple Bubble Growth and Droplet Formation in Superheated Liquids" ICLASS 2018, 14 Triennial International Conference on Liquid Atomization and Spray Systems, Chicago, IL, USA, July 22-26, 2018.

D. D.Loureiro: Conceptualization (equal), Methodology (lead), Software (pre- and post-processing code, modifications to DNS code), Formal analysis, Investigation, Data Curation, Writing - Original Draft, Visualization.

J. Reutzsch: Software (DNS code development, deployment support), Writing - Review & Editing.

D. Dietzel: Conceptualization (equal), Software (RP-e solver), Writing - Review & Editing.

A. Kronenburg: Conceptualization (equal), Methodology, Resources, Supervision (main), Writing - Review & Editing (significant), Project administration.

B. Weigand: Resources (DNS code), Writing - Review & Editing.

K. Vogiatzaki: Conceptualization (equal), Supervision (second), Project administration, Funding acquisition, Writing - Review & Editing.

Loureiro et al. [2]: D. D.Loureiro, J. Reutzsch, A. Kronenburg, B. Weigand, K. Vogiatzaki "Resolving breakup in flash atomization conditions using DNS" ICMF 2019, 10th International Conference on Multiphase Flow, Rio de Janeiro, Brazil, May 19–24, 2019.

[1] Contributor Roles Taxonomy `https://www.elsevier.com/researcher/author/policies-and-guidelines/credit-author-statement` Accessed 17.11.2023

D. D.Loureiro: Conceptualization (equal), Methodology (lead), Software (pre- and post-processing code, modifications to DNS code), Formal analysis, Investigation, Data Curation, Writing - Original Draft, Visualization.

J. Reutzsch: Software (DNS code development, deployment support), Writing - Review & Editing.

A. Kronenburg: Conceptualization (equal), Methodology, Resources, Supervision (main), Writing - Review & Editing (significant), Project administration.

B. Weigand: Resources (DNS code), Writing - Review & Editing.

K. Vogiatzaki: Conceptualization (equal), Supervision (second), Project administration, Funding acquisition, Writing - Review & Editing.

Loureiro et al. [3]: D. D.Loureiro, J. Reutzsch, A. Kronenburg, B. Weigand, K. Vogiatzaki "Towards full resolution of spray breakup in flash atomization conditions using DNS" High Performance Computing in Science and Engineering '19, Springer International Publishing 2021 (submitted 2019).

D. D.Loureiro: Conceptualization (equal), Methodology (lead), Software (pre- and post-processing code, modifications to DNS code), Formal analysis, Investigation, Data Curation, Writing - Original Draft, Visualization.

J. Reutzsch: Software (DNS code development, deployment support), Writing - Review & Editing.

A. Kronenburg: Conceptualization (equal), Methodology, Resources, Supervision (main), Writing - Original Draft, Project administration.

B. Weigand: Resources (DNS code), Writing - Review & Editing.

K. Vogiatzaki: Conceptualization (equal), Supervision (second), Project administration, Funding acquisition, Writing - Review & Editing.

Loureiro et al. [4]: D. D.Loureiro, J. Reutzsch, A. Kronenburg, B. Weigand, K. Vogiatzaki "Primary breakup regimes for cryogenic flash atomization", International Journal of Multiphase Flow 2020.

D. D.Loureiro: Conceptualization (equal), Methodology (lead), Software (pre- and post-processing code, modifications to DNS code), Formal analysis, Investigation, Data Curation, Writing - Original Draft, Visualization.

J. Reutzsch: Software (DNS code development, deployment support), Writing - Review & Editing.

A. Kronenburg: Conceptualization (equal), Methodology, Resources, Supervision (main), Writing - Review & Editing (significant), Project administration.

B. Weigand: Resources (DNS code), Writing - Review & Editing.

K. Vogiatzaki: Conceptualization (equal), Supervision (second), Project administration, Funding acquisition, Writing - Review & Editing.

Loureiro et al. [5]: D. D.Loureiro, J. Reutzsch, A. Kronenburg, B. Weigand, K. Vogiatzaki "Droplet size distributions in cryogenic flash atomization" International Journal of Multiphase Flow 2021.

D. D.Loureiro: Conceptualization (equal), Methodology (lead), Software (pre- and post-processing code, modifications to DNS code), Formal analysis, Investigation, Data Curation, Writing - Original Draft, Visualization.

J. Reutzsch: Software (DNS code development, deployment support), Writing - Review & Editing.

A. Kronenburg: Conceptualization (equal), Methodology, Resources, Supervision (main), Writing - Review & Editing (significant), Project administration, Funding acquisition.

B. Weigand: Resources (DNS code), Writing - Review & Editing.

K. Vogiatzaki: Conceptualization (equal), Supervision (second), Project administration, Funding acquisition, Writing - Review & Editing.

Acknowledgements

This work was made possible through participation in two collaborative projects that provided funding, training and extensive networking opportunities. They are:

- HAoS-ITN – Marie Sklodowska-Curie Innovative Training Networks "Holistic Approach of Spray Injection through a Generalized Multi-phase Framework", Grant Agreement No 675676 funded by the European Union Horizon 2020 Research and Innovation programme.

- SFB-TRR 75 – Collaborative Research Center Transregio 75 "Droplet Dynamics Under Extreme Ambient Conditions", project number 84292822 funded by the Deutsche Forschungsgemeinschaft (DFG, German Research Foundation).

The CFD simulations presented in this work were performed in close collaboration with the Institute of Aerospace Thermodynamics (ITLR) and with computational resources and support provided by the High Performance Computing Center Stuttgart (HLRS).

On a personal level, I would like to first express my sincere gratitude to my supervisor Prof. Andreas Kronenburg, not only for trusting me with this project and career opportunity, but also for his immense patience and interest through many long, but always productive discussions. I also thank him for sharing his expertise and especially for his contributions to the writing process, which was not always my strong suit. Thank you also to my co-supervisor Dr. Konstantina Vogiatzaki who originally proposed and made this project possible.

My gratitude goes also to all my colleagues at ITV, for their friendship and good spirit over the years at the institute. Especial thanks to Dirk Dietzel for his initial guidance into the world of flash boiling, and to Jan Gärtner for many fruitful discussions on the topic, in addition to his exceptional IT technical support.

I am also very thankful to the colleagues at ITLR, Jonathan Reutzsch and Jonas Steigerwald, for sharing their office with me, which always led to many productive and fun discussions, in addition to their essential collaboration.

For my introduction into the world of experimental rocketry, I would like to thank Prof. M. Oschwald, Andreas Rees and colleagues at the DLR Institute of Space Propulsion, where I was hosted for my secondment through the HAoS-ITN project.

The present text was largely written during my employment at European XFEL GmbH and for this reason I would like to thank supervisor Sebastian Göde, for allowing me the necessary time flexibility, in addition to sharing his expertise in cryogenic fluid behaviour and experimental methods.

Thank you to my parents for the encouragement and unconditionally supporting me through my studies. Also to my sister Isabel for the support and illustration contribution.

Obrigado aos meus pais pelo incentivo e apoio incondicional ao longo dos meus estudos.

This thesis is dedicated to Yulia and the Zimnitskiy family for the endless love, patience, support and encouragement through the best and the toughest of times. Most of all, thank you for inspiring me to be the best I can be.

Эта диссертация посвящается Юлии и семье Зимницких за бесконечную любовь, терпение, поддержку и ободрение в самое лучшее и самое трудное время. Больше всего спасибо за то, что вы вдохновляете меня быть самым лучшим, каким я могу быть.

Table of contents

List of figures

List of tables

Nomenclature

Latin

A	Surface area (interface) $\left[\mathrm{m}^2\right]$
a	Surface area density (interface) $\left[\mathrm{m}^2/\mathrm{m}^3\right]$
c_p	Specific heat at const. pressure $\left[\mathrm{J/kg/K}\right]$
D	Droplet diameter [m]
$\overline{D}_A$	Droplet area-weighted (Sauter) mean diameter [m]
D_A^{fit}	DNS-fitted area-weighted (Sauter) mean diameter [m]
$\overline{D}_{ij}$	Droplet weighted mean diameters (assuming sphericity) [m]
$\overline{D}_N$	Droplet arithmetic mean diameter [m]
D_{ref}	Droplet diameter estimator [m]
$\overline{D}_V$	Droplet volume-weighted (De Broukere) mean diameter [m]
dx	Cell size [m]
e	Specific internal energy $\left[\mathrm{J/kg}\right]$
f	Volume of fluid field [−]
h	Specific enthalpy $\left[\mathrm{J/kg}\right]$
$h_{\mathrm{f}v}$	Latent heat of vaporization (specific) $\left[\mathrm{J/kg}\right]$
J_{CNT}	Bubble nucleation rate $\left[\#/\mathrm{m}^3/\mathrm{s}\right]$
Ja	Jakob number [−]
$\dot{m}''$	Vaporization mass flux $\left[\mathrm{kg/s/m}^2\right]$
$\dot{m}'''$	Volumetric vaporization rate $\left[\mathrm{kg/s/m}^3\right]$

m_m Molecule mass [kg]

n Bubble nuclei number density $\left[\#/\mathrm{m}^3\right]$

N_{bub} Number of bubble nuclei (DNS domain) [#]

$\hat{\mathbf{n}}_\Gamma$ Interface normal vector [−]

p Pressure [Pa]

R_p Pressure ratio [−]

R Bubble radius [m]

R_{crit} Bubble critical radius [m]

$\dot{R}$ Bubble growth rate $\left[\mathrm{m/s}\right]$

Oh_b Ohnesorge number [−]

Re_b Reynolds number [−]

R_g Specific gas const. $R_g = k_{\mathrm{B}}/m_m$ $\left[\mathrm{J\,kg^{-1}\,K^{-1}}\right]$

R^* Normalized bubble radius (growth factor) [−]

St Stefan number [−]

T Absolute temperature [K]

t Time [s]

t^* Normalized (at coalescence) simulation time [−]

$\boldsymbol{u}$ Velocity field vector $\left[\mathrm{m/s}\right]$

V Volume $\left[\mathrm{m}^3\right]$

v Specific volume $v = 1/\rho$ $\left[\mathrm{m^3/kg}\right]$

V_0 Reference liquid volume (domain) $\left[\mathrm{m}^3\right]$

We_b Weber number [−]

Greek

α Thermal diffusivity $\alpha = \lambda/\rho c_p$ $\left[\mathrm{m^2\,s}\right]$

ΔT Level of superheat [K]

η_f Bubble packing factor (void fraction) [−]

η_K Kolmogorov scale [m]

γ Surface area to liquid volume ratio $\left[\mathrm{m}^2/\mathrm{m}^3\right]$

γ^* Normalized (at coalescence) surface area to liquid volume ratio [−]

$\dot{\gamma}$ Rate of surface area generation (volumetric) $\left[\mathrm{m}^2/\mathrm{m}^3/\mathrm{s}\right]$

$\dot{\gamma}_\mathrm{max}^\mathrm{fit}$ DNS-fitted peak rate of surface area generation (volumetric) $\left[\mathrm{m}^2/\mathrm{m}^3/\mathrm{s}\right]$

λ Heat transfer coefficient $\left[\mathrm{W}/\mathrm{m}^2/\mathrm{K}\right]$

μ Dynamic viscosity coefficient [Pa s]

ρ Density $\left[\mathrm{kg}/\mathrm{m}^3\right]$

σ Surface tension coefficient $\left[\mathrm{N}/\mathrm{m}\right]$

$\sigma_{(N,A,V)}$ Droplet diameter standard deviation [m]

Physical Constants

k_B Boltzmann const.: $\left[1.380\,648\,8 \times 10^{-23}\,\mathrm{J\,mol^{-1}}\right]$

N_A Avogadro const.: $\left[6.022\,141\,29 \times 10^{23}\,\mathrm{mol^{-1}}\right]$

R_U Universal gas const.: $\left[8.314\,462\,1\,\mathrm{J\,K^{-1}\,mol^{-1}}\right]$

Subscripts

0 Initial or injection conditions

crit Critical (bubble radius)

crit Critical point (Pressure and temperature)

f Final, at instant of bubble coalescence

Γ At the interface

i At initialization

∞ Far-field conditions

ℓ Liquid phase

max Maximum, peak

sat Saturation conditions

triple Triple point (Pressure and temperature)

v Vapour phase

Vectorial Operators

[ ] Tensor

$\| \ \|$ Module

$\sim$ Smoothed field

$\boldsymbol{a}$ (bold) Vector

$\nabla\cdot$ Divergence

$\nabla\times$ Curl

$\boldsymbol{ab} \equiv \boldsymbol{ab}^{\mathsf{T}} \equiv \boldsymbol{a} \otimes \boldsymbol{b}$ Diadic product

∇ Gradient

$\mathbf{I}$ Identity matrix

$^{\mathsf{T}}$ Transposed matrix

Acronyms

AMR Adaptive mesh refinement

CFD Computational fluid dynamics

CFL Courant–Friedrichs–Lewy condition

CNT Classical nucleation theory

DNS Direct numerical simulation

ELSA Euler-Lagrange spray atomization

EOS Equation of state

HPC High performance computing

HRM Homogeneous relaxation model

LCH4 Liquid methane

LES Large eddy simulation

LH2 Liquid hydrogen

LN2 Liquid nitrogen

LOx Liquid oxygen

PDA Phase Doppler anemometry

PLIC Piecewise linear interface calculation

RANS Reynolds averaged Navier-Stokes

RCS Reaction control system

RP-e Rayleigh-Plesset and energy transport

SGS Sub grid scale

SMD Sauter mean diameter

TBL Thermal boundary layer

Chapter 1

Introduction

Flash atomization refers to the fluid-mechanical process of breaking-up a liquid jet into a spray of fine droplets, through the process of *flash boiling*[1]. In turn, flash boiling occurs when a liquid experiences a rapid drop in pressure, leading to a thermodynamic instability and a rapid phase change process that drastically enhances the atomization process.

The process of flash boiling relies on a liquid initially stored or advected at a stable temperature and pressure being mechanically forced into a low pressure environment, becoming *superheated*. This is a meta-stable state where the boiling point at the new pressure is much lower than the initial liquid temperature. In practice, it can be simply achieved by discharging the liquid trough a small orifice, like a fuel injector, into a larger chamber at sufficiently low pressure.

The flash atomization process is illustrated in Fig. 1.1 in the context of a rocket engine, where it plays a key role in the ignition process. Immediately after discharge into the low pressure atmosphere or vacuum, the cryogenic liquid propellants are in the superheated state. Microscopic vapour bubbles spontaneously nucleate in very large numbers within the liquid, kick-starting the atomization process. Importantly, these bubbles can form not only at the injector walls and other particular nucleation sites, but also homogeneously within the bulk of pure liquid. The bubbles, initially microscopic, grow very rapidly extracting heat from the surrounding liquid until a new equilibrium is reached at the lower pressure, or all the liquid is consumed into vapour. During this process the jet disintegrates as multiple vapour bubbles collide, coalesce, burst or simply shatter the jet through radial expansion, creating a fine

[1]Even though *boiling* and *evaporation* strictly refer to distinct types of vaporization processes, both terms *flash evaporation* and *flash boiling* are often used in the literature. In this work some of the terminology associated with evaporation and boiling is used interchangeably.

mist of droplets. These droplets are typically orders of magnitude smaller than the ones obtained in conventional sprays where the liquid is broken-up by aerodynamic interaction with the surrounding gas at normal ambient conditions.

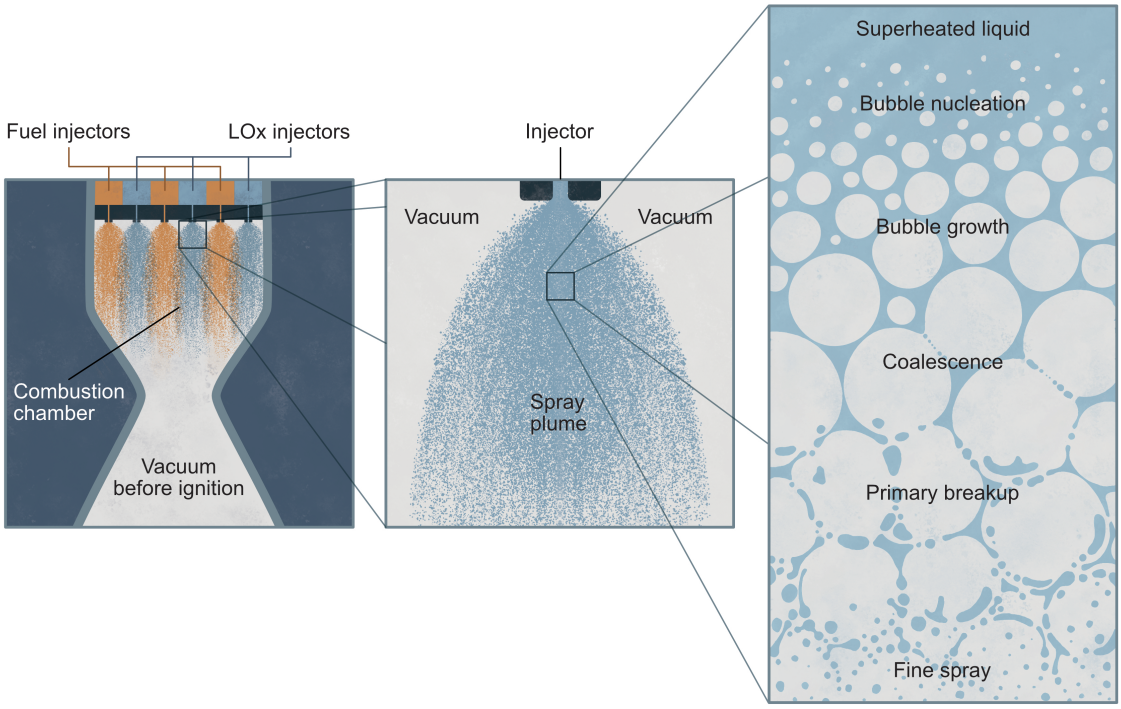

Figure 1.1: The flash boiling atomization process in the context of a rocket engine (*Illustration by Isa Loureiro).*

Flash atomization is generally beneficial in industrial and combustion applications, where it can be controlled through the design of the injector or increasing the liquid temperature. In combustion, the atomization process and mixing of fuel and air are crucial as they will affect the reliability of the ignition and the efficiency of the subsequent combustion process. This is the case of gasoline direct injection (GDI) for internal combustion engines, where improved atomization can help reduce emissions [6].

Another common application of flash boiling is the household aerosol dispenser [7], where flashing conditions are created by storing liquefied gases in a high pressure can at room temperature, that are then discharged to ambient conditions. In this case the product is mixed with the volatile propellant, such as propane, to be delivered as a fine mist.

A combination of high temperatures and high pressures is associated with accidents involving large water boilers and the storage of liquefied gases, including rocket propellants. In these cases, the lack or malfunction of a pressure release

valve, combined with an uncontrolled increase in temperature of the liquid, will lead to extremely high internal pressures and the eventual mechanical failure of the vessel. The large amount of liquid suddenly exposed to atmospheric pressure will undergo a flash boiling process, that is also known as a steam explosion. Understanding the process of droplet formation in steam explosions can be especially important in nuclear accidents as the small droplets can promote the spread of nuclear fallout [8].

Although the tools and findings presented in this work would generally apply in many of the contexts and applications just enumerated, the case of cryogenic rocket propellants will be the primary focus. Due to their low boiling point cryogenic fluids express flashing behaviour even at relatively high pressures. Flashing conditions are also generally observed for all fluids when injected into a vacuum, as is the case for spacecraft operating in the high atmosphere or Earth's orbit.

1.1 Relevance and technological impact in rocketry

Since the invention of the first liquid fueled rocket engine by Robert Goddard in 1923, cryogenic liquid oxygen (LOx) has been used as an oxidizer [9]. At the time and for subsequent rocket designs until the present day, various hydrocarbons such as kerosene and ethanol have been used as fuel. In 1961 the Centaur upper stage with the RL-10 engine by Aerojet Rocketdyne was the first to use liquid hydrogen (LH2) as fuel and is still in use today. More recently in 2019, SpaceX performed the first test flights with the Raptor engine fueled by liquid methane (LCH4). These liquid-fuel rocket variants are also referred to as kerolox, hydrolox and methalox. Due to challenges associated with storage and ignition, cryogenic propellants are, so far, only used in the large main-stage engines. This way, the cryogenic tanks can be topped-off seconds before liftoff and the priming and ignition of the engines can make use of heavy ground support equipment. Later, the final orbital insertion is performed in space by the upper-stage engine, facing additional ignition challenges. For cryogenic systems this typically occurs within minutes to a few hours from launch, limiting their flexibility e.g. for Homann-transfer maneuvers or the disposal of the rocket stage after payload deployment.

An alternative to the use of cryogenic fluids is the use of hypergolic propellants. These are reactive chemical compounds that can be kept as liquids at standard conditions and spontaneously ignite when mixed. A typical bi-propellant example is dinitrogen tetroxide (NTO) as oxidizer and hydrazine or its derivatives as fuel. Another example is highly concentrated hydrogen peroxide in combination with

a silver catalyst. These are also known as *storable* liquid propellants and were parallelly developed throughout the 20th century. Thanks to their energy density, hypergolic rocket designs do not require turbo-pumps and can be as simple as a pair of valves releasing the propellants from storage, at relatively low over-pressures, directly into the combustion chamber. The design's simplicity and ignition reliability make them ideal for reaction control systems (RCS) or vernier engines. These are small rocket thrusters used to precisely adjust the spacecraft attitude (orientation) or for ullage control. Hypergolic engines have also been chosen for long duration missions and safety-critical systems such as the descent engine for the Apollo Moon missions or emergency escape systems in modern human-carrying spacecraft. Other stored fluids include triethylaluminum and triethylborane (TEA-TEB) which is used as a high energy igniter for the main engines. However, hypergolic propellants have major disadvantages, namely their high toxicity and corrosiveness, causing safety and environmental concerns as well as ground handling costs. Various ground handling accidents [10] and other safety concerns have motivated research towards replacing these systems with safer "green" alternatives [11, 12], primarily cryogenic.

A renewed interest in human exploration missions to the moon and Mars calls for in-situ resource utilization. This implies that all propellants should be produced locally, i.e. hydrogen and oxygen via electrolysis of water ice deposits on the moon and methane via the Sabatier process on Mars. This excludes the use of hypergolics and suggests the use of Hydrolox or Methalox in all of the spacecraft systems, which can have additional advantages in terms of reducing total system complexity. Replacing hypergolic propellants with hydrolox or methalox in RCS systems as well as human-rated engines for long duration missions will require the development of new injection systems with improved ignition reliability. Here, flash boiling atomization plays a key role as it will determine the quality of the fuel-oxidizer mixing and the subsequent combustion efficiency. Some of the key factors are jet expansion and penetration, that are influenced by the rate of phase change, as well as droplet size, shape and velocity. Flashing also plays a role within the complex piping and turbomachinery of the engines, as they are primed for ignition.

A viable alternative to the use of chemicals such as TEA-TEB is the use of electric sparks or high powered lasers [13, 14, 15]. This type of system requires very precise timing and focus of the laser in a point where a combustible mixture must be present to ensure ignition. In this context deviations from the expected shape of the fuel or oxidizer plume behaviour can lead to engine failure. The precise control of the spray and ignition conditions must also consider a wide range in initial chamber

pressures that may vary from sea level to a low vacuum during a launch, the absolute vacuum of interplanetary space, a low pressure CO_2 atmosphere on the surface of Mars or a head-on hypersonic flow during atmospheric (re-)entry.

Flash boiling atomization is thus expected to play a key role in the design of future space vehicles and launch systems. A better understanding of this process can be a key factor not only in terms of safety and reliability, but also provide a competitive advantage for the commercial space industry by contributing to simpler and more efficient system designs.

1.2 Motivation and objectives

Flash boiling atomization is a multi-scale physics problem with strong interplay between the thermodynamics of phase change, the microscopic mechanics of droplet formation and the large scale morphological characteristics of the spray plume. As will be reviewed in Chapter 2, studies on flash boiling atomization have been primarily of experimental nature where the injection conditions are carefully controlled and data is retrieved in terms of spray morphology (spread, penetration, density, etc.) or by local probing of droplet size and velocity in the downstream region. While they provide actionable models via empirical correlations with the injection parameters, they contribute limited understanding on the underlying primary breakup process occurring at the exit of the nozzle.

On a deeper level, the dynamics of bubble growth in superheated liquids are well understood and can be modeled based on first-principles from classical thermodynamics and fluid mechanics. However, they provide limited insight on how this leads to the observed spray characteristics.

Computational fluid dynamics (CFD) simulations have in the past decades provided an affordable and safe alternative to experimental methods. They are developed towards engineering applications, with particular interest for conditions that are hazardous or difficult to replicate, such is the case of cryogenic and highly reactive fluids in vacuum. Here, however, the multi-scale nature of the problem presents a major road block as the complete process cannot be resolved by a single simulation method. Methods that capture the large scale features of the flow, cannot affordably resolve the liquid and vapour phases separately and other small-scale phenomena occurring below the resolution of the computational mesh. Instead, they rely on sub-grid-scale (SGS) models to determine the evolution of key variables, such as the liquid/vapour volume fraction in a cell or the statistical distribution of expected

droplet sizes. These models must be calibrated based on empirical data, or via additional direct numerical simulations (DNS).

The primary aim of this work is to use DNS methods to bridge the gap between the small scale thermo-fluid mechanics of individual bubble growth in superheated liquid and the resulting spray characteristics that can be observed experimentally. For these simulations, a state-of-the-art CFD code is deployed in high performance computer (HPC), making use of parallel programming techniques to achieve the required level of physical detail.

A better understanding of the droplet formation mechanics at the microscopic level may serve as the basis for new ab-initio models for flash atomization. Furthermore, DNS can directly provide useful data to model and calibrate SGS models in more affordable simulations of the large-scale flow for engineering applications. The combination with conventional CFD methods is of particular interest, as they can provide the local variables within the jet or spray that define the DNS boundary conditions. Fig. 1.2 illustrates the relationship and data flow between experimental methods, large-scale CFD and DNS.

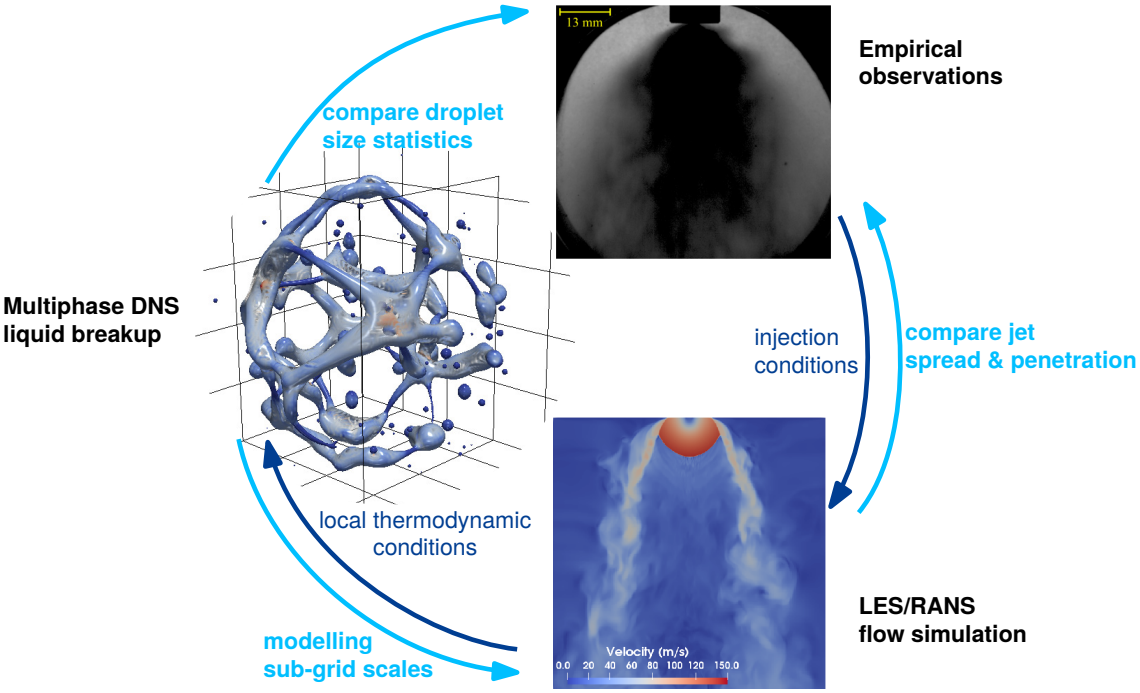

Figure 1.2: Schematic of relationships between empirical methods, large scale simulations [16] and DNS.

The specific objectives of this work as presented in this thesis are:

1. Establish an computationally affordable and systematic approach to simulate atomization in flash boiling conditions.
2. Explore and provide a qualitative characterization of the primary breakup mechanics.
3. Collect statistical data on droplet size and other spray characteristics.
4. Propose DNS-calibrated SGS models for future numerical investigations.

1.3 Thesis outline

This thesis is organized as follows: Chapter 2 provides an overview of the background literature on the topic of flash atomization and additional context for the present study. Chapter 3 introduces the relevant theory with focus on the thermodynamics of bubble growth as well as the models and reference data used in this work. Chapter 4 details the governing equations and computational methods used in the DNS solver, followed by the methodology used to define the simulation domain and key study parameters. The results are presented in Chapter 5 covering qualitative analysis of the spray patterns, resolution criteria and mesh effects, quantitative analysis of the spray formation and proposed predictive models. Chapter 6 provides a general discussion on the relevance of the results obtained, comparing with the literature. Known limitations and possible technical improvements are also discussed. A final summary and concluding remarks are provided in chapter 7, followed by suggestions for future investigations.

Chapter 2

Research background

Well known studies on flash boiling atomization can be traced back to the 1960's and 70's [17, 7]. More recent studies have remained primarily of experimental nature and only in the last decade numerical studies have become feasible. This chapter covers the background literature on experimental methods and various aspects of spray morphology and classification in Sec. 2.1. Section 2.2 covers the known theoretical models for primary breakup. Finally, Sec. 2.3 reviews the relevant literature on spray atomization using computational methods.

2.1 Experimental methods and spray morphology

It is well established [18, 19, 20, 21] that the morphology of a flashing sprays is primarily determined by the injection conditions, including the liquid temperature and the chamber pressure that determine the level of superheat (cf. Chap. 3).

Bubble nucleation can be classified as *homogeneous* when it occurs uniformly within the bulk of the liquid phase, or *heterogeneous*, when bubble nucleation is triggered at the injector walls requiring less energy per nuclei. A longer nozzle thus promotes more heterogeneous nucleation. The nozzle geometry can also be adjusted to create zones of low pressure that trigger cavitation, enhancing the atomization [21], or to avoid it in order to maximize the mass flow rate. For low superheats or small diameter jets, heterogeneous nucleation can be avoided completely, allowing for *external* atomization [22, 23, 24]. Experiments performed for a wide range of pressures [19, 22, 25] allow the observation of the transition from *partial-* to *fully-flashing* regimes. *Partially flashing* sprays pertain to low levels of superheat and are characterized by only moderate jet spreading angles and noticeable fluctuations in spray density. With increasing levels of superheat, the spreading increases and the

droplet size is reduced to a fine mist, as flashing becomes the primary driver of the atomization process.

Many experimental studies [19, 26, 23, 27] make use of shadowgraphy to correlate the macroscopic spray characteristics like spreading angle, density and penetration with the pressure ratio. Additionally, the use of Schlieren techniques allows the observation of shock waves [23]. Also relevant are the small scale characteristics of the spray like droplet size and velocity distributions. Experimentally, this can be measured using techniques such as particle image velocimetry (PIV) [28] or Phase Doppler Anemometry (PDA) [25, 27, 29, 30], however these techniques are limited to areas where the spray is sufficiently diluted and rely on the assumption of droplet sphericity for size measurements.

Theoretical criteria for transitioning to the fully flashing regime have been proposed, based on the degree of superheat. [19, 22, 25]. Notably it is observed that once the fully flashing regime is reached, the spray characteristics become insensitive to further decreases in the ambient pressure. This is comparable to an underexpanded choked flow condition where the two-phase flow can be accelerated to high Mach numbers and a system of shock formations is embedded in the spray plume [19, 23, 16].

Direct observation of liquid breakup in flashing conditions is only possible for external flashing with low levels of superheat where discrete bubbles can be observed within the jet with the use of long-distance microscopes and ultra high-speed cameras [22, 24]. For partially flashing sprays at high chamber pressures, bubble nucleation and growth is expected to only contribute to the initial jet breakup, but the viscous interaction with the relatively dense environment is responsible for the final atomization process. This type of droplet formation will be generally referred here as *aerodynamic* breakup, even though it encompasses several widely studied types of droplet formation mechanisms [31, 32].

Although more scarce due to associated experimental challenges, studies using cryogenic liquids in vacuum conditions have also been performed using the aforementioned techniques [14, 27, 28, 33]. The vacuum conditions naturally lead to the fully flashing regime in most relevant applications. It is important to note, however, that even in relatively low vacuums, it is easy to exceed the triple point of the fluid, which leads to ice formation. Under controlled pressure conditions, the general flashing behaviour follows the one of other non cryogenic liquids. Cryogenic fluids such as LOx, LN2 and LCH4, can have a higher energy threshold [33] for bubble nuclei formation, thus requiring a higher level of superheat for flashing and

delaying heterogeneous (internal) bubble nucleation, when compared to e.g. ethanol. However, the opposite is true for LH2.

Although these experimental works have provided a wide body of knowledge on the behaviour of flashing sprays, they provide little insight into the underlying mechanics of jet breakup and droplet formation. Especially for fully flashing conditions, the underlying breakup mechanism has never been directly observed based on the known literature. An alternative approach, as is the one explored in the present work, is to model the flashing process from first-principles at the microscopic scale of individual bubbles.

2.2 Primary breakup modelling

The dynamics of bubble growth in superheated liquids is a well understood phenomenon, with established models documented in the literature and validated by experiments [34, 35, 36, 18, 37]. As will be detailed in Chapter 3, the Rayleigh-Plesset equation [34] serves as the basis for the response of a bubble to pressure changes, while an equation of state and thermal boundary layer (TBL) model can be used to account for the thermodynamic effects and phase change. Once a number of bubbles collide with their neighbours and the primary breakup process effectively starts, the available models remain highly speculative. Three main breakup modes hypothesised are *inertial shattering*, *bubble coalescence* and *micro-explosion* [35].

First, *inertial shattering* suggests that large portions of liquid are radially accelerated by the internal bubble nucleation, separating large sections of the jet. This simply increases the liquid surface area enhancing the breakup that continues via the other two mechanisms or aerodynamically.

The *bubble coalescence* mode is proposed by Sher and Elata [7], Senda et al. [38] and various subsequent works. Atomization at the exit of the injector is described as the simultaneous coalescence of large numbers of bubbles densely packed in a matrix of liquid. The droplets result from the interstitial liquid between bubbles in number and size determined by the geometrical arrangement and void fraction. Thermodynamics are coupled based on energy conservation considering the surface area generated just before coalescence, or on calibrated nucleation rates that determine the bubble number density.

The *micro-explosion* mode suggests that vapour can form inside a still superheated droplet previously detached from the liquid bulk. Razzaghi [8] and others [39, 40], assume that a single bubble nucleates within the primary droplet or blob

and grows forming a liquid film that breaks at a critical thickness. As the film is being accelerated or "pushed" by the internal gas, this results in droplets with sizes determined by Rayleigh-Taylor stability theory [41]. Coupling with phase change thermodynamics is done through the internal bubble growth rate, which determines the amplitude and frequency of the interfacial instabilities.

Potential flaws of either modelling approaches, besides simplifications necessary for the application of analytical models, include the assumption of high degrees of geometrical regularity and symmetry. In addition, some degree of empirical calibration is always required, which in turn is based on measured droplet size distributions in the downstream spray, rather than at the location where breakup occurs.

2.3 Computational methods

Numerical simulations based on Navier-Stokes equations (N-S), generally referred to as computational fluid dynamics (CFD), have in the past decades provided an affordable and safe alternative to experimental methods. They are of particular interest for conditions that are hazardous or difficult to replicate, such is the case of cryogenic and highly reactive fluids in vacuum. Here, however, the multi-scale nature of the problem presents a major road block as the complete process cannot be resolved with a single CFD method. They can thus be segregated into the two main types covered in the following sections.

2.3.1 Large scale spray simulations

Reynolds-averaged Navier-Stokes (RANS) or Large Eddy Simulation (LES) [42, 43, 44, 45, 46, 16, 47] are common methods used in CFD for engineering applications. They can provide great detail to the flow patterns of the flashing spray and how it interacts with the chamber geometry, or with other spray plumes, as would occur in fuel-oxidizer mixing.

However, these models cannot resolve all scales of the liquid-vapour interactions at the phase interface and instead rely on calibrated sub-grid-scale (SGS) models, similar to the idea of sub-grid turbulence models. These are theoretical or empirically calibrated to provide closure for the liquid-vapour interface phenomena (phase change and capillary effects) that ultimately drive the flow. Consequently, CFD methods using SGS models have limited predictive capabilities. In addition, only one set of conservation equations is often solved for a surrogate fluid representing the mixture of vapour and liquid within a cell. To distinguish between the two phases,

an additional scalar for the volume or mass fraction is transported. This approach is referred to as one-fluid modelling [16, 46, 43]. For large-scale simulations, the one-fluid method does not resolve individual bubbles but relies on sub-grid models to represent phase interactions. A critical property that must be modeled for flashing flows is the phase transfer due to vaporization, which can be solved by suitable sub-grid models such as the homogeneous relaxation model (HRM).

Studies using Eulerian-Lagrangian methods (e.g. [42, 48]) transport statistical data on droplet size as discrete particles (Lagrangian stochastic particles) within a continuous (Eulerian) flow. The Eulerian–Lagrangian Spray Atomization (ELSA) approach [49, 44, 45, 47] expands the capabilities of the Euler-Euler modelling by attempting to model the sub-grid droplet size through the use of independent variables representing volume fraction and surface area density of the sub-grid two phase flow.

2.3.2 Liquid breakup DNS

A lack of empirical data to calibrate SGS models, particularly for small scale phenomena and hard to probe regions of the flow, again calls for a computational alternative. This is provided by Direct Numerical Simulations (DNS) that is, finally, the approach explored in this work. The term DNS is typically refers to the fact that no sub-grid-scale models are used and only the fundamental laws of fluid mechanics are employed, with sufficient resolution to capture all the relevant physics.

In the more wide-spread context of turbulent flows, DNS is used as opposed to LES and RANS meaning that all scales associated with turbulence and energy dissipation through the formation of eddies (Kolmogorov scales) are fully resolved in space and time. With two-phase DNS, also referred to as interface-capturing DNS, the liquid-vapour interfaces are *also* fully resolved in the space and time domains, considering the effect of phase change and liquid surface tension in addition to viscous effects.

Although various interface capturing DNS methods have been available in the past two decades [50], only recently they have become affordable for application in atomization problems thanks to advances in high performance computing (HPC). Due to the high resolutions required, DNS simulations are also still very limited in terms of physical domain size and are typically only used for representative or archetype test cases.

Early DNS of liquid jet breakup and droplet formation include Desjardins et al. [51], Lebas et al. [49] and Shinjo and Umemura [52], where the formation of the

small scale liquid structures and their breakup into small droplets is analysed. More recently Ertl et al. [53] extended the method to breakup of non-Newtonian jets using the same numerical tools employed in this work.

All these works have focused on aerodynamic atomization, i.e., the breakup resulting from liquid-vapour interaction and turbulent flow. Thus, the Kolmogorov scale is used as the primary resolution criterion, implying that the flow is fully resolved once the cell size is of the order of the smallest-scale turbulent structures. This is, however, not necessarily below the size of the smallest liquid structures dictated by surface tension effects, that act with increasing strength towards the smallest scales.

Similarly to the Kolmogorov scales used to estimate the size of the smallest eddies in turbulent flows, the *Hinze scale* [31] may be used as a reference to estimate the smallest droplets that would resist breakup through aerodynamic interaction with the surrounding gas. However, this is only one of many possible mechanisms for primary breakup and droplet formation, as will be shown in the present work.

It can thus be questioned if a "true DNS" is achieved in the context of multi-phase flows. A benchmark study by Estivalezes et al. [54] shows mesh dependency of the results at all levels of resolution for several DNS codes, that have been attributed to enstrophy generation at the liquid-vapour interfaces. Furthermore, as pointed out by Gorokhovski and Herrmann [50], every DNS of liquid breakup implies topological changes that cannot be resolved by DNS within the continuum assumption of the Navier-Stokes equations. Due to numerical discretization, topological changes are necessarily and automatically introduced when the distance between two interfaces can no longer be resolved. This suggests that the smallest liquid structure formed during breakup in N-S based DNS is always of the order of the cell size, even if adaptive mesh refinement (AMR) is employed [55] or if the cell size approaches the molecular scale (present work).

The inclusion of thermodynamic effects in multiphase DNS is of special relevance for the study of flash boiling phenomena. This implies the resolution of heat transfer at the level of individual bubbles and droplets and additional computational effort. Developments in the treatment of phase change in multi-phase DNS include the work presented in [56, 57, 58] and most recently in Reutzsch et al. [59]. These are however limited to the study of individual droplets or bubbles where the vaporization is regulated by relatively slow heat diffusion processes. Flash boiling, however, implies much higher levels of heat and mass transfer leading sharp temperature gradients that cannot yet be affordably resolved, particularly in the context of atomization

studies with large numbers of bubbles and droplets.

A notable advancement towards DNS simulation of flash boiling was achieved by Dietzel et al. [60] who simulated the growth of multiple bubbles in superheated liquid in a fully compressible two-phase framework. Thus, thermodynamic effects are included via equations of state that regulate the vaporization rate. Bubble to bubble interaction is captured via propagation of pressure waves. With their implementation, however, it was not feasible to capture the complexity of the subsequent liquid breakup, that is ultimately the focus of the present work.

This overview provides only a sample of a large body of work done towards CFD simulations of multi-phase flows in HPC. Studies of primary liquid breakup involving multiple bubbles in flashing conditions have not been found in the known literature.

Chapter 3

Bubble nucleation and growth

This chapter covers the thermodynamics and theoretical models of phase change for liquids in superheated conditions. In the first section the basic concepts for the equation of state and latent heat are introduced. Section 3.2 focuses on the process of liquid superheating and bubble nucleation and provides numerical values for key metrics and properties of interest of LOx for the conditions that will be later used in this work. Then, in Sec. 3.3, models for spherical bubble growth from the background literature are briefly summarized. It is followed in Sec. 3.4 by the final reference model used in this work again applied to LOx bubbles, providing the base data and parameters necessary for the DNS setup and the characterization of the resulting atomization process.

3.1 Fundamentals of phase change

For the description of phase change processes, an essential tool is the ability to characterise the material properties and the energy stored in a fluid based on known or measurable intensive properties like the absolute temperature, T, pressure, p, and density, ρ. These are known as state variables and are related through an equation of state (EOS), such as the ideal gas law, which is a commonly used approximation for gases and can be written as

$$pv = R_g T \tag{3.1}$$

where $v = 1/\rho$ is the specific volume and $R_g = k_\mathrm{B}/m_m$ is the specific gas constant, given the molecule mass of the substance. The ideal gas law neglects inter-molecular forces and the volume of individual molecules. An improved alternative is the van der Waals EOS [61] that can be used to describe the behaviour of real gases and

liquids and is given by

$$p = \frac{R_g T}{v - b} - \frac{a}{v^2}, \tag{3.2}$$

where the term b accounts for the volume of the molecules and the term a/v^2 represents the inter-molecular forces that become dominant in liquids. This EOS will be used in this and the following section for illustrative purposes. More accurate empirically calibrated Helmholtz functions can be provided by the EOS library `CoolProp` [62], which has been used in this work for obtaining precise numerical values of the fluid density and internal energy, as well as other properties such as viscosity and surface tension coefficients.

The van der Waals equation describes a continuous solution of the pressure as a function of the specific volume v (or density) and temperature. In reality, not all values of v correspond to valid states of matter. Instead, the cubic equation should be solved to obtain v as a function of p and T, with one or two solutions corresponding to a stable state, that can be gas or liquid. For a conventional phase change process through slow isobaric heating, e.g. boiling water at constant atmospheric pressure, the equation simply describes a (initially small) variation of the liquid volume as a function of T. However, it is observed that when the saturation temperature, $T_{\text{sat}}(p)$, is reached, the temperature remains constant while parts of the liquid transition directly to a vapour state through a step in density, as the additional heat supplied is used to completely break the inter-molecular bonds. The energy supplied is known as the latent heat of vaporization, which represents the change in specific enthalpy, h, between the liquid and vapour states and is equivalent to the change in internal energy, plus the work done on the surroundings by the volume expansion

$$h_{\text{f}v} \equiv \Delta h \equiv h_v - h_\ell = \Delta e + p\Delta v. \tag{3.3}$$

Here, Δ represents the change between the liquid and vapour states, for the specific internal energy, e, and volume, v, that are state functions evaluated at the environment pressure p (constant) and the corresponding saturation temperature $T = T_{\text{sat}}(p)$.

The saturation conditions $T_{\text{sat}}(p)$ or $p_{\text{sat}}(T)$ correspond to a continuous series of states where both the liquid and vapour solutions of the van der Waals equation are valid and the two states can coexist as stable phases. Eq. (3.2) does not explicitly provide the location of the saturation limits. Instead, they can be obtained via Maxwell's construction or the Clausius-Clapeyron equation which ensure that both phases have equal Gibbs free energy and are thus in thermodynamic equilibrium

[61]. Here, for the sake of simplicity, it is assumed that $p_{\mathrm{sat}}(T)$ or $T_{\mathrm{sat}}(p)$, as well as Δe are known via an accurate EOS.

3.2 Superheat and bubble nucleation

Contrary to isobaric boiling, in flash boiling conditions phase transition is achieved through adiabatic expansion with no external supply of heat. The process is described in the pressure-volume diagram of Figure 3.1. The isotherm (in red) represents the behaviour described by the van der Waals EOS (Eq. (3.2)) which predicts a continuous transition from liquid to gas inside the dome described by the saturation lines. The fluid cannot exist, however, in the dashed segment where $\partial p/\partial v > 0$ implies a mechanical non-equilibrium condition.

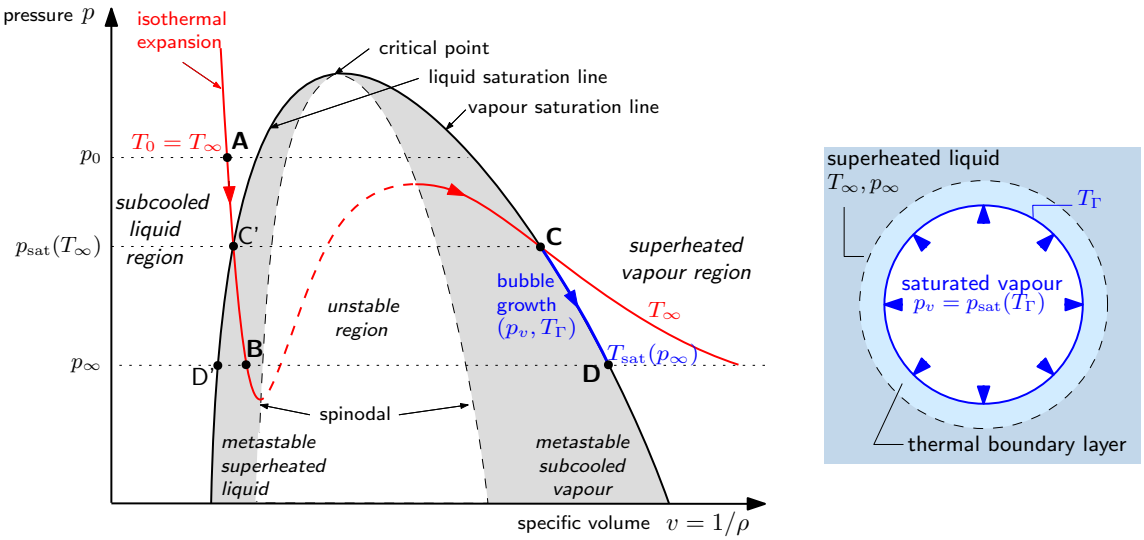

Figure 3.1: Pressure-volume diagram (left) and schematic of a bubble submerged bubble (right). The flashing phase change process is defined along the isotherm described by the van der Waals equation (illustrative behaviour), showing liquid superheating (A-B), isothermal nucleation (B-C) and bubble growth (C-D). The conditions in and around the bubble during the C-D stage are schematized on the right.

The liquid initially stored at sub-cooled conditions (point A) at pressure p_0 and temperature T_0, is rapidly discharged into a low pressure environment at p_∞ (point B). The injection process is assumed to be isothermal such that the liquid remains at temperature $T_\infty = T_0$. Here, and throughout this work, T_∞ and p_∞ will be used as the principal variables characterizing the thermodynamic conditions, where the subscript ∞ denotes far-field conditions, i.e., the environment pressure and the

liquid temperature far away from the liquid-vapour interface where the phase change process is taking place.

Point B, at pressure p_∞ is below the saturation condition $p_{\text{sat}}(T_\infty)$ meaning that the liquid is now superheated. This state can be characterized in terms of degrees superheat,

$$\Delta T = T_\infty - T_{\text{sat}}(p_\infty), \tag{3.4}$$

or pressure ratio,

$$R_p = \frac{p_{\text{sat}}(T_\infty)}{p_\infty}. \tag{3.5}$$

Superheated liquid is a meta-stable state where the condition for mechanical equilibrium $dp/dv < 0$ is still verified. The minimum pressure achievable is represented by the *spinodal line*, where $\partial p/\partial v = 0$. Although mechanically stable, point B is only a local minimum in terms of thermodynamic potential (note that C' and C at the saturation lines have equal Gibbs free energy and further expansion work pv has been done between point C' and B). The liquid can thus remain in state B only temporarily, until local fluctuations in density (i.e. the natural variance in the number of molecules in a given region of the volume) or a further decrease in the local pressure trigger the phase change process, forming a vapour bubble within the liquid at point C, where the vapour pressure is $p_v = p_{\text{sat}}(T_\infty)$.

Bubble nucleation at point C is only an approximation, since it neglects the additional supply of latent heat to form the bubble that would require cooling of the surrounding liquid (and thus thermal non-equilibrium) or nuclei formation at a lower pressure. More precisely, it can be shown (Carey [61] p.138) by integration of the Gibbs-Duhem equation that

$$p_v = p_{\text{sat}}(T_\infty) \exp\left(\frac{p_\infty - p_{\text{sat}}(T_\infty)}{\rho_\ell R_g T_\infty}\right) \tag{3.6}$$

is the vapour pressure that ensures thermodynamic equilibrium with $T_v = T_\infty$ while considering the expansion work. However, the effect of the exponential term is negligible for high liquid/vapour density ratios, justifying the $p_v = p_{\text{sat}}(T_\infty)$ approximation. An extreme case considered in this work is LOx at $T_\infty = 120\,\text{K}$, for which ρ_ℓ/ρ_v is only ≈ 24, but still the approximation error for p_v is less than 3.5%.

The derivation of Eq. (3.6) also takes into account the effect of the Laplace pressure, that allows mechanical equilibrium considering $p_v >> p_\infty$. The Young-Laplace equation describes the capillary pressure across the liquid vapour-interface

due to surface tension in a spherical bubble as

$$\Delta p = p_v - p_\infty = \frac{2\sigma}{R}, \tag{3.7}$$

where σ is the surface tension coefficient evaluated at the liquid temperature T_∞. With $p_v = p_{\text{sat}}(T_\infty)$, Eq. (3.7) is used to define the critical bubble radius, R_{crit}, as the smallest bubble size for which the vapour pressure is in mechanical equilibrium with the environment and the capillary forces,

$$R_{\text{crit}} = \frac{2\sigma}{p_{\text{sat}}(T_\infty) - p_\infty}. \tag{3.8}$$

This mechanical equilibrium is unstable, meaning that bubbles smaller than R_{crit} would collapse under the surface tension force, while larger ones will experience rapid growth driven by the internal vapour pressure.

Once the bubble starts to grow, even though the system is no longer in equilibrium, a local quasi-steady process can be assumed inside the bubble, implying that the vapour will remain in saturation conditions as new vapour is continuously being generated at the interface and the volume increases. However, since latent heat must be supplied for the phase change process, the interface temperature, T_Γ, will gradually decrease towards point D, as described in Fig. 3.1 by the blue line. As the liquid cools at the interface, the far-field temperature in the bulk of the liquid T_∞ remains constant, leading to the formation of a thermal boundary layer around the bubble. This is depicted in Fig. 3.1 (right). The dynamics of bubble growth are thus determined not only by the pressure difference across the interface, but also by heat conduction, as will be detailed in Sec. 3.3. At point D, $T_\Gamma = T_{\text{sat}}(p_\infty)$ meaning that the interface has cooled to a point where the vapour pressure equals the environment, i.e. $p_v = p_{\text{sat}}(T_\Gamma) = p_\infty$. Still, the temperature gradient in the liquid continues to conduct heat to the interface driving further growth. The final thermodynamic equilibrium is only reached once the surrounding liquid has also cooled to $T_{\text{sat}}(p_\infty)$ (point D') or completely vaporized.

It should be noted that for $p_\infty < p_{\text{triple}}$ (high vacuum) the saturation temperature would correspond to the solid phase. This implies that the interface (and then the surrounding liquid) would freeze and slowly sublimate until thermal equilibrium is reached in the bulk solid phase. Such effect should be considered in practical applications, however, it is not included for the range of pressures covered in this work.

This process of adiabatic expansion is often globally characterized by the Jakob

number which quantifies the ratio between the available heat stored in the liquid and the latent heat required for complete vaporization. It is defined [37] as

$$\mathrm{Ja} = \frac{\rho_\ell c_{p,\ell} \left| T_\infty - T_{\mathrm{sat}}(p_\infty) \right|}{\rho_v h_{\mathrm{f}v}}, \tag{3.9}$$

where $c_{p,\ell}$ and ρ_ℓ are evaluated at T_∞ assuming incompressible liquid, and ρ_v and $h_{\mathrm{f}v}$ are evaluated at $T_{\mathrm{sat}}(p_\infty)$ (point D).

The Stefan number is similarly defined in mass-specific form,

$$\mathrm{St} = \mathrm{Ja}\frac{\rho_v}{\rho_\ell} = \frac{c_{p,\ell} \left| T_\infty - T_{\mathrm{sat}}(p_\infty) \right|}{h_{\mathrm{f}v}}, \tag{3.10}$$

with $\mathrm{St} = 1$ representing nucleation at the spinodal line, while practical homogeneous nucleation occurs between $\mathrm{St} = 0.5$ and 0.8 [21].

Classical nucleation theory (CNT) can also be used to calculate a bubble nucleation rate,

$$J_{\mathrm{CNT}} \propto \exp(-\Delta G / k_{\mathrm{B}} T), \tag{3.11}$$

where J_{CNT} denotes the number of bubbles nucleated per unit of liquid volume and time. It is based on the Gibbs energy necessary to form a nucleus and the thermodynamic potential associated with the liquid temperature. Although the model provides a good approximation for the temperature dependence, the proportionality constant is difficult to determine. Consequently the model can be used as a threshold to determine whether or not flashing occurs at a given injection condition [19], but is not adequate to predict absolute nuclei number densities or local void fraction within the flow.

With LOx as the working fluid, R_{crit} and the various superheat metrics described are provided in Table 3.1 as numerical values for the various thermodynamic conditions and DNS test cases studied in this work. Also included are the reference saturation conditions and the various necessary fluid properties, obtained using the `CoolProp` [62] EOS library.

The Jacob number and R_p are most often used in conjunction with the jet Weber number to characterize the morphological behaviour of flashing sprays. However, an inspection of Tab. 3.1 shows that ΔT and R_p are inconsistent in quantifying the level of superheat: condition 3 (at low temperature and low pressure) has a higher R_p than condition 4 (at higher temperature and high pressure), while ΔT shows that condition 4 has a higher degree of superheat. A similar inconsistency is found when comparing Ja and St numbers. Furthermore, Ja varies by two orders

Table 3.1: Superheat metrics, critical radius and fluid properties for LOx. Cases A to D provide correspondence to the series of DNS cases presented in the following chapters and consistent with Loureiro et al. [5].

Condition	1	2	3	4	5
T_∞ [K]	120	100	80	120	100
p_∞ [Pa]	10^3	10^3	10^3	10^5	10^5
DNS case	Cases A	Cases B	Cases C	—	Cases D
ΔT [K]	58.7	38.7	18.7	29.9	9.94
R_p [−]	1022	254	30.12	10.22	2.54
Ja [−]	7404	4921	2511	59.86	20.03
St [−]	0.478	0.284	0.133	0.271	0.081
J_{CNT} $[\#/\mathrm{m^3 s}]$	10^{40}	10^{40}	10^{36}	10^{39}	10^{31}
R_{crit} [µm]	0.012	0.0849	1.08	0.0133	0.139
p_{sat} [Pa]	1.02×10^6	2.54×10^5	3.01×10^4	1.02×10^6	2.54×10^5
T_{sat} [K]	61.3	61.3	61.3	90.1	90.1
$\sigma(T_\infty)$ $[\mathrm{N/m}]$	0.006 14	0.0107	0.0157	0.006 14	0.0107
ρ_ℓ $[\mathrm{kg/m^3}]$	974	1.09×10^3	1.19×10^3	974	1.09×10^3
$c_{p,\ell}$ $[\mathrm{J/kgK}]$	1.93×10^3	1.74×10^3	1.68×10^3	1.93×10^3	1.74×10^3
μ_ℓ [Pas]	9.74×10^{-5}	1.53×10^{-4}	2.61×10^{-4}	9.74×10^{-5}	1.53×10^{-4}
$h_{\mathrm{fv}}(T_{\mathrm{sat}})$ $[\mathrm{J/kg}]$	2.37×10^5	2.37×10^5	2.37×10^5	2.13×10^5	2.13×10^5
$\rho_v(T_{\mathrm{sat}})$ $[\mathrm{kg/m^3}]$	0.0629	0.0629	0.0629	4.41	4.41

of magnitude between the cases at high and low pressure, which can be attributed to the change in vapour density, without it being necessarily associated to a drastic change in flashing behaviour. St seems to be a more suitable superheat metric as it represents an energy balance for equal masses of liquid and vapour and is in relative agreement with ΔT. Finally, it can be observed that the order of magnitude for R_{crit} is primarily determined by the liquid temperature, since $p_{\mathrm{sat}} << p_\infty$ for most cases except condition 5 with the lowest ΔT. Condition 4 is ultimately not considered for DNS since the expected breakup dynamics are similar to condition 1 (cf. Sec. 5.1).

In this work, the flash atomization process is studied from the perspective of the dynamics of bubble growth and how it leads to liquid breakup, rather than global energy potential. As shown, neither of the commonly used metrics are sufficient on their own to unequivocally define the superheated state. Therefore, *level of superheat* will be used as a generic term to compare different test cases while characterization in terms of precise superheat metrics is avoided. Instead, the use of absolute temperature and pressure values (T_∞ and p_∞) is preferred. Additionally, for each case, R_{crit} acts as a reference length scale. In the next section, the bubble the dynamics of bubble growth are analysed in greater detail.

3.3 Models for spherical bubble growth

The dynamics of vapour bubble growth and collapse have been first studied by Rayleigh [63]. Since then, various improved and extended models have been proposed and validated experimentally, as reviewed in various works [36, 64, 18, 37].

The equation of motion known as the Rayleigh-Plesset equation [34] can be written as

$$R\ddot{R} + \frac{3}{2}\dot{R}^2 = \frac{1}{\rho_\ell}\left(p_v - p_\infty - \frac{2\sigma}{R} - \frac{4\mu_\ell}{R}\dot{R}\right), \tag{3.12}$$

which models the acceleration of liquid with density ρ_ℓ, by the internal bubble pressure p_v that acts against the environment pressure, surface tension force and liquid viscosity, as given by the terms inside the brackets.

Starting at the critical radius given by Eq. (3.8), the bubble experiences several stages of growth. In the first stage, the growth is slow and restricted by surface tension. However, the inverse dependence on the radius causes an exponential acceleration. This *surface tension controlled stage* is often interpreted as an initial delay of the bubble growth that is very sensitive to the initial conditions [36].

In the second stage the growth rate, $\dot{R}$, is primarily limited by the inertia of the surrounding liquid. Assuming a constant internal vapour pressure, neglecting viscosity and in the absence of surface tension, the growth rate can be estimated as

$$\dot{R} = \sqrt{\frac{2\left(p_v - p_\infty\right)}{3\rho_\ell}}. \tag{3.13}$$

This is known as *inertia controlled growth stage*. However, the vapour pressure is determined by the interface temperature $p_v = p_{\mathrm{sat}}(T_\Gamma)$, which must decrease due to the effect of latent heat. An *inertial-thermal transition stage* will occur as both inertial and thermal effects play a role in the bubble growth and the liquid decelerates, with the formation of a thin thermal boundary layer (TBL) around the bubble.

The final stage is known as *thermal diffusion controlled growth stage*, where $p_v = p_{\mathrm{sat}}(T_\Gamma) \approx p_\infty$ and the growth rate is determined by the heat diffusion from the bulk of the liquid to the interface that supplies the latent heat for further vaporization. It can be modeled as [34]

$$\dot{R} = \mathrm{Ja}\sqrt{\frac{3\alpha_\ell}{\pi t}} \tag{3.14}$$

where $\alpha_\ell = \lambda_\ell/\rho_\ell c_{p,\ell}$ is the liquid thermal diffusivity and Ja is given by Eq. (3.9).

A flexible model proposed by Mikic et al. [65] provides a closed-form expression that interpolates between the inertial and thermal diffusion stages of growth. This was later improved by Miyatake et al. [66] to include the initial effect of surface tension and non-linear effects in the temperature dependent vapour pressure. The reference solution used in this work, however, is based on an exact computational solution using the method of Lee and Merte [36], that avoids particular assumptions related to each stage of growth, permits the use of an accurate equation of state for temperature dependent fluid properties and is relatively inexpensive in the context of modern computational resources. The approach is detailed in the following section.

It should be noted that the models described in this chapter generally make the assumption of thermodynamic equilibrium at the interface. I.e., the vapour remains at saturation condition $p_v = p_{\mathrm{sat}}(T_\Gamma)$ and in thermal equilibrium $T_v = T_\Gamma$. Furthermore it is assumed that the vapour pressure and material properties are uniform inside the bubble, even though they may vary in time according to T_v and p_v. Likewise, the liquid is assumed incompressible, even though its exact density can be computed via EOS as a function of both T_∞ and p_∞. With these assumptions, it is also implied that the temperature is uniform along the spherical interface and gradients of density or temperature within the vapour should thus be quickly dissipated, relative to the time scale of the growth. The assumptions of uniform vapour properties and liquid incompressibility are justified by low Mach numbers in both phases when considering the relatively slow growth rates (less than 20 m/s for LOx, 40 m/s for LCH4 or 60 m/s for water).

The assumption of local thermodynamic equilibrium at the interface is questioned by some authors [67, 37]. The use of the Hertz-Knudsen relation [68] is suggested [67, 69] to account for unequal vaporization and condensation fluxes as well as temperature or pressure jumps across the interface. However, the lack of reliable accommodation coefficients limits the applicability of this approach, aside from limited evidence of its relevance or validity [37, 68] for the particular case of bubble growth in superheated liquids.

3.4 Reference solution (RP-e)

The reference solution for spherical bubble growth used in this work is an implementation by Dietzel [70] following the method of Lee and Merte [36]. It integrates the Rayleigh-Plesset equation (3.12) in time, while coupled with the energy transport equation for the thermal boundary layer that develops around the bubble. For

brevity it is referred to as RP-e (Rayleigh-Plesset & energy).

The energy transport equation, given in terms of temperature $T(r,t)$, time t and spherical coordinate r as

$$\frac{\partial T}{\partial t} + \dot{R}\frac{R^2}{r^2}\frac{\partial T}{\partial r} = \alpha_\ell \left(\frac{\partial^2 T}{\partial r^2} + \frac{2}{r}\frac{\partial T}{\partial r} \right), \tag{3.15}$$

is solved by an implicit finite difference scheme on a 1D grid with irregular spacing to resolve the large gradients close to the bubble interface. The boundary conditions are $T(\infty,t) = T_\infty$ and

$$4\pi R^2 \lambda_\ell \left(\frac{\partial T}{\partial r} \right)_{r=R} = h_{\mathrm{f}v} \frac{d}{dt} \left(\frac{4}{3}\pi R^3 \rho_v \right), \tag{3.16}$$

which ensures that the heat flux matches the latent heat of vaporization. The interface temperature $T_\Gamma = T(R,t)$ provides the coupling with the Rayleigh-Plesset equation (Eq. (3.12)), through the saturation condition $p_v = p_{\mathrm{sat}}(T_\Gamma)$ and temperature dependent surface tension $\sigma(T_\Gamma)$. On the vapour side the temperature is assumed uniform and equal to T_Γ. The saturation pressure $p_{\mathrm{sat}}(T_\Gamma)$ and all other properties dependent on T_Γ (σ, ρ_v and $h_{\mathrm{f}v}$) are evaluated in real-time using the `CoolProp` EOS [62]. The Rayleigh-Plesset equation is numerically integrated in time, starting from the equilibrium at $R = R_{\mathrm{crit}}$ and with $T(r,0) = T_\infty$. In turn, it provides R and $\dot{R}$ in Eqs. (3.15) and (3.16) for each time-step.

With the TBL continuously developing from $R = R_{\mathrm{crit}}$, the method is able to capture the continuous transition between the equilibrium state at the critical radius, the inertia controlled stage and the thermal diffusion controlled stage as the bubble radius increases across several orders of magnitude.

Solutions for LOx at a range of T_∞ and p_∞ conditions (see Table 3.1) are plotted in Fig. 3.2, including the bubble radius as function of time and several variables of interest as function of bubble radius. The bubble size, shown in Fig. 3.2(a) as a function of time provides an insight into the time and length scales involved that is often not evident in the normalized figures provided in the literature. Even though each 20 K change in T_∞ implies an order of magnitude change in the initial radius, R_{crit}, all cases seem to reach sizes of the order of 0.1 mm in less than 0.1 ms. This however approaches the length and time scales associated with typical experimental injectors. Considering the high nuclei number densities allowed by CNT for high superheats, it can be expected that atomization will occur in the early stages of bubble growth soon after nucleation.

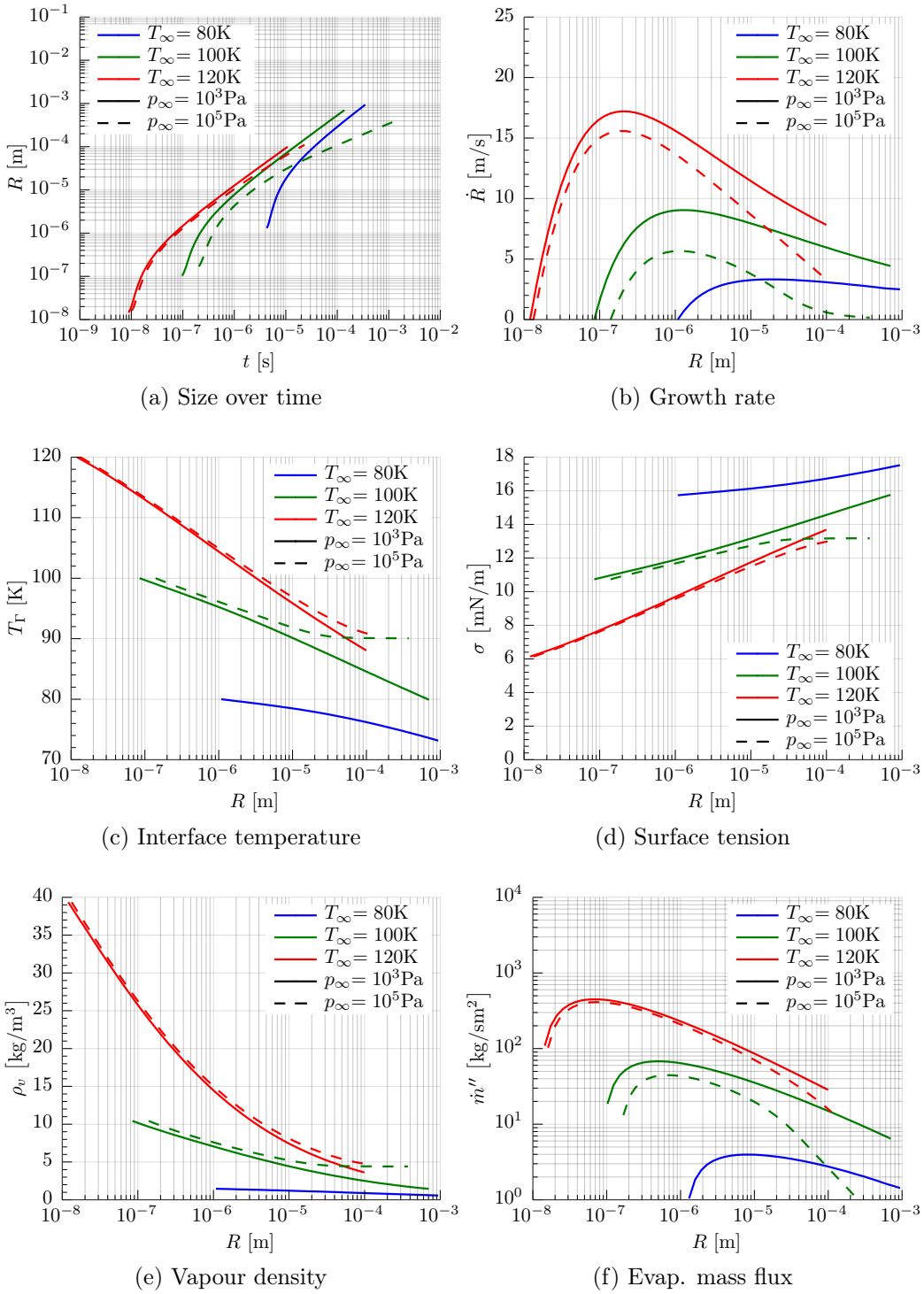

(a) Size over time

(b) Growth rate

(c) Interface temperature

(d) Surface tension

(e) Vapour density

(f) Evap. mass flux

Figure 3.2: Results of the RP-e model for spherical bubble growth for LOx at T_∞ (indicated by line colour) and p_∞ (by line type)

The different stages of growth can be observed in Fig. 3.2(b): starting at the critical radius, the inertial stage corresponds to the initial steep acceleration. Then,

due to cooling of the interface, the growth starts to decelerate. Notably, the peak is consistently observed after the bubble has grown by approximately one order of magnitude, independently of the level of superheat. It corresponds to the start of the transition stage, where both inertia and heat transfer play an important role as the growth decelerates. This stage is quite extended, covering several orders of magnitude until bubbles reach macroscopic sizes, rather than being a brief transition period as the theoretical (asymptotic) models of Sec. 3.3 might imply. The final thermal diffusion stage, where $T_\Gamma = T_{\text{sat}}(p_\infty)$, is not reached for most cases within the computed range. The exception is the case with the lowest superheat ($T_\infty = 100\,\text{K}$ at $p_\infty = 10^5\,\text{Pa}$, dashed green line) where an inflection point of $\dot{R}$ can be observed.

Nonetheless, the effect of interface cooling is significant throughout all stages of growth, as shown in Fig. 3.2(c). This figure also distinctly shows the point where the thermal diffusion stage starts for the low superheat case. Variations of T_Γ also imply considerable variations of surface tension coefficient (Fig. 3.2(d)) and vapour density (Fig. 3.2(e)) for all cases. This highlights the importance of an adequate representation of these quantities as a function of bubble size. Furthermore, near-equilibrium conditions (i.e., $p_v = p_{\text{sat}}(T_\infty)$ or $T_\Gamma = T_{\text{sat}}(p_\infty)$) do certainly not hold even if equilibrium is often used as a standard in the literature [71].

The vaporization mass flux, given by

$$\dot{m}'' = \dot{R}\rho_v, \tag{3.17}$$

will play an important role in the DNS simulations and is shown in Fig. 3.2(f). Notably, p_∞ has a negligible effect on $\dot{m}''$ for the high temperature $T_\infty = 120\,\text{K}$ cases. Also notable is the fact that the lowest peak vaporization rate corresponds to the case of lowest temperature, not the lowest superheat. These observations hold up to radii of $\approx 0.1\,\text{mm}$ and only after that (when thermal diffusion dominates) the actual level of superheat seems to become relevant. Even though the current results are based on LOx as fluid, similar results have been obtained for various cryogenic fluids, including LN2, LCH4 and LH2 (cf. Appendix E).

The RP-e model covers the complete growth of individual bubbles in flashing conditions, but does not take into consideration any interactions between the bubbles, in particular how they deform, merge and burst to form the spray. This can only be captured in full 3D simulations that resolve the hydrodynamics of multiple interacting bubbles. As detailed in the next chapter, the RP-e model is used for calibration of the fluid properties and vaporization rates in the DNS, as well as providing the basis for flow characterisation and proposed predictive models.

Chapter 4

DNS methods

For the DNS of the atomization process the in-house code `FS3D` (Free Surface 3D) for multi-phase flows [72] is used. The code employs a finite volume method to discretize the incompressible Navier-Stokes equations while capturing a fully resolved liquid-vapour interface with phase change and surface tension using the Volume of Fluid (VOF) method with PLIC (piecewise linear interface calculation) reconstruction. The governing equations are detailed in Sec. 4.1, followed by the models and schemes related to the treatment of the interface. Also in this chapter, Sec. 4.2 describes how the simulation domain is defined in the context of the global flow and identifies the primary variables and setup parameters.

Additional technical aspects related with the DNS simulations can be found in the appendices. The adaptations required in the implementation on the boundary conditions are covered in Appendix A. Further remarks on the code's performance in the HPC system and computational cost projections are provided in Appendix B. Finally, the methodology to process the DNS data and produce the results later presented is covered in Appendix. C.

4.1 Governing equations

The two-phase flow is governed by the Navier-Stokes equations in a one-fluid formulation, where the liquid and vapour are represented by a variable density, ρ, while assuming incompressible and Newtonian fluid in each phase. For a continuous three-component velocity, $\boldsymbol{u}$, and pressure field, p, the continuity (or mass conservation) and momentum conservation equations are

$$\frac{\partial \rho}{\partial t} + \nabla \cdot \boldsymbol{u} = 0 \tag{4.1}$$

and

$$\frac{\partial}{\partial t}(\rho \boldsymbol{u}) + \nabla \cdot [\rho \boldsymbol{u}\boldsymbol{u}] = \nabla \cdot \mu \left[\nabla \boldsymbol{u} + (\nabla \boldsymbol{u})^{\mathsf{T}}\right] - \nabla p + \boldsymbol{f}_\sigma, \tag{4.2}$$

respectively, where $\boldsymbol{f}_\sigma$ denotes the volumetric force due to surface tension which acts only in the vicinity of the liquid-vapour interface (Sec. 4.1.3). Other body forces and buoyancy effects are excluded in this work.

The system of equations is discretized using the finite volume method in a uniform Cartesian grid. The grid is staggered according to the Marker and Cell (MAC) method [73], meaning that all scalars are stored at cell centres and velocity vectors are stored at the cell faces.

In the VOF method the interface is tracked by transporting an additional field variable, f, representing the volume fraction of liquid in the cell

$$f = \begin{cases} 0 & \text{in the gas phase} \\ ]0,1[& \text{in interface cells} \\ 1 & \text{in the liquid phase} \end{cases}. \tag{4.3}$$

Using f as the phase indicator, the fluid properties are volume-averaged in cells that contain both phases. The density and viscosity are thus

$$\rho = \rho_\ell f + \rho_v (1 - f) \tag{4.4}$$

and

$$\mu = \mu_\ell f + \mu_v (1 - f), \tag{4.5}$$

where the subscripts ℓ and v denote the known properties of the liquid and vapour phases, which are constant assuming incompressibility and constant temperature in each phase. The VOF transport equation can be written as [56]

$$\frac{\partial f}{\partial t} + \nabla \cdot (f \boldsymbol{u}_\Gamma) = \frac{-\dot{m}'''}{\rho_\ell}, \tag{4.6}$$

where $\boldsymbol{u}_\Gamma$ is the interface velocity and $\dot{m}'''$ is the volumetric vaporization rate at the interface, such that the right hand side of the equation accounts for the volume of liquid being consumed.

Using an efficient multi-grid solver ([74]), the pressure field p is obtained iteratively by projecting the velocity field given by the momentum equation until the

pressure Poisson equation,

$$\nabla \cdot \left[\frac{1}{\rho}\nabla p\right] = \frac{\nabla \cdot \boldsymbol{u}}{\Delta t}, \tag{4.7}$$

is satisfied. Here, ρ is given by Eq. (4.4) and an assumption of incompressibility in each phase is maintained, implying a null velocity divergence term ($\nabla \cdot \boldsymbol{u} = 0$) in the pure phase regions. However, in cells containing the interface ($0 < f < 1$), $\nabla \cdot \boldsymbol{u}$ must be determined as a function of the vaporization rate, $\dot{m}'''$, to account for the volume of vapour generated. This is detailed in the following section.

For the numerical integration, a second order upwind scheme is employed for the advective terms and a second-order central difference scheme for the diffusive terms. The time integration is first order Euler explicit. The time step is dynamically adjusted to ensure a stable CFL condition for the maximum velocity or limited by the explicit stability constraint for viscous transport or capillary wave propagation.

4.1.1 PLIC interface reconstruction

To compute accurate fluxes of the VOF variable (Eq. (4.6)) and prevent numerical diffusion of the interface, the piecewise linear interface calculation (PLIC) method [75] is used. For each finite volume cell the interface is approximated by a plane that is orthogonal to the local normal vector given by the gradient of f as

$$\hat{\mathbf{n}}_\Gamma = -\frac{\nabla f}{\|\nabla f\|}. \tag{4.8}$$

Then, the location of the plane is adjusted such that the volume bound by it within the cell matches the f value. Figure 4.1 shows a representation of the numerical treatment of the fluid-vapour interface. The real interface shown in (a) is discretized and represented by the scalar f in (b). (c) shows the PLIC reconstructed interface. The geometric reconstruction also provides an approximation to the interface area density, a_Γ, given by the area of the PLIC plane divided by cell volume.

4.1.2 Phase change

According to the continuity equation (4.1), the velocity field is divergence free ($\nabla \cdot \boldsymbol{u} = 0$) only in cells where the density ρ is constant. At the liquid interface, where phase change takes place, $\dfrac{\partial \rho}{\partial t} \neq 0$ and $\nabla \cdot \boldsymbol{u}$ must be determined, acting as a source term in the pressure Poisson equation (4.7). The method implemented by Schlottke and Weigand [56] takes into account the interface reconstruction to

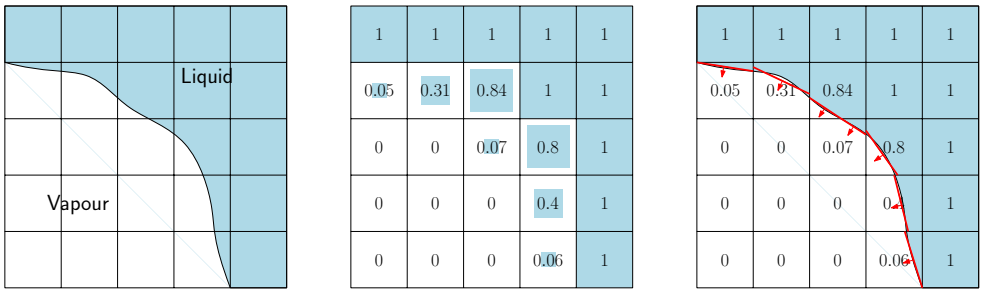

(a) (b) (c)

Figure 4.1: 2D representation of the liquid-vapour interface in a bubble using of the Volume of fluid field and PLIC reconstruction.

determine the fluxes of the liquid and vapour phases across partially wet cell faces. With $\boldsymbol{f}_A$ being the "wetted" area, sub-grid velocities for the liquid interface, $\boldsymbol{u}_\Gamma$, and vapour phase, $\boldsymbol{u}_v$, are computed such that the volume balance

$$\nabla \cdot \left[\boldsymbol{u}_\Gamma \boldsymbol{f}_A + \boldsymbol{u}_v \left(1 - \boldsymbol{f}_A\right)\right] = -\dot{m}''' \left(\frac{1}{\rho_v} + \frac{1}{\rho_\ell}\right) \tag{4.9}$$

is satisfied. Then, $\nabla \cdot \boldsymbol{u}$ is obtained based on a virtual mass-weighted velocity $\boldsymbol{u}^*$, viz.

$$\nabla \cdot \boldsymbol{u} = \nabla \cdot \boldsymbol{u}^* \equiv \nabla \cdot \left[\boldsymbol{u}_\Gamma \boldsymbol{f}_A \rho_\ell + \boldsymbol{u}_v \left(1 - \boldsymbol{f}_A\right) \rho_v\right] \tag{4.10}$$

that is consistent with the mass-weighted velocity obtained in the momentum conservation Eq. (4.2). The resulting $\boldsymbol{u}_\Gamma$ is also used in the advection term of Eq. (4.6). When considering the velocity divergence $\nabla \cdot \boldsymbol{u}^*$, the pressure field resulting from Eq. (4.7) naturally introduces in Eq. (4.2) the necessary jump condition for pressure and momentum at the interface.

In the case of expanding bubbles and the setup used in this work, no external forces or pressure gradients are present, except for the surface tension forces. The divergence of the velocity field at the bubble interfaces is thus the main and only driver of the breakup process. Defining the vaporization rate as

$$\dot{m}''' = a_\Gamma \dot{m}'', \tag{4.11}$$

the flow is then governed by the mass flux across the interface $\dot{m}''$. In this work it is introduced as an external parameter in addition to the other material properties of the fluid, all of which are calibrated to account for thermodynamic effects according the models of Chap. 3 as described in Sec. 4.2.

4.1.3 Surface tension

The surface tension is introduced in Eq. (4.2) as continuous volumetric force, $\boldsymbol{f}_\sigma$ that acts only in the vicinity of the interface. In the `FS3D` code, different surface tension models are available, including the continuum surface force (CSF) and the balanced continuum surface force (bCSF). While the plain CSF model is known to generate spurious currents, this is solved by the bCSF [72]. However, the latter makes use of height functions that extend beyond the interface and is not sufficiently flexible to capture poorly resolved regions. These are necessarily present upon topological changes of the interface (i.e., bubble coalescence and liquid breakup). Thus, in this work, the continuum surface stress (CSS) model by Lafaurie et al. [76] is used (for further details see also [56, 77]).

The CSS model makes use of a smoothed phase indicator field $\tilde{f}$ to define

$$\boldsymbol{f}_\sigma = \nabla \cdot \left(\sigma \|\nabla \tilde{f}\| \left[\mathbf{I} - \tilde{\boldsymbol{n}}_\Gamma \tilde{\boldsymbol{n}}_\Gamma \right] \right) \tag{4.12}$$

where $\|\nabla \tilde{f}\|$ represents a smoothed surface area density and $\tilde{\boldsymbol{n}}_\Gamma = -\nabla \tilde{f} / \|\nabla \tilde{f}\|$ its normal vector. The smoothing operator [56] causes the surface tension force to be distributed on the vicinity of the interface rather than acting as a point-like force in the cell containing the interface. This helps reduce the generation of parasitic currents due to the interface discretization. The smoothing operator acts on a stencil of $3^3 = 27$ cells, meaning that the f field is smeared by one cell in each direction around the reference point. The divergence operator in Eq. (4.12) is also carried out in stencils of 27 cells. This means that, in total, the surface tension in a given point is influenced by the f value in a stencil of $5^3 = 125$ cells. This contrasts with the PLIC reconstruction that through Eq. (4.8) depends only on the 26 cells in the immediate vicinity. As a consequence, it may occur that artificial surface tension forces are generated when two interfaces approach each other at a distance that is less than 4 computational cells, while the PLIC reconstruction would lead to a topological change only when that distance is less than 3 cells. While this effect should not cause a significant influence in the overall fluid dynamics if the main interface features are reasonably resolved, non-physical dynamics can be introduced in certain situations, notably in flat lamellae resulting from head-on droplet collisions [77] and from bubble coalescence process in the high Weber regime that is one of the focus points of the present work (Sec. 5.2.1).

4.2 DNS case definition and setup parameters

The multi-phase simulations are performed with the goal of observing the droplet formation in a flash boiling jet. However, due to the discrepancy of length scales involved, it is currently not practical to perform simulations of the complete jet and spray plume while resolving the complex liquid breakup mechanisms and thermodynamic effects. Using the assumption of fluid incompressibility, DNS of the atomization process can be performed at achievable computational cost. The pure fluid-mechanical processes at the microscopic scale are focused, on a domain representing a small section of the jet. Thermodynamic effects associated with bubble growth (Chap. 3) are introduced by calibration of key properties and variables as functions of the relevant free setup parameters.

To define the DNS domain we start by contextualizing it within the macroscopic flow expected for a typical injector. Depending on the injector design, different flow structures can be expected (cf. [35, 43, 20, 21]). As depicted in Fig. 4.2, cryogenic liquid initially stored in subcooled conditions at temperature T_ℓ and pressure p_0 is released through a cylindrical nozzle into the low pressure combustion chamber at p_{chamber}. Also depicted is a hypothesized pressure profile along the nozzle. The sharp angle at the entrance of the orifice can lead to the formation of a vena contracta and cavitation. Then, along the nozzle, bubbles may nucleate heterogeneously at the walls or homogeneously within the liquid bulk. This leads to a two phase flow where the pressure remains below the saturation condition but still relatively high in relation to the chamber. Due to the low speed of sound in the two phase flow, a sonic condition develops in the nozzle (chocked flow) and the mass flow rate becomes independent of the pressure differential. At the exit of the nozzle, the fluid is no longer bounded by the injector walls, expands and accelerates causing the final pressure drop towards the chamber pressure.

Given experimental observations [19, 26, 23, 27] of nearly 180 degrees of jet spreading for high superheat levels, it is evident that the radial expansion of the spray is driven by bubble expansion and atomization soon after crossing the nozzle exit. This is thus the region of interest for DNS, even in the (expected) case that the phase change process may start inside the nozzle. As the DNS domain cannot always cover the entire cross-section of the flash-boiling jet, the focus is on a small control-volume of liquid emulating a fluid element moving with the jet velocity. The control-volume can represent a section of the jet bulk or a large liquid blob previously detached by shattering. Within this volume, a finite number of bubbles nucleates. It is assumed that no macroscopic velocity gradients exist across the

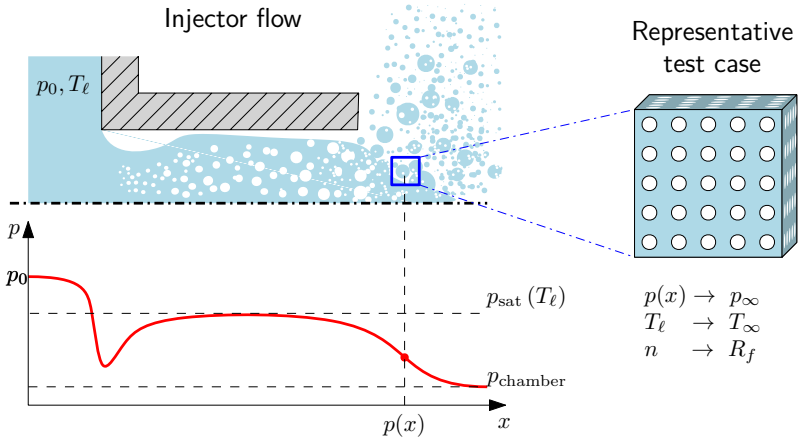

Figure 4.2: Schematic of flashing flow in the injector with hypothesised pressure profile and representative test case relating the local conditions of pressure, $p(x)$, liquid temperature, T_ℓ, and bubble number density, n, to the free parameters of the DNS p_∞ and T_∞ and expected coalescence radius (R_f).

domain and that the bubbles are initially at rest relative to the control volume and each other. Buoyancy forces due to acceleration or gravity are also neglected. The environment conditions for the DNS, that are the far-field liquid temperature T_∞ and pressure p_∞ identified in Chap. 3 for individual bubbles, are only local and instantaneous conditions within the jet or spray. These are not necessarily known based on the injection conditions. While $T_\infty \approx T_\ell$ is a valid first assumption, a moving fluid element within the jet will experience a pressure in the range of $p_{\text{sat}}(T_\infty)$ to p_{chamber}, as described by $p(x)$. Nonetheless, since the time scale for bubble growth and breakup are much smaller than the one associated with the macroscopic flow velocity, p_∞ can be assumed constant throughout the time span of a DNS test case.

The local pressure and thus the local level of superheat can be affected by several factors beyond isentropic expansion. For very low p_{chamber}, the limit of mechanical stability given by the spinodal line (Fig. 3.1) is expected to trigger sufficient vaporization to temporarily maintain a higher local pressure. It has also been shown [60] that once bubbles nucleate and start to grow, a pressure gradient develops towards the centre of the jet further reducing the local level of superheat. Thus, the asymptotic limit of p_{chamber} may only be reached once the liquid is fully atomized or cooled to a new equilibrium. Finally, the presence of shocks [23, 19, 16] can add complexity to the pressure profile. The local pressure is thus very hard to estimate for a given set of injection parameters. However, as observed in Sec. 3.4, p_∞ is expected to have a small influence during most of the bubble growth, that ultimately drives the atomization process, except for very low levels of superheat. In this context,

the local number of homogeneous bubble nuclei also cannot be reliably estimated. The local nuclei number density, n, must therefore be treated as an additional free parameter for the DNS. Since n determines the average spacing between bubbles and thus how much each bubble can expand until it coalesces with its neighbours, it determines the average bubble size at the point that the breakup process starts. This shall be referred the final bubble coalescence radius R_f. Assuming that within a small control volume of liquid, V_0, all bubbles coalesce simultaneously and grow at the same rate, the final radius, R_f, can be related with n by mass conservation, as will be detailed in Sec. 4.2.1.

The R_f parameter is the relevant variable for the purpose of characterizing the mechanics of droplet formation, since it provides a characteristic length for the breakup dynamics at the microscopic level, independently of the nozzle diameter that is often used as reference length for jet atomization studies. For convenience, the normalized parameter

$$R_f^* = R_f / R_{\text{crit}} \tag{4.13}$$

can be used, where R_{crit} is the critical radius (Eq. (3.8)). Thus R_f^* represents the bubble growth factor from nucleation to the start of the breakup. According to the RP-e model described in Sec. 3.4, R_f^* correlates with different stages of bubble growth for which different growth rates and surface tension coefficients are expected due to interface cooling effects.

4.2.1 Computational domain

Two main types of setup are used in the various studies performed. First the bubbles are arranged in a cubic-lattice array of equally spaced bubbles submerged in a pool of liquid (buffer zone), as depicted in Fig. 4.3 (left). This type of canonical arrangement allows a clear observation and classification of droplet formation mechanics, particularly focusing on the liquid trapped between the bubbles (interstitial liquid).

In the second approach a larger number of bubbles is randomly distributed within a large liquid blob, that is in turn surrounded by vapour, see Fig. 4.3 (right). The surrounding gas is pure vapour with the same properties as the vapour generated inside the bubbles. This setup is more realistic since it avoids perfect symmetries and a simultaneous coalescence of all the bubbles at the same radius, which can influence the droplet formation dynamics. In both arrangements the two-phase flow is free to expand through the use of continuity boundary conditions (outflow) and the buffer zones are sufficiently large to contain most of the spray generated, even though some

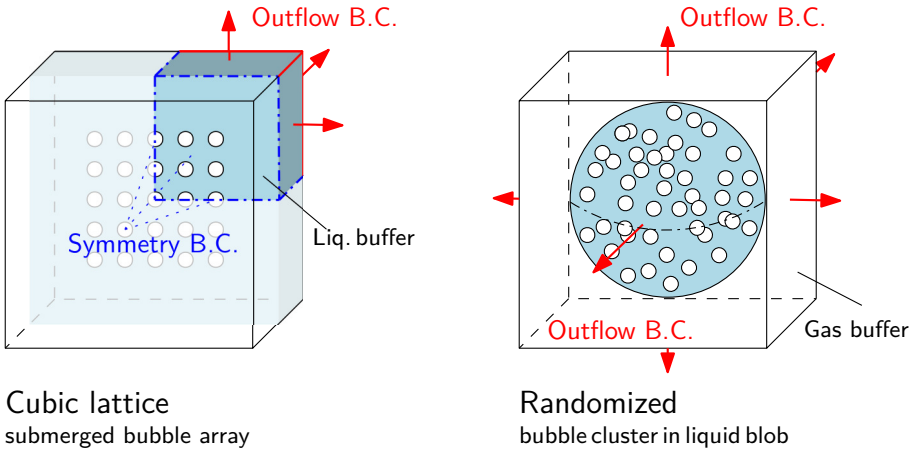

Figure 4.3: DNS domain configuration with boundary conditions used.

droplets may leave the domain. To minimize computational cost, the cubic lattice arrangement uses symmetry boundary conditions. In the case of irregular bubble distributions, no symmetry conditions are used.

Both cases are geometrically characterized by the number of bubbles N_{bub} and bubble number density, n, or the corresponding final bubble size, R_f. In the randomized case, however, the irregular spacing between bubbles implies that not all coalescence events will occur simultaneously or at the same bubble radius. Thus, the target R_f shall be interpreted as a mean bubble coalescence radius for the test case.

To ensure that the flow is fully developed and to allow realistic bubble deformations and interactions before coalescence, the domain is initialized with bubbles significantly smaller than the target merging size. It is essential to precisely determine the initial control volume size, V_i, that for a given N_{bub} determines the correct bubble spacing that will lead to coalescence at R_f. This is now detailed for both cubic lattice and randomized setups with the help of Fig. 4.4.

In the limit of infinitesimally small bubbles (Fig. 4.4 left) the bubble number density is

$$n = \frac{N_{\text{bub}}}{V_0}, \tag{4.14}$$

where N_{bub} is the number of bubbles included in the simulation and V_0 is a control volume of pure liquid where the bubble nuclei are initially distributed. In practice, bubbles must be distributed in a volume V_i and initialized with a finite diameter, R_i, that can be resolved by the DNS mesh (Fig. 4.4-Initialization).

At any stage of the bubble growth the total volume of vapour and liquid can be

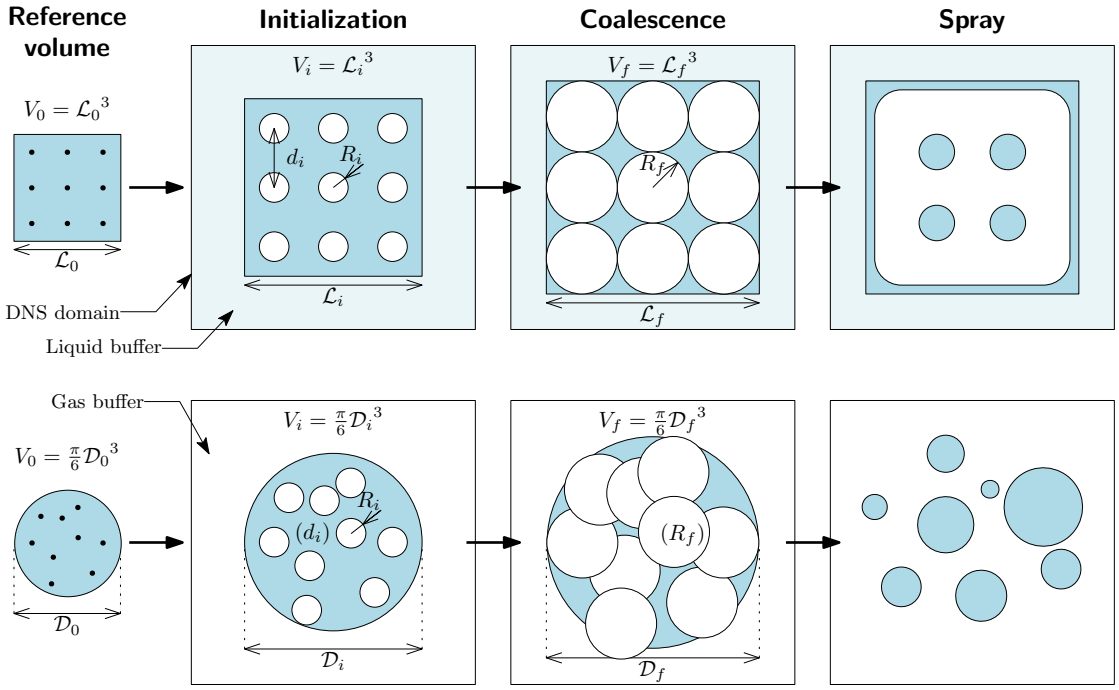

Figure 4.4: Schematic of the simulation domain definition, comparing the cubic lattice arrangement (top) with the randomized setup (bottom).

determined by mass conservation using

$$V_{\text{tot}}(R) = V_0 + \underbrace{N_{\text{bub}}\frac{4}{3}\pi R^3}_{\text{vapour generated}} - \underbrace{N_{\text{bub}}\frac{4}{3}\pi R^3\frac{\rho_v}{\rho_\ell}}_{\text{liquid consumed}}$$

$$\Leftrightarrow \quad V_{\text{tot}}(R) = V_0 + N_{\text{bub}}\frac{4}{3}\pi R^3\left(1 - \frac{\rho_v}{\rho_\ell}\right), \tag{4.15}$$

assuming constant density in both phases and equal bubble radii. With Eq. (4.15) the initial and final volumes, $V_i = V_{\text{tot}}(R_i)$ and $V_f = V_{\text{tot}}(R_f)$, are defined as depicted in Fig. 4.4-Coalescence. However, a closure relation is necessary to determine V_0 as a function of the target R_f. This can be done by imposing the final vapour volume fraction, or void fraction, η_f, assuming spherical bubbles simultaneously touching at the instant of coalescence

$$\eta_f = \frac{N_{\text{bub}}\frac{4}{3}\pi R_f^3}{V_f}. \tag{4.16}$$

Combining Eqs. (4.16) and (4.15) for $V_f = V_{\text{tot}}(R_f)$ we obtain

$$V_0 = N_{\text{bub}}\frac{4}{3}\pi R_f^3\left(\frac{1}{\eta_f} - 1 + \frac{\rho_v}{\rho_\ell}\right) \tag{4.17}$$

and

$$n = \left[\frac{4}{3}\pi R_f^3 \left(\frac{1}{\eta_f} - 1 + \frac{\rho_v}{\rho_\ell} \right) \right]^{-1} . \tag{4.18}$$

For the cubic lattice arrangement, η_f is the cubic (least dense) packing factor of equal spheres, $\eta_f = \pi/6 = 0.52$. For a randomized packing of equal spheres, no closed form for η_f exists and it can only be estimated or measured empirically. As will be shown, the amount of bubble translation and deformation that might help determine an effective η_f varies greatly depending on R_f. To reduce the number of free variables, the same $\eta_f = \pi/6$ has been selected for the randomized cases. This means that the number density, n, and the volume of liquid available in the domain to form droplets is the same (per bubble) in both setup types, for a given R_f. The sensitivity and implications of this assumption are discussed in Chap. 6.

With V_0 determined as a function of the target R_f and N_{bub}, Eq. (4.15) can be used to determine the initialization volume $V_i = V_{\text{tot}}(R_i)$. For the cubic lattice array the bubble centres are uniformly distributed. For the randomized blob, a random number generator is used to place N_{bub} within the V_i sphere of liquid [78]. The bubbles are initiated with a maximum $R_i = R_f/10$ which must be resolved by at least one grid cell in order to initiate their growth in the DNS. Since $R_i \ll R_f$, $V_i \approx V_0$.

For a given n or R_f, the size of the computational domain is ultimately determined by N_{bub}. For the simulations in cubic-lattice array, the number was selected as $5^3 = 125$, in order to ensure that at least one bubble is completely surrounded by other bubbles and not in contact with any of the symmetric boundaries or buffer zones. For the randomized cases, the number of bubbles varies from 125 to 1000, depending on computational cost limitations and the expected breakup behaviour, ensuring that it is sufficient to observe the breakup mechanics or to generate a statistically relevant number of droplets.

The effective size required for the computational domain should include not only the control volume V_f, but also allow for a significant spreading of the liquid structures throughout the breakup process. This determines the size of the buffer zone which also needs to be adjusted case-by-case according to the expected breakup behaviour. Still, the interaction of the liquid-vapour interface with the outflow cannot always be avoided, requiring the adapted boundary condition implementation described in Appendix. A.

4.2.2 Thermodynamic calibration

Vapour compressibility and interface cooling effects are not captured by the numerical methods selected for the DNS, which focuses only on the pure fluid mechanics of the breakup as captured by the Navier-Stokes equations. The driving force of the breakup process must nonetheless be the internal vapour pressure of the bubbles.

As described in Sec 4.1 the pressure field is obtained by solving the Poisson equation (4.7) while accounting for the divergence of the velocity field $\nabla \cdot \boldsymbol{u}$ at the interface cells, given by the source term $\dot{m}'''$ (Eq. (4.11)) in Eq. (4.9) as well as Eq. (4.6). The flow is thus controlled by the vaporization mass flux $\dot{m}''$, that is applied at every interface cell. $\dot{m}''$ becomes thus a global external parameter of the DNS, that is calibrated based on the RP-e solution for each case, according to T_∞, p_∞ and the target coalescence radius given by R_f^*. The same calibration approach is taken for other variables dependent on the interface temperature: the vapour density, ρ_v, viscosity, μ_v, the surface tension coefficient, σ. The properties of the liquid phase (density, ρ_ℓ, and viscosity, μ_ℓ) depend only on T_∞ and p_∞. Since when assuming bubble sphericity we have $\dot{m}'' = \rho_v \dot{R}$ (Eq. (3.17)), $\dot{R}$ acts as an imposed interface velocity relative to each bubble centre that can be conveniently used for the characterisation of the breakup dynamics.

These calibrated parameters are kept constant throughout the simulation. Even though, in some cases, they may vary significantly during bubble growth up to R_f, it is expected that the spray breakup is largely determined by the bubble growth rate at the instant of coalescence as early growth (and associated small bubble radii) does not significantly contribute to volume expansion.

The incompressible assumption is justified at the level of individual bubbles, given the relatively low bubble growth rates. However, with the geometrical setup described in the previous section, there is a cumulative effect associated with the growth rates of a given number of bubbles along a radial direction from the centre of the domain. The absolute maximum flow velocity is effectively proportional to $\sqrt[3]{N_{\text{bub}}}\dot{R}$ at the outer shells of the bubble cluster, resulting in relatively high Mach numbers. Since no compressibility effects are considered, it is implied that the relative velocity of the bubble interfaces at the outer regions of the domain are similar to the values found at the center. Such approximation is compatible with the goals of this work, but neglects important compressibility effects that will be further discussed in Sec. 6.4.

With the above assumptions and approximations the definition of each DNS case can be done in terms of three main free parameters, T_∞, p_∞ and R_f^*. The RP-e and

EOS then provide all the remaining variables necessary to solve the Navier-Stokes based system of equations of the DNS detailed in Sec 4.1.

Simulations are performed for LOx at T_∞ between 80 K and 120 K and p_∞ of 10^5 Pa to 10^3 Pa. The corresponding superheat levels and other metrics have been provided in Tab. 3.1. All of these correspond to sub-critical injection temperatures and environment pressures above the triple point, ensuring a two phase flow. R_f^* values tested vary between 2 and 50, covering the surface tension, inertial and transition stages of growth described in Sec. 3.3. For ease of comparison and interpretation, the DNS cases will be labelled A to D indicating decreasing levels of superheat according to Table 3.1, followed by a number corresponding to R_f^*. For example, case B-10 corresponds to $T_\infty = 100\,\mathrm{K}$, $p_\infty = 10^3\,\mathrm{Pa}$ with $R_f^* = 10$.

The simulation time, t^{DNS}, covers the initial growth of the bubbles from R_i to R_f and the subsequent liquid breakup until most of the liquid structures have reached relatively stable sizes. These time scales also vary in order of magnitude depending on the thermodynamic conditions. Considering the constant growth rate calibrated for each case, we use $t_i = R_i/\dot{R}$, and $t_f = R_f/\dot{R}$ to define an adjusted dimensionless time

$$t^* = \frac{t^{\mathrm{DNS}} - t_i}{t_f} \approx \frac{t^{\mathrm{DNS}}\dot{R}}{R_f}, \tag{4.19}$$

implying that start of coalescence is expected at $t^* = 1$. In order to capture the complete breakup $t^* > 10$ is typically required.

Using T_∞, p_∞ and R_f^* as the primary variables that define each test case, n, V_f, R_f and t_f will vary by orders of magnitude. A complete list of setup parameters for the series of cases simulated can be found in Appendix D. Between case A-2 (highest superheat, $R_f^* = 2$) and case D-50 (lowest superheat, $R_f^* = 50$), the following ranges apply

$$\begin{aligned} n &\in [2 \times 10^{22}, 8 \times 10^{14}]\,/\mathrm{m}^3 \\ t_f &\in [3 \times 10^{-9}, 2 \times 10^{-6}]\,\mathrm{s} \\ R_f &\in [2 \times 10^{-8}, 7 \times 10^{-6}]\,\mathrm{m} \\ \sqrt[3]{V_f} &\in [5 \times 10^{-7}, 7 \times 10^{-5}]\,\mathrm{m}. \end{aligned} \tag{4.20}$$

Chapter 5

Results

This chapter covers the main results on liquid breakup mechanics under flash boiling conditions, obtained using the DNS methods described in Chapter 4. Section 5.1 focuses on a qualitative analysis of the breakup behaviour across the range of test cases using the cubic-lattice setup. A predictive classification model is proposed, that is also used as a reference for the subsequent study. Although the findings have been first proposed in the author's publication Loureiro et al. [1], the simulations and results shown here take into account later investigations and are based on Loureiro et al. [4]. Section 5.2 discusses resolution criteria including a predictive droplet size estimator that serves as basis for quantitative models. Mesh-dependency effects are also evaluated. This section is based on the results presented in Loureiro et al. [2]. Finally, Sec. 5.3 presents the results of the DNS performed with the randomized setup, towards obtaining statistical droplet size data as well as the time-evolution of total spray surface area. From these results DNS-calibrated models are proposed. These results are based on the final publication Loureiro et al. [5].

The complete list of setup parameters defined for each case according to Sec. 4.2 can be found in Appendix D. Numerical data presented in Secs. 5.2 and 5.3 makes use of the post-processing methods and definitions provided in Appendix C.

5.1 Breakup patterns and flow characterization

To observe and understand the breakup mechanics, the cubic lattice arrangement allows for the most clarity on the interaction between individual bubbles and liquid flow leading to droplet formation. For this analysis, all simulations are initialized to represent a $5 \times 5 \times 5$ array of bubbles assuming simultaneous nucleation of equal bubbles, with varying spacing determined by the R_f^* parameter and thermodynamic

parameters determined by T_∞ and p_∞, as outlined in Sec. 4.2. The complete list of setup parameters is provided by Tab. D1 in Appendix D. A typical result is shown in Fig. 5.1, obtained by rendering the $f = 0.5$ iso-surface of the VOF field at different moments of the simulation. The visualization is from the perspective facing one of the symmetric boundaries, effectively showing 1/8 of the physical domain. The normalized time t^* (Eq. (4.19)) is used to refer to different steps in the sequence.

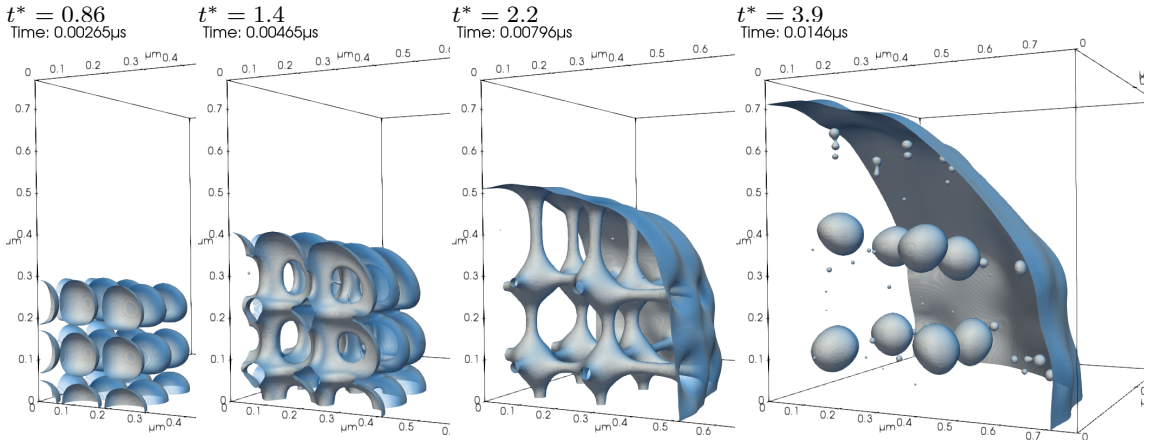

Figure 5.1: Breakup sequence example (Case A-5) in cubic lattice arrangement.

The first image of the sequence ($t^* = 0.86$) is obtained just few nano-seconds after the start of the simulation, showing bubbles after the initial rapid growth and just before they collide with their neighbours. The bubbles in the first plane are sectioned by the boundary and the whole cluster is surrounded by liquid. Some degree of bubble deformation is observable as the bubbles "push" against each other in the cubic arrangement. At $t^* = 1.4$ (note that bubble coalescence is implied to start at $t^* = 1$) the liquid separating the bubbles has been punctured and all the vapour volumes are inter-connected, leaving a matrix structure of liquid ligaments. These ligaments stretch as the vapour volume further increases ($t^* = 2.2$). Towards the upper, right and back sides of the domain, the interface of the now coalesced bubble pushes against the surrounding liquid and grows towards a spherical shape. This outer interface, however, has no physical significance as it is only a consequence of the use of a liquid buffer in lieu of an infinite pool of submerged bubbles. In the final step ($t^* = 3.9$) the liquid ligaments have broken, releasing an array of large primary droplets surrounded by some small satellites. This archetypal behaviour is somewhat expected and is comparable to the *bubble coalescence* in densely packed arrangement previously proposed by previous works [7, 38]. However, it will be shown here that by varying the free parameters, R_f^*, T_∞ and p_∞, the breakup behaviour can be substantially different.

As described in the previous chapters, the thermodynamic state corresponding to a given T_∞ and p_∞ implies a specific behaviour for bubble growth according to the RP-e model solution. Within each solution R_f^* corresponds to a point when the bubbles reach the size $R = R_f$, providing the growth rate $\dot{R}$ and surface tension coefficient σ at the moment of coalescence. Also important are the density and viscosity of the liquid, ρ_ℓ and μ_ℓ (that depend primarily on T_∞), while the saturated vapour properties μ_v and ρ_v (also functions of R_f) play a minor role. With these variables, dimensionless numbers can be defined that shall be used, first, to characterize the breakup dynamics and later, to establish mesh resolution criteria and predictive models for the expected droplet size.

The dynamics of liquid breakup processes are typically characterized by the Weber and Ohnesorge numbers. The final bubble diameter, $2R_f$, and the interface velocity, $\dot{R}$, are used as characteristic scales to define

$$\mathrm{We}_b = \frac{2R_f \rho_\ell \dot{R}^2}{\sigma}. \tag{5.1}$$

Here the subscript b denotes a bubble characterization instead of the conventional definitions (droplet or jet diameters) used in spray atomization literature. As such, We_b represents the relative strength of the bubble surface tension force against liquid momentum due to bubble expansion. Similarly, the Ohnesorge number can be defined as

$$\mathrm{Oh}_b = \frac{\mu_\ell}{\sqrt{2R_f \rho_\ell \sigma}}, \tag{5.2}$$

to represent the strength of viscous dissipation (in the liquid) against the product of liquid inertia and surface tension. The Ohnesorge number is thus also representative of how strongly the capillary waves are dissipated by viscosity. These definitions are used to locate the different cases in the Weber-Ohnesorge diagram presented in Fig. 5.2 as functions of T_∞ and R_f^* (iso-lines), where the intersection points correspond to test cases simulated in this work. For clarity, only $p_\infty = 10^3\,\mathrm{Pa}$ cases are shown, as influence of p_∞ is small and cases with $p_\infty = 10^5\,\mathrm{Pa}$ fall in the same region.

In the diagram of Fig. 5.2 three breakup regimes are identified, the *Retracting liquid*, the *Ligament stretching* and the *Thin lamella*, associated with respective We_b ranges. This classification is a result of the breakup behavior observed in the series of DNS test cases that will now be compared in detail. Figure 5.3 provides the breakup sequences for cases A-2, A-10 and A-50. These correspond to $T_\infty = 120\,\mathrm{K}$ with higher Oh_b numbers (stronger effect of liquid viscosity), to demonstrate the

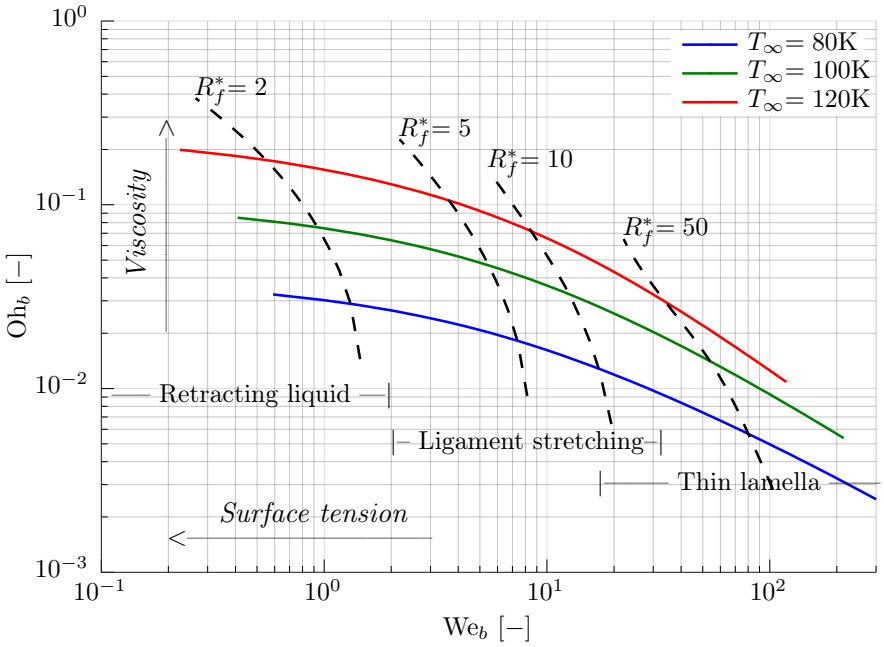

Figure 5.2: Weber-Ohnesorge diagram to characterize the type of breakup. The correlation to the physical simulation parameters is shown by the T_∞ and $R_f^* = R_f/R_{\text{crit}}$ lines, which are based on the RP-e model for superheated LOx at $p_\infty = 10^3$ Pa.

effect of varying We_b.

The first sequence, Case A-2 in Fig. 5.3(a), is initialized for $R_f^* = 2$, which can be interpreted as a high bubble number density such that bubbles merge soon after nucleation. In this case, with $We_b = 0.54$, the surface tension force dominates over the liquid momentum driven by vapour pressure. The bubbles remain largely spherical until they collide with their neighbours ($t^* = 0.88$). The gas coalesces into a single continuous volume containing the large connected structures left from the interstitial liquid ($t^* = 1.5$). Up to this point the behaviour is similar to the one previously observed for case A-5 in Fig. 5.1. However, once the ligaments break from the outer bubble interface, in $t^* = 2.4$, the thick ligaments retract, pulling the still connected liquid fluid elements from the original positions between the bubbles. Some ligaments that are thinner due to fluctuations in the initial bubble position will break, while the dominant ones can pull multiple volumes together into eventually spherical drops ($t^* = 6.3$). This behaviour was classified as *retracting liquid* and is generally observed for all cases with $We_b < 2$. The result is a droplet-merging effect, becoming larger relative to the bubble size. It should be clarified that even though the drops appear large, they are of the order of 50 nm when taking into account the scale of the domain and can actually be much smaller than the ones

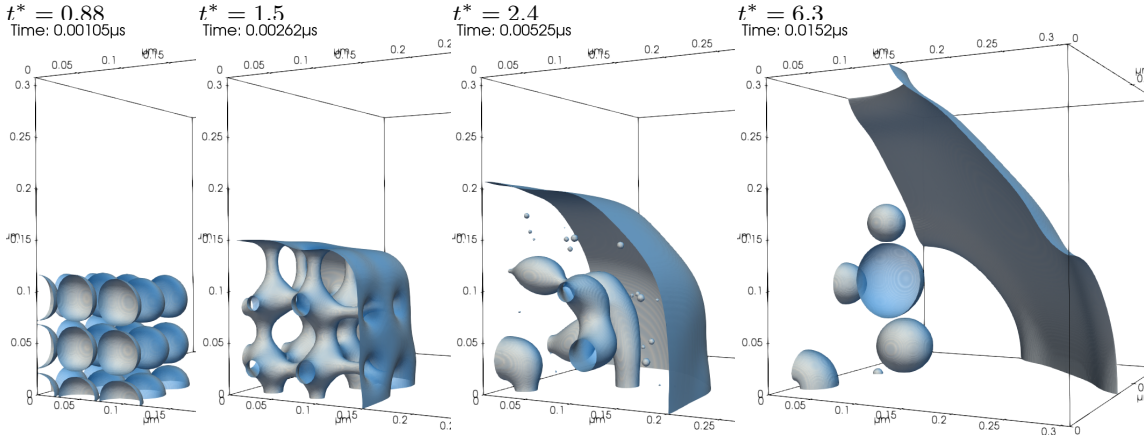

(a) Case A-2: $R_f^* = 2$ $\mathrm{We}_b = 0.54$ $\mathrm{Oh}_b = 0.17$

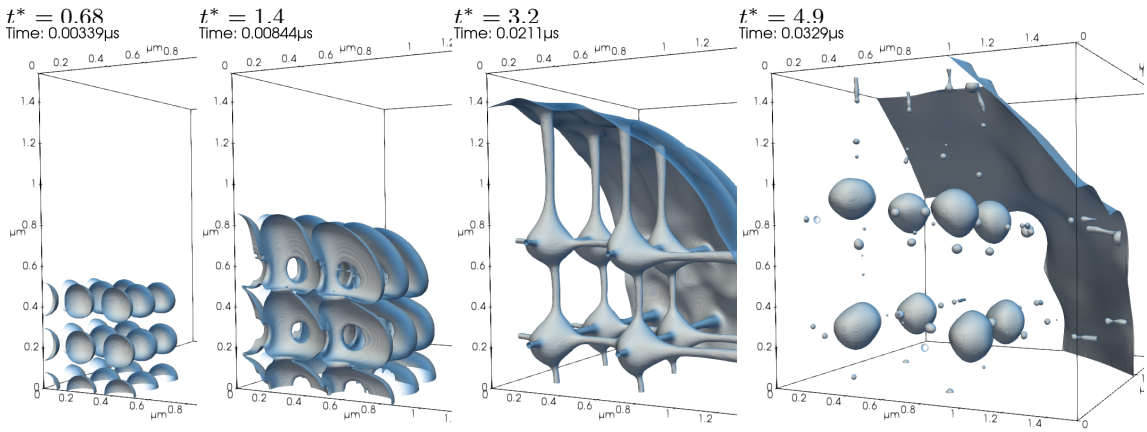

(b) Case A-10: $R_f^* = 10$ $\mathrm{We}_b = 8.4$ $\mathrm{Oh}_b = 0.071$

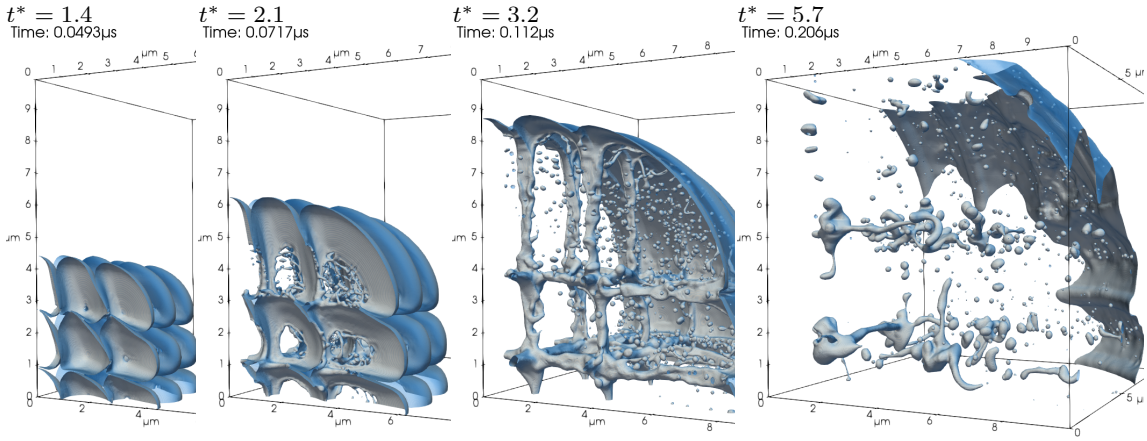

(c) Case A-50: $R_f^* = 50$ $\mathrm{We}_b = 34$ $\mathrm{Oh}_b = 0.029$

Figure 5.3: Breakup sequences for regular array cases A-2, A-10 and A-50 at relevant points of normalized time t^*, showing the effects of varying We_b given by different R_f^* with $T_\infty = 120\,\mathrm{K}$ and $p_\infty = 1000Pa$.

observed for the other cases shown as the latter represent physically larger domains. Furthermore, some of the drops form while in contact with the symmetry boundary conditions and thus are only partially visualized. Also important is the fact that the behaviour we are trying to observe is somewhat hindered by the high degree of symmetry and regularity of the setup. For this reason small randomized deviations are introduced to the initial nuclei position. This artificial effect is later avoided with fully randomized nuclei clusters (Sec. 5.3).

Towards higher We_b, the second sequence (Fig. 5.3(b)) is Case A-10, which starts with a process similar to case A-2, but with bubbles slightly deviating from spherical shape as they grow. At $t^* = 1.4$ the bubbles have touched, forming holes that quickly grow radially as the surface tension force minimizes the total area. At $t^* = 3.2$ the matrix of connected interstitial liquid volumes now stretches as the momentum of the main volumes is able to overcome the surface tension force of the ligaments. The ligaments eventually break and quickly retract to form a regular array of droplets ($t^* = 4.9$). This behaviour is observed in the range $2 < We_b < 20$ and was classified as *stretching ligaments*. Within the range, a different behaviour is also observed for the ligament breakup. For $We_b > 5$, the pinching of the ligaments occurs simultaneously at two points close to the main droplets, creating a satellite droplet. At lower We_b the ligaments instead pinch closer to their mid point suppressing the satellite formation, as observed previously in case A-5 (Fig. 5.1). It should be noted, however, that at every pinch point even smaller satellites can be generated, down to the scale of the mesh resolution, as will be further discussed. As a consequence of the cubic array arrangement, the size of the main droplets is approximately equal to the final bubble size and it can be extrapolated that the number of droplets would equal the initial number of bubbles in an infinite array.

Finally, we turn our attention to the *thin lamella* regime found for large R_f^* and We_b cases towards the right of of the We_b-Oh_b map of Fig. 5.2. At high We_b the surface tension force is relatively weak, allowing the bubbles to deform as they grow, forming a flat interface when they collide with their neighbours as shown for Case A-50 of Fig. 5.3(c). The lamellae, i.e., the thin film of liquid trapped between two bubbles, remain hydro-dynamically stable as they experience a similar pressure from the vapour on both sides. The surface tension force also acts to smooth local thickness variations. However, phase change continues at the surface, meaning that the lamella will get progressively thinner and stretched. When they break ($t^* = 2.1$) they can either generate a large number of very small droplets, or form a ring that retracts with high velocity, shedding droplets and ligaments. This particular process

will be analised in greater detail in Sec. 5.2.1, in particular regarding inherent mesh dependent effects. Still, this represents only part of the spray formation process at high We_b numbers, as seen at $t^* = 3.2$, where large liquid structures remain from the interstitial liquid. Contrary to previous cases, here the surface tension force is very weak, causing the ligaments to break simply due to vorticity and other fluctuations in the flow. As a result, there is a wide distribution of droplet sizes and irregular ligament shapes, shown at $t^* = 5.7$. The volume of liquid in the main interstices available to form these droplets is much smaller relative to the final bubble size, however, again, the resulting droplets only appear smaller in this visualization and can be physically larger than Cases A-2 and A-10 when taking into account the scale of the domain. It is also evident that these droplets are highly irregular in their shape motivating the use of a Sauter Diameter (see Appendix Sec. C3) with independent area and volume measurements for each droplet when estimating an equivalent average diameter.

The effect of the Oh_b number can be observed in cases C-2 and C-5 shown in Fig. 5.4. In terms of We_b and breakup regime, these are similar to cases A-2 and A-10 respectively. Here the lower liquid temperature implies a reduction in viscous dissipation that was in part responsible for the smooth surface of the droplets observed earlier. The result is droplets that are highly irregular with surface oscillations and additional satellite formation. It can be surmised that this can have an enhancing effect on secondary atomization driven by aerodynamic interaction with the surrounding gas. The Oh_b number is also low for cases with large R_f^* (note trend in Fig. 5.2) playing a role in the highly irregular breakup of the ligaments, such as case A-50. It is important to note that a reduced relative strength of viscosity is also indicative of the onset of turbulent flow behaviour. Even though the liquid structures are too small to observe any internal turbulence patterns, this type of breakup is comparable to aerodynamic breakup and would be largely affected by the macroscopic flow gradients not covered by the DNS. Also particularly for cases with high We_b and low Oh_b, it was observed that the droplets formed were close to the cell size, suggesting the need to define resolution criteria and evaluate mesh dependence effects, that are covered in the following sections.

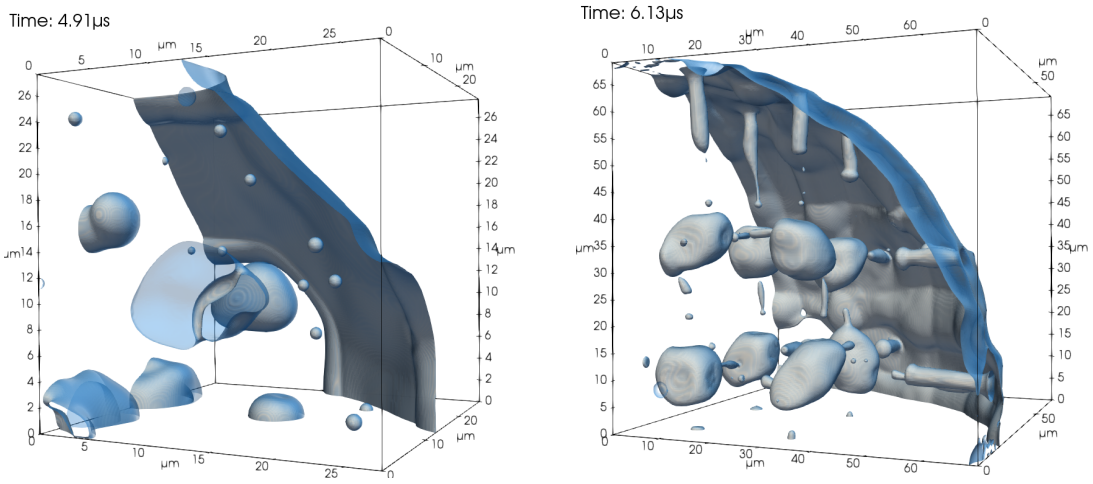

(a) Case C-2 at $t^* = 5.1$
$R_f^* = 2$, $\mathrm{We}_b = 1.3$, $\mathrm{Oh}_b = 0.029$

(b) Case C-5 at $t^* = 3.6$
$R_f^* = 5$, $\mathrm{We}_b = 7.4$, $\mathrm{Oh}_b = 0.018$

Figure 5.4: Resulting spray for regular array cases with low Oh_b ($T_\infty = 80\,\mathrm{K}$) showing irregular main droplets and larger satellites.

5.2 Resolution criteria and droplet size estimator

The flow can be characterized in terms of laminar or turbulent behaviour by the Reynolds number, defined for the liquid phase as

$$\mathrm{Re}_b = \frac{\sqrt{\mathrm{We}_b}}{\mathrm{Oh}_b} = \frac{\rho_\ell \dot{R}_f 2R_f}{\mu_\ell}. \tag{5.3}$$

For $2 < R_f^* < 100$ the range is $1 < \mathrm{Re}_b < 200$ at $T_\infty = 120\,\mathrm{K}$ and $10 < \mathrm{Re}_b < 3000$ for $T_\infty = 80\,\mathrm{K}$, with the later indicating a possible transition to a turbulent regime within the liquid phase. For the gas phase, $\mathrm{Re}_{b,v}$ can be estimated using μ_v and ρ_v and is generally one order of magnitude lower than the liquid, due to the large ratio of kinematic viscosities.

Using Kolmogorov's theory [79], the length scale of turbulent dissipation (smallest eddies) can be estimated as

$$\eta_\mathrm{K} = 2R_f / \mathrm{Re}_b^{3/4}, \tag{5.4}$$

where $2R_f$ has been taken as the integral length scale (rather than a length associated with the control volume size) to maintain independence of N_bub. As noted in Sec. 2.3.2, this metric has been used in the literature for multiphase DNS [50, 53, 54] as a resolution criterion. In particular for atomization processes the Hinze scale [31]

can also be used to estimate the size of the smallest droplet based on liquid-vapour shear interaction (aerodynamic breakup). However, in the present application of flash atomization, droplets are expected to form at scales associated to the bubble size. For this context no adequate estimator was found in the literature.

A novel droplet size estimator is proposed here, that shall be supported by the results presented in the following sections. The estimator can be obtained by equating the dynamic pressure (or volumetric kinetic energy) in the liquid accelerated by bubble growth, that is proportional to $\rho_\ell \dot{R}^2/2$, with the Laplace pressure (or volumetric surface energy) $4\sigma/D$ of the resulting droplet[1]. This results in the reference droplet diameter

$$D_{\text{ref}} = \frac{8\sigma}{\rho_\ell \dot{R}^2}. \tag{5.5}$$

Combining Eqs. (5.1) and (5.5) we obtain

$$D_{\text{ref}} = \frac{16}{\text{We}_b} R_f. \tag{5.6}$$

Even though several droplets may be formed per bubble and the contact of several bubbles is necessary to form each droplet, D_{ref} is expected to emerge as the average value based on total energy conservation. It should be noted, however, that droplets smaller than D_{ref} are still expected to form due to capillary effects such as pinching.

Just like We_b, the reference droplet size D_{ref} is evaluated considering $\dot{R}(R_f)$ and $\sigma(R_f)$ given by the RP-e solution (Sec. 3.4). The results are plotted in Fig. 5.5 as functions of the merging bubble radius, R_f. Equation (5.6) is used to map the three main breakup regimes earlier noted in Fig. 5.2, with the approximate transitions given by $\text{We}_b = 2$ and $\text{We}_b = 20$ lines. The centre band corresponding to the *ligament stretching* shows that expected droplet size is similar to final bubble size, as observed in the results of Sec. 5.1.

A notable result is the observation of a minimum in the $D_{\text{ref}}(R_f)$ curve that corresponds to the peak in $\dot{R}$ according to the RP-e model (Fig. 3.2(b)). This corresponds to $R_f^* \approx 10$ to 15. For $R_f^* < 10$ surface tension dominates forming larger droplets relative to the bubble size. As R_f tends to 0, D_{ref} tends to infinity, corresponding to the equilibrium at R_{crit}. For $R_f^* > 20$, the predicted droplet size is also larger due to the effect of bubble interface cooling according to the RP-e model, that implies a reduction of $\dot{R}$ and increase of σ. In principle, any of the approximate models described in Sec. 3.3 could be used to estimate $\dot{R}(R)$ and $\sigma(R)$ and thus

[1] For ease of reading, the radius and letter R will generally be used to refer to bubble sizes, while D and diameter is used for droplet sizes.

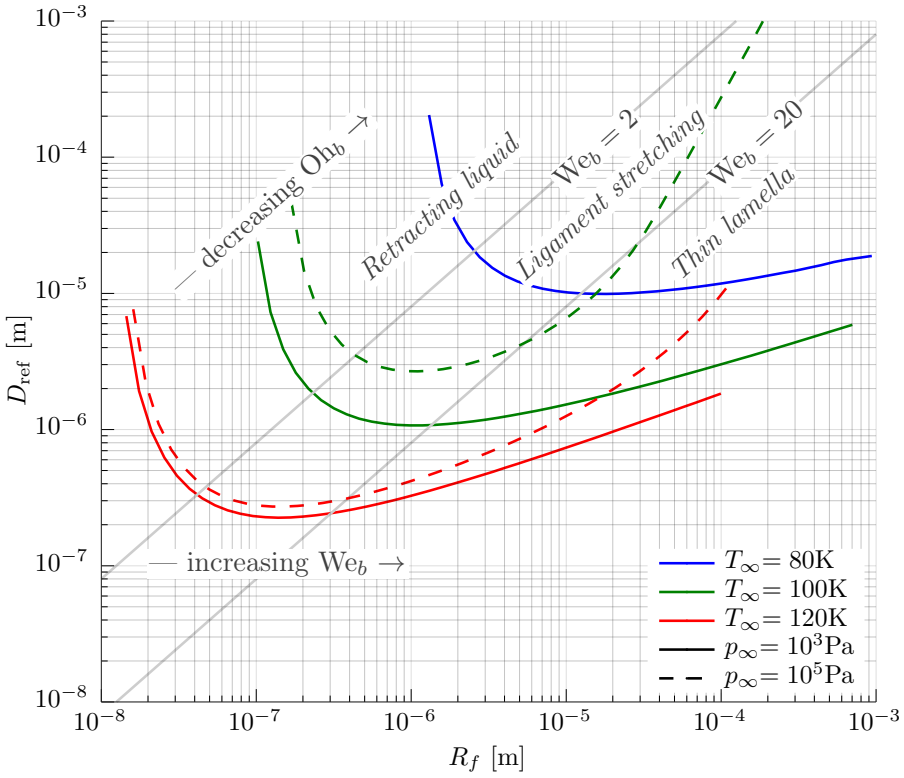

Figure 5.5: D_{ref} estimator as function of R_f based on the RP-e model for spherical bubble growth in LOx at T_∞ indicated by line colour and p_∞ by line type.

produce similar curves. However, only the RP-e is expected to be able to precisely capture the $\dot{R}$ peak, that is associated with the beginning of the *transition* stage of growth.

For the purpose of a mesh resolution criterion, both D_{ref} and η_{K} are used. Typically, for the results presented in this thesis, D_{ref} is resolved by a minimum of 15 cells. For low We_b cases, since $D_{\text{ref}} > 2R_f$, it suffices to resolve R_f by at least 10 cells. η_{K} becomes the limiting factor in cases with high We_b and Re_b (low Oh_b), where it approaches the cell size. Due to computational cost considerations (see projections in Appendix B) these criteria limit the range of test cases for which significant results can be obtained, with cases A-50 and C-10 being the limit cases for highest We_b and lowest Oh_b simulated.

5.2.1 Mesh convergence

From the regimes identified in Sec. 5.1, cases with $\text{We}_b > 20$ in the *thin lamellae* regime seem to be the most challenging, since they lead to liquid features and droplets with the smallest relative size. The process of thin lamella breakup occurs

necessarily at the limit of mesh resolution, as the thin films of liquid become progressively thinner, with no other external mechanism to promote the initial puncture. These have thus been chosen as the focus for verifying expected numerical effects and the influence of mesh resolution.

Figure 5.6 shows the final stages of lamella retraction at different resolutions. The renderings show only a thin slice of the 3D simulation domain for better visualization of the droplets resulting from a single lamella. It is observed that with increasing resolution, droplets are formed in larger numbers and with smaller sizes. At the highest resolutions, droplets and ligaments much larger than the cell size tend to shed later in the lamella retraction process. Droplets of size similar to the grid are still present in large numbers, but barely resolvable in the renderings of Fig. 5.6 c) and d). This shows that at low resolutions most droplets are likely to be artificially generated, but the numerical method is also able to capture organic droplet generation from rim instabilities during the lamella retraction process as long as sufficient resolution is provided. The size of the *real* droplets is associated with the edge diameter of the free end of the liquid film in turn regulated by Taylor-Culick mechanics [80, 81] (further discussed in Sec. 6.1). With sufficient resolution these *real* droplets become easily distinguishable from the *artificial* ones associated with the grid size.

In fact, the creation of artificial droplets is inherent to two-phase interface capturing methods, as topology changes imply the depletion of liquid in a minimum number of cells such that two independent interfaces can be reconstructed [50]. As noted in Sec. 4.1.3, for the numerical methods employed here, mesh effects are expected to be present when the distance between two parallel interfaces is less than 4 cells, that is consistent with the smallest droplet sizes observed.

The mesh effects are evaluated by computing the droplet size statistics after lamella retraction, using the methods and definitions of Appendix C. To avoid the influence of larger droplets and ligaments that may still be in the process of breaking-up for the selected point in simulation time (found e.g. in Fig. 5.6(d)), only droplets with high sphericity – drops with surface area that approaches the one of a sphere with the same volume (cf. Sec. C2) – are considered. Therefore, only for the results presented in this section, $\overline{D}_N = \overline{D}_{10}$, $\overline{D}_A = \overline{D}_{32}$ and $\overline{D}_V = \overline{D}_{43}$. The results are shown in the histograms of Fig. 5.7. It can be observed that with increasing mesh resolution, the diameter distribution based on droplet count in 5.7(a) shifts to smaller sizes (left). Conversely, the volume fraction distribution 5.7(b) seems to converge towards a normal distribution of droplet sizes, with a well defined mean

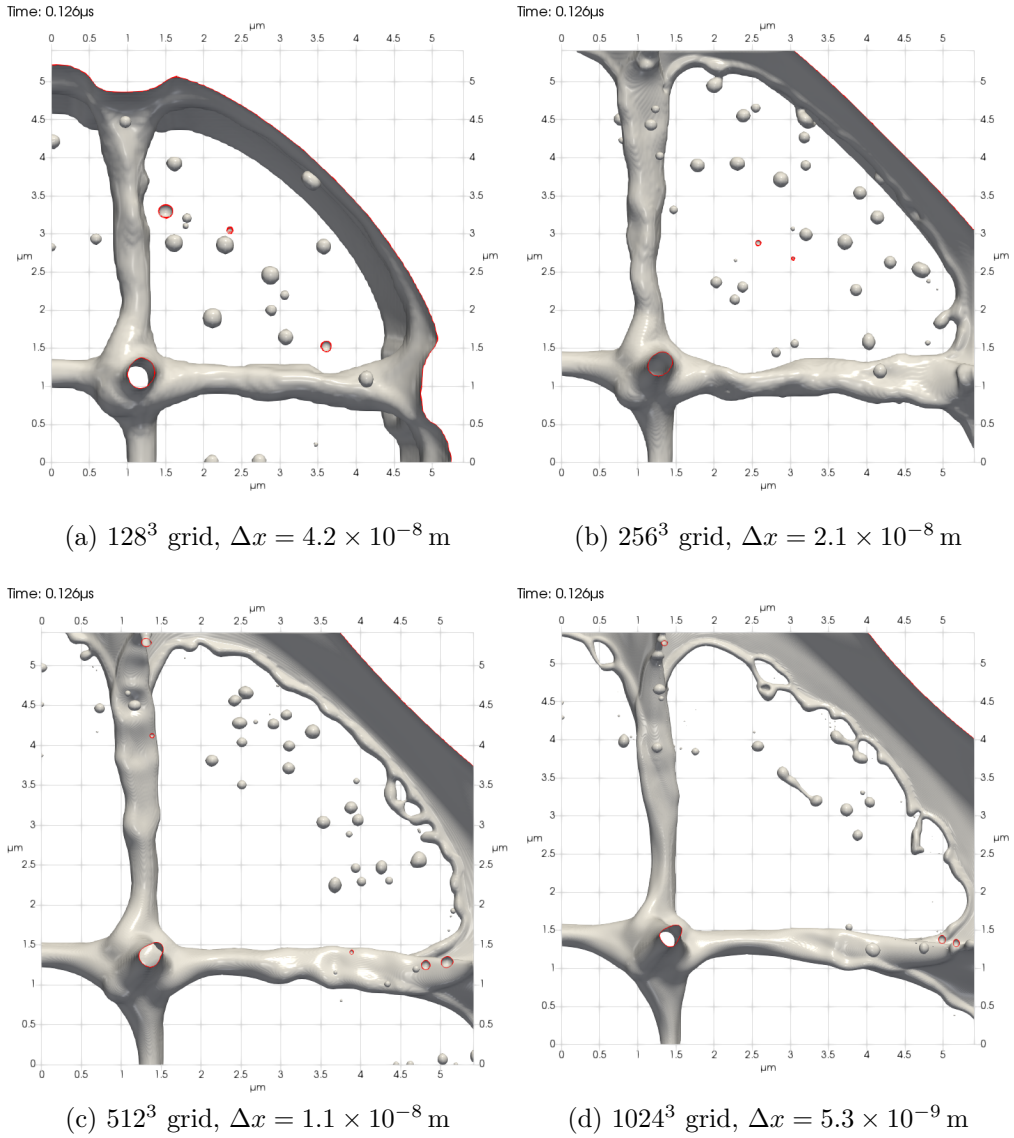

(a) 128^3 grid, $\Delta x = 4.2 \times 10^{-8}$ m

(b) 256^3 grid, $\Delta x = 2.1 \times 10^{-8}$ m

(c) 512^3 grid, $\Delta x = 1.1 \times 10^{-8}$ m

(d) 1024^3 grid, $\Delta x = 5.3 \times 10^{-9}$ m

Figure 5.6: Lamella breakup for a case A-50 ($We_b = 33$) with different grid refinements. The interface is rendered by the iso-surface $f = 0.1$.

size, as expected.

With these observations, it is proposed that the most reliable metrics are given by the area-weighted mean diameter $\overline{D}_A$ and the volume-weighted mean diameter $\overline{D}_V$, for which independence of the mesh discretization can be achieved. These are equivalent to Sauter (SMD) and De Brouckere mean diameters. However, the arithmetic mean diameter ($\overline{D}_N$) of the droplet size will always be largely influenced by the mesh resolution. The hypothesis can be observed in the graph of Fig. 5.8 showing the three mean diameters, again sampling only spherical droplets, versus the cell-count dimension of the mesh. Here the resulting cell size, Δx, and the D_{ref}

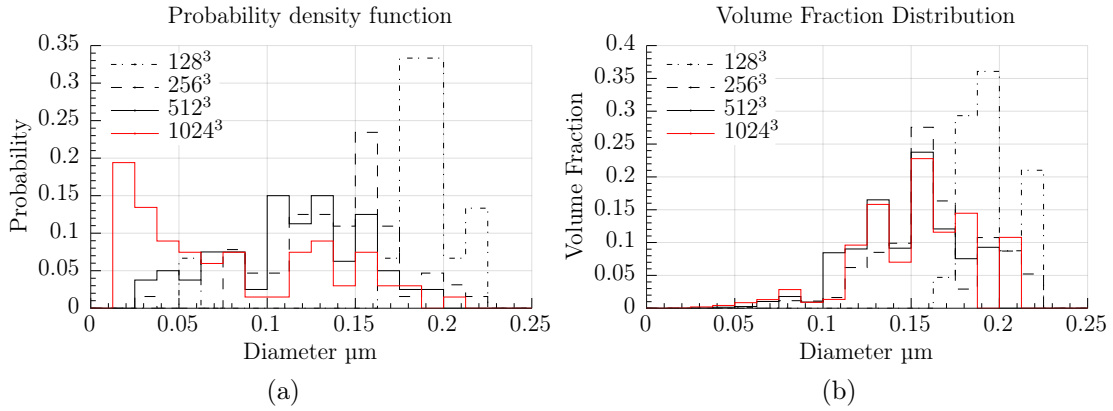

Figure 5.7: Histogram of the droplet size probability (weighted by droplet count) versus the volume fraction distribution, for increasing mesh resolutions.

estimator given by Eq. (5.5) are also compared.

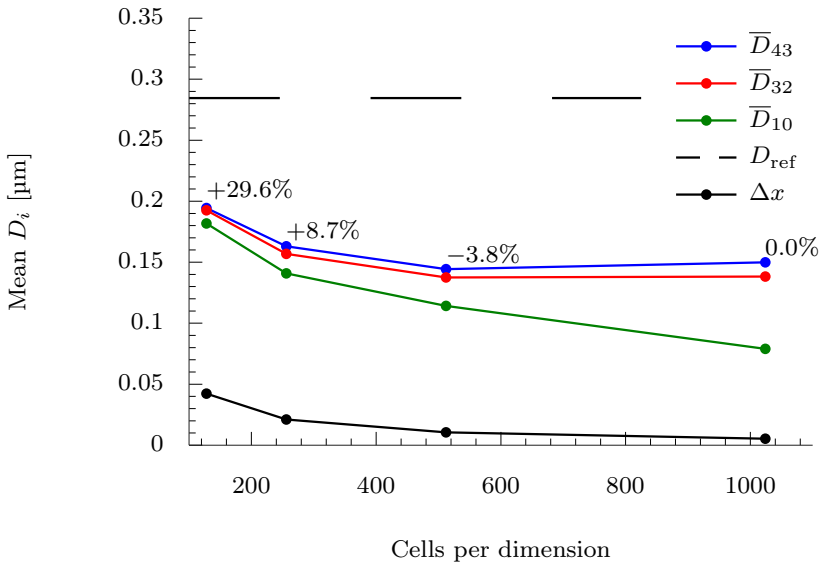

Figure 5.8: Dependency of the $\overline{D}_{10}$ (arithmetic), $\overline{D}_{32}$ (Sauter) and $\overline{D}_{43}$ (De Brouckere) mean diameters with the mesh size, compared with the cell size Δx and estimated droplet size D_{ref}. The error relative to the most refined case is shown for the $\overline{D}_{43}$.

Comparing the mean droplet sizes, it is shown the $\overline{D}_{32}$ and $\overline{D}_{43}$ can vary by up to 30% between the best and worst resolved cases, but the results seem to converge already for the 512^3 cell mesh. This case resolves D_{ref} by 25 cells and R_f by 57 cells. However, due to the computational cost considerations, this level of resolution cannot be employed for cases including a larger number of bubbles and with a

sufficiently large buffer volume to observe the complete spray breakup (that extends far beyond the lamella retraction phase). For the resolution criteria used in this work — $\Delta x < D_{\text{ref}}/15$ and $\Delta x < R_f/30$ – a less than 10% error in the $\overline{D}_V$ and $\overline{D}_A$ is expected due to the contribution of artificial droplets, based on the results of Fig. 5.8. For the arithmetic mean diameter, $\overline{D}_{10}$, the result seems to be a near-linear function of the cell resolution up to the 1024^3 -cell mesh (where $\Delta x < D_{\text{ref}}/50$), meaning that the expected error in $\overline{D}_N$ cannot be quantified and the result is generally non-significant.

Figure 5.8 also shows that the reference droplet size D_{ref} is able to match the droplet size in order of magnitude. However, it seems to overestimate the results for this particular droplet formation mechanism. This can be explained by 1) the exclusion of larger ligaments and deformed droplets and 2) the particular breakup mechanism at the retracting rim, where the local fluid velocity is significantly higher than the bubble growth rate $\dot{R}$ used as a reference (cf. Loureiro et al. [2]).

It should be re-emphasized that this study reflects only the contribution of droplets formed during lamellae retraction, that is the most sensitive to artificial numerical effects. This is still only the first stage of the breakup process in the high We_b regime, that is followed by the chaotic breakup of the matrix of interstitial liquid, generating much larger droplets. Overall, the error introduced in the results for the complete breakup (as seen in Fig. 5.3(c) $t^* = 5.7$) is expected to be much smaller. The reasoning and observations offered here can also be generalized for the lower We_b regimes. The formation of artificial droplets is always expected upon topology changes, which includes the pinching of ligaments in cases such as A-10 (Fig. 5.3(b)). Here it is important to distinguish the organic formation of satellite droplets from long ligaments, versus the much smaller artificial ones possibly formed at the point of pinching. Due to the much larger volume discrepancy relative to the primary droplets, these shall also not impact area or mass weighted statistics. In these cases, the extremely small artificial satellites also tend to quickly evaporate and can thus simply be treated as vapour.

5.3 Quantitative results in randomized clusters

For the results presented in the previous sections there was a deliberate choice to use the regular cubic lattice arrangements to allow a systematic study and better understanding of the breakup mechanics. This arrangement is, however, far from representing realistic conditions and does not yet take full advantage of the capabili-

ties provided by the three-dimensional DNS approach. It was also observed that the high degree of symmetry and regularity can introduce artificial bias on the breakup mechanics as well as exaggerate mesh-dependent effects.

The results presented now, make use of the randomized domain setup introduced in Sec. 4.2.1, representing a large number of bubbles nucleating inside an arbitrarily large primary liquid drop, detached from the liquid bulk. The use of vapour buffer zones instead of continuous liquid, promotes the formation of additional droplets at the outer interface of the primary liquid sphere. This simulation setup thus combines the *bubble coalescence* and the *micro-explosion* assumptions suggested by previous works (Sec. 2.2). The breakup mechanics, that can be directly observed in both the interior and outer shell of the droplet, are nonetheless expected to follow the previously observed breakup patterns. A wider series of tests cases is simulated across the different breakup regimes and superheat conditions, including lower temperatures and higher pressures, even though they fall within the same ranges of We_b and Oh_b previously explored. The complete list of setup parameters is provided by Tab. D2 in the appendix. The number of nuclei (N_{bub}) varies from 1000 to 125 taking into account the type of breakup expected, the maximum expected flow velocity (respecting the incompressible flow assumption) as well as resolution requirements and computational cost considerations. Rather than a fixed spacing between bubble nuclei, the randomized setup implies an average spacing that can be calculated by mass conservation for the target breakup bubble size R_f, as detailed in Section 4.2.1. Thus, bubble coalescence no longer occurs at the exact size R_f, which should instead be interpreted as an average value of final bubble size. Still, the target $R_f^* = R_f/R_{\mathrm{crit}}$ is used as the free parameter that determines the growth rate and other thermodynamic properties (global and constant) according to the RP-e reference model, as detailed in Sec. 4.2.

Although the primary goal of this series of test cases is the extraction of quantitative data, such as droplet size statistics, the results will first be compared in terms of qualitative behaviour across the We_b and Oh_b range. Figure 5.9 provides the breakup sequences for selected cases, showing the initial conditions, different stages of the breakup process and the final spray. For the final step, a histogram of the droplet size is provided, corresponding to the area-weighted droplet size distribution.

The impact of the *retracting liquid* regime for $\mathrm{We}_b < 2$ is now especially evident in Fig. 5.9(a) for Case A-2. There, 1000 bubbles coalesce very early in their growth and surface tension acts to collect the liquid of several interstices into relatively large droplets, as hypothesized earlier with regular bubble arrays. The average droplet

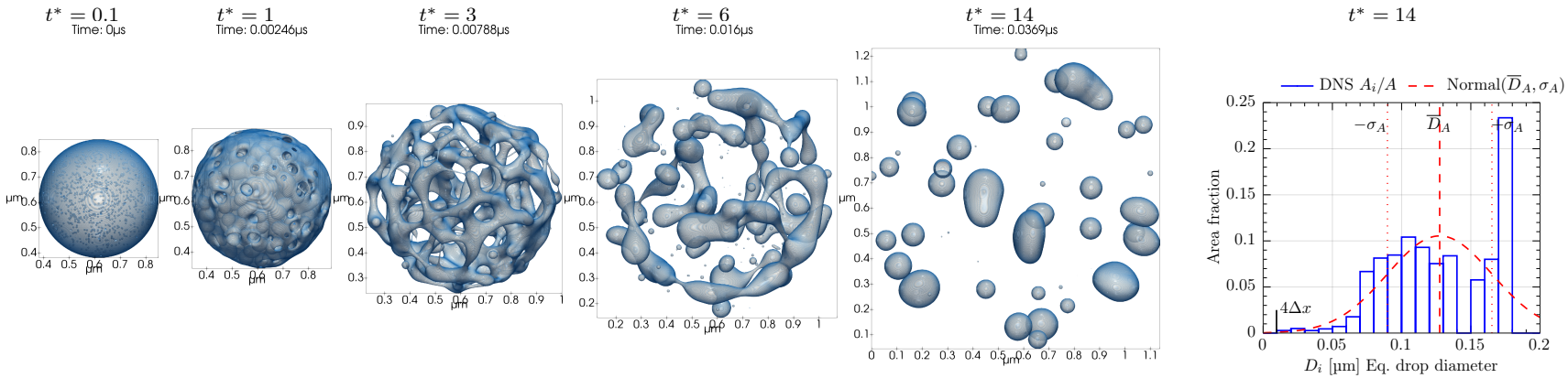

(a) Case A-2: $N_{\text{bub}} = 1000$ $V_0 = 0.055\,\mu\text{m}^3$ $R_f^* = 2$ $T_\infty = 120\,\text{K}$, $p_\infty = 10^3\,\text{Pa}$ $\text{We}_b = 0.54$ $\text{Oh}_b = 0.17$

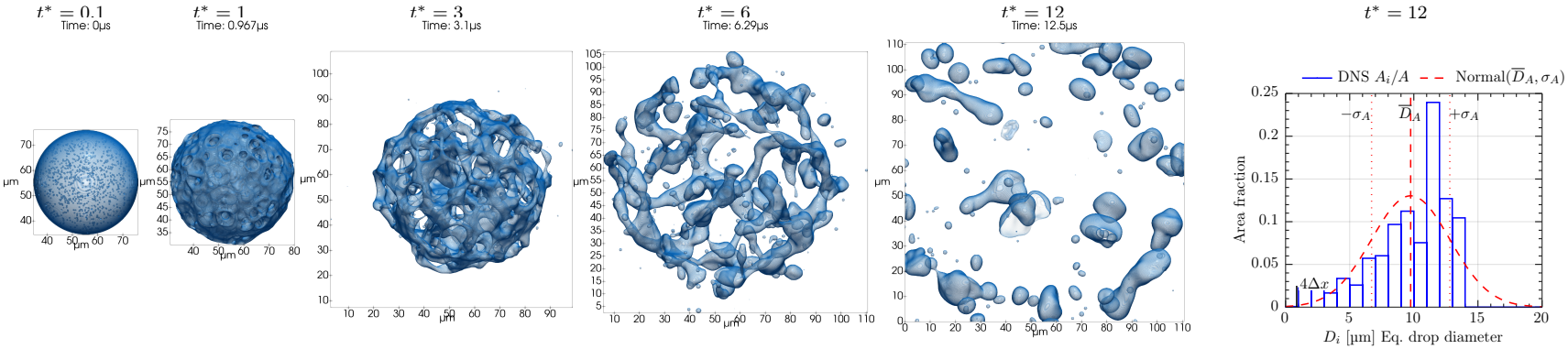

(b) Case C-2: $N_{\text{bub}} = 1000$ $V_0 = 3.85 \times 10^4\,\mu\text{m}^3$ $R_f^* = 2$ $T_\infty = 80\,\text{K}$, $p_\infty = 10^3\,\text{Pa}$ $\text{We}_b = 1.3$ $\text{Oh}_b = 0.029$

Figure 5.9: Breakup sequences for randomized cluster cases at similar points of normalized time t^* and histograms for final area-weighted droplet size distribution, with fitted normal distribution for mean diameter $\overline{D}_A$ (SMD) and standard deviation σ_A. (cont. 1/3)

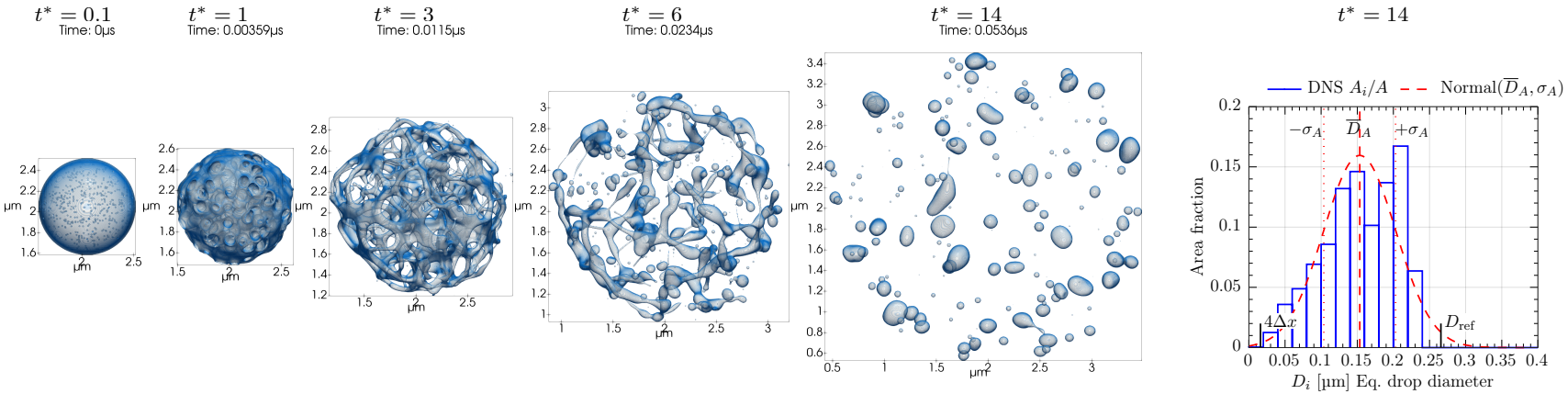

(c) Case A-5: $N_{\text{bub}} = 512$ $V_0 = 0.437\,\mu\text{m}^3$ $R_f^* = 5$ $T_\infty = 120\,\text{K}$, $p_\infty = 10^3\,\text{Pa}$ $\text{We}_b = 3.6$ $\text{Oh}_b = 0.1$

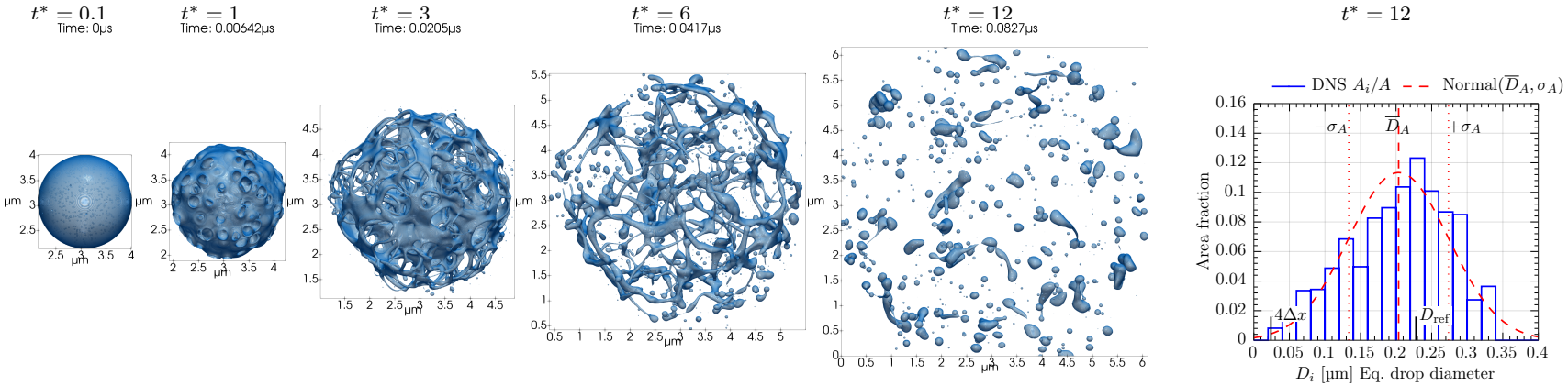

(d) Case A-10: $N_{\text{bub}} = 512$ $V_0 = 3.48\,\mu\text{m}^3$ $R_f^* = 10$ $T_\infty = 120\,\text{K}$, $p_\infty = 10^3\,\text{Pa}$ $\text{We}_b = 8.4$ $\text{Oh}_b = 0.071$

Figure 5.9: (cont. 2/3)

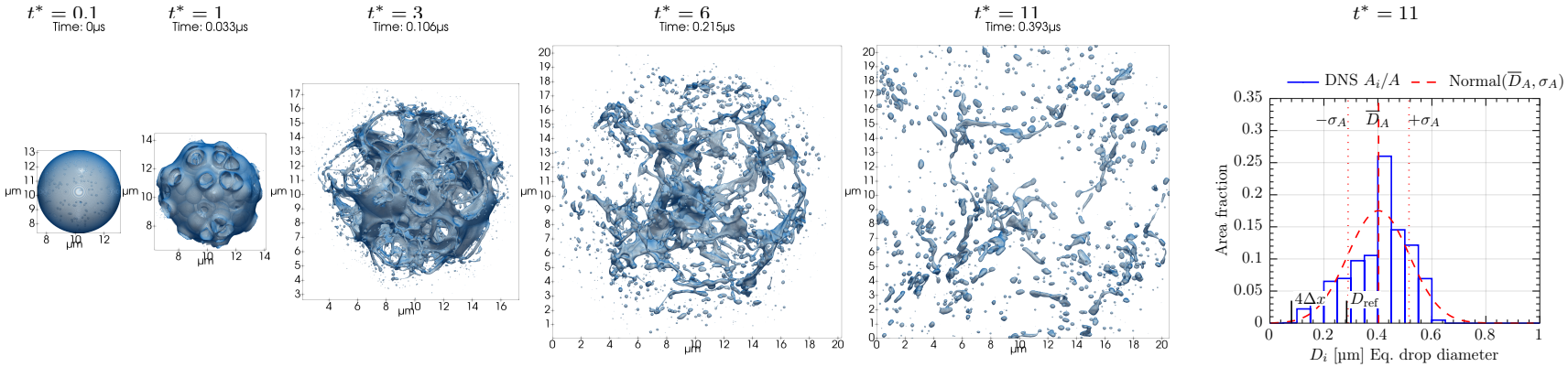

(e) Case A-50: $N_{\text{bub}} = 125$ $V_0 = 105\,\mu\text{m}^3$ $R_f^* = 50$ $T_\infty = 120\,\text{K}$, $p_\infty = 10^3\,\text{Pa}$ $\text{We}_b = 34$ $\text{Oh}_b = 0.029$

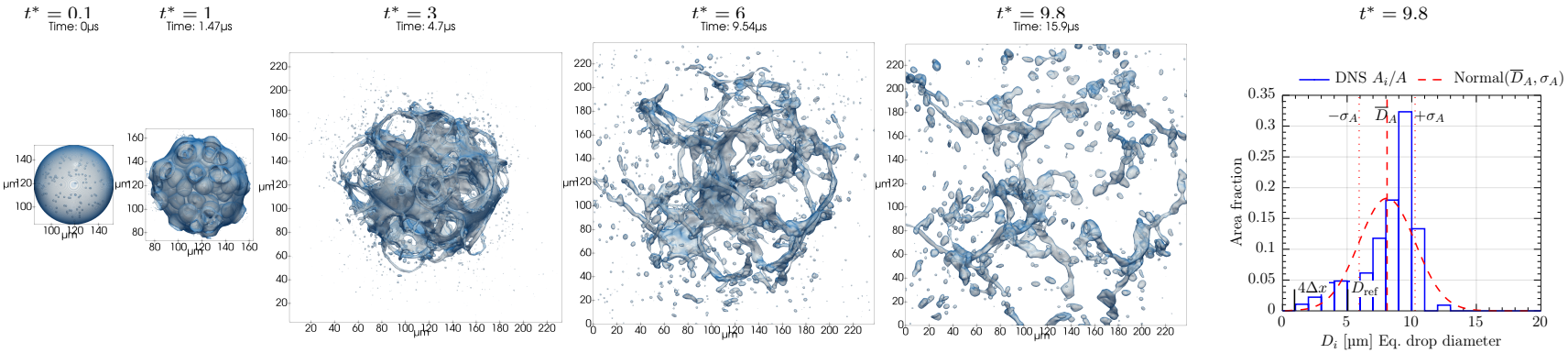

(f) Case D-50: $N_{\text{bub}} = 125$ $V_0 = 1.62 \times 10^5\,\mu\text{m}^3$ $R_f^* = 50$ $T_\infty = 100\,\text{K}$, $p_\infty = 10^5\,\text{Pa}$ $\text{We}_b = 22$ $\text{Oh}_b = 0.011$

Figure 5.9: (cont. 3/3)

size $\overline{D}_A = 0.128\,\mu m$ is approximately 2.5 times larger than the target bubble size $R_f = 0.024\,\mu m$. The same was observed for lower temperature and higher pressure cases, such as case C-2 ($R_f = 2.16\,\mu m$, $\overline{D}_A = 9.76\,\mu m$), shown in Fig. 5.9(b). There, as previously observed, the reduced Oh_b number leads to more irregular droplets and the formation of additional satellites.

Case A-5, in Fig. 5.9(c), is in the *ligament stretching* regime ($2 < We_b < 20$) showing main droplets forming at the bubble interstices connected by thin ligaments. Case A-10, in Fig. 5.9(d), is in the same regime but with larger We_b that allows thinner and longer ligaments that turn into satellite droplets. As expected, for both cases the droplet size is similar (within 20%) to the bubble diameter (for A-5 $R_f = 0.0601\,\mu m$, $\overline{D}_A = 0.153\,\mu m$; for A-10 $R_f = 0.12\,\mu m$, $\overline{D}_A = 0.204\,\mu m$). Contrary to the expectations set by previous works for the *micro-explosion* breakup mechanics [8, 39, 40], the droplets generated at the edge of the primary liquid blob do not show a particularly different mechanism of formation, when compared to the bulk or the cubic lattice cases..

The *thin lamella* regime for $We_b > 20$ is represented by case A-50, in Fig. 5.9(e), and case D-50 Fig. 5.9(f), with the first having the highest We_b and the latter having the lowest Oh_b simulated. Despite the scaling factor of ten between the two, the breakup mechanics are very similar (note that the same randomization seed is used for nuclei placement). Both lead to the formation of thin lamellae in the initial stages of the breakup that burst forming an initial group of small droplets as observed in the previous sections. The breakup continues as the remaining interstitial liquid structures deform in a chaotic fashion. Once again, the initial lamellae breakup ($t^* = 1$–3) can generate a large number of small droplets including those that are well resolved and seemingly originating from natural instabilities during lamellae retraction, as well those that are numerically artificial (barely observable) which are ignored in post-processing if their diameter is less than 4 mesh cells. Compared with the observations of Secs. 5.1 and 5.2.1, the randomized arrangement seems to promote non-simultaneous lamellae puncturing and a wider range of droplet sizes. Lamellae now forming non-othogonally to the mesh, show the expected mechanics of Taylor-Culick type film retraction, with a rim that is less prone to shedding (e.g. Fig. 5.9(e) $t^* = 3$). In the second stage of breakup ($t^* \geq 6$) the droplets generated are much larger, with many ligaments persisting with elongated shapes.

The histograms and normal distributions fitted to each case in Fig. 5.9 are based on mean droplet size $\overline{D}_A$ and respective variance σ_V^2, defined in Appendix Sec. C3. The droplet size estimator D_{ref} and the limit of resolution $4\Delta x$ are also noted when

within the range of droplet sizes shown. Even though the surface area distribution and SMD are the main focus of this analysis, the complete set of statistical results as defined in Eqs. (C12) to (C17) is provided in table 5.1.

Table 5.1: Table of results for statistical data processed at the end of each simulation (instant given by t and t^*).

DNS case	A-2	A-5	A-10	A-16	A-50	B-2	B-10	C-2	C-5	D-2	D-10	D-50
We_b [−]	0.54	3.62	8.44	13.38	33.80	0.93	12.56	1.31	7.38	0.75	8.19	22.08
Oh_b [−]	0.17	0.10	0.07	0.05	0.03	0.08	0.03	0.03	0.02	0.06	0.03	0.01
D_{ref} [µm]	0.7059	0.2658	0.2279	0.23	0.2845	2.907	1.081	26.33	11.72	5.95	2.723	5.051
t^* [−]	13.6	13.52	12.25	13.56	10.81	13.6	10.09	11.72	10.63	13.6	11.98	9.821
t [µs]	0.0372	0.054 01	0.087 28	0.1515	0.3967	0.437	0.9561	12.58	18.96	1.026	2.958	16.02
N_{d} [#]	42	166	450	166	872	115	856	107	660	81	420	454
$\overline{D}_N$ [µm]	0.088 29	0.089 14	0.1084	0.1341	0.2593	0.3369	0.6285	4.701	5.229	0.6923	1.351	3.895
σ_N [µm]	0.0451	0.055 81	0.069 28	0.090 59	0.1168	0.292	0.357	3.601	3.144	0.5968	0.9024	2.2
$\overline{D}_A$ [µm]	0.1275	0.1534	0.2036	0.2694	0.4025	0.7807	1.261	9.755	11.3	1.568	2.743	8.094
σ_A [µm]	0.037 73	0.049 68	0.070 14	0.081 34	0.1129	0.2479	0.372	3.049	3.814	0.5143	0.9303	2.163
$\overline{D}_V$ [µm]	0.1387	0.1695	0.2277	0.294	0.4342	0.8594	1.371	10.71	12.59	1.737	3.058	8.672
σ_V [µm]	0.034 77	0.042 22	0.060 66	0.064 23	0.098 92	0.2042	0.2996	2.385	3.123	0.4264	0.7923	1.711

Estimations for droplet and particle sizes are often provided in the literature by log-normal distributions (of the droplet size probability) and Rosin-Rammler distributions (based on the cumulative mass distribution). These can also be computed based on the DNS data (cf. Loureiro et al. [5]). However, it was found that 1) the log-normal distribution is of little significance given the mesh dependence of the $\overline{D}_N$ results observed in 5.2.1, and 2) the Rosin-Rammler distribution, that is also defined by two simple fitting parameters, does not provide a significant advantage in terms of capturing the skewness of the data, when compared with the (symmetrical) normal distribution for both the $\overline{D}_A$ and $\overline{D}_V$ distributions.

When comparing the $\overline{D}_A$ histograms for each case in Fig. 5.9 with the fitted normal distributions, it can be observed that in most cases the data is skewed towards larger droplets, with an outlying size group. This simply means that the larger droplets contain a larger fraction of the spray surface area. This can be expected as larger droplets allow for more interface deformations, while smaller droplets tend to be smoother and round due to the effect of surface tension and viscosity. This is further proven by a stronger skewness being observed in the cases with lower Oh_b (Fig. 5.9 (b), (e) and (f)). The outlying size group above the mean value seems to be related with the breakup progress over time. For cases A-50 or D-50 a few liquid large structures are still connected but clearly in the process of breaking-up. In cases A-2 and C-2 especially elongated droplets can be observed that, although being few in count, contain a large fraction of the spray area. It was observed that throughout the simulation time, the spray evolves towards the normal

distribution, as the last large structures tend to break and relax to spheroid shapes. This is not the case at the end of the simulations due to computational limitations, as a significant fraction of the liquid would leave the simulation domain. In other words, the outlying size group above the mean can signify that the breakup process is not yet complete. Notwithstanding, and as an important result of this work, the average size, $\overline{D}_A$ or SMD, does not change significantly over time.

The latter conclusion can be better understood in terms of total surface area to liquid volume ratio, γ, given by Eq. (C20), noting that $\overline{D}_A = 6/\gamma$. This is shown in Fig. 5.10 in normalized form given by γ^* (Eq. (C21)), as a function of normalized time t^*. Recalling that $t^* = 1$ corresponds to the instant of bubble coalescence where the average radius R equals R_f, it can be observed that the total surface area ceases to increase soon after the bubbles collide and start coalescing. At this point the internal vapour volume becomes interconnected across many, or all, bubbles and also to the exterior of the liquid blob. This means that the internal gas pressure, that was driving fluid expansion, is now able to escape and no further energy potential is available to create additional surface area. Conversely, it is obvious by by observing

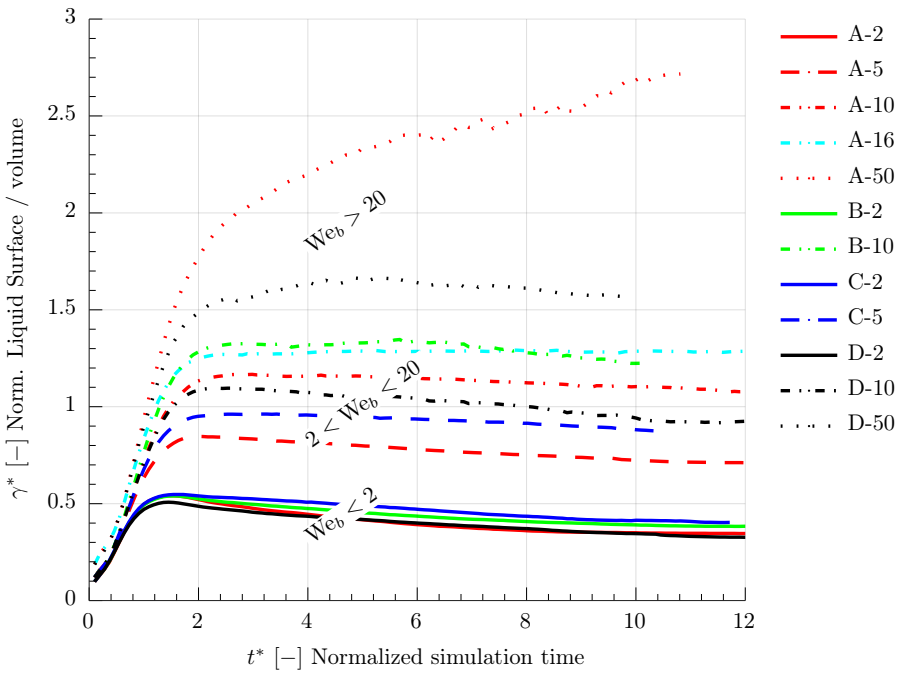

Figure 5.10: Normalized surface to volume ratio of the spray as function of time.

Fig. 5.9 that at $t^* = 2$ the breakup process has barely started and the spray is nothing more than a single drop with a large internal surface area. The actual breakup process is then driven by 1) the inertia or kinetic energy stored in the

liquid that has been accelerated radially and reached a velocity of the order of $\dot{R}$ around each bubble centre; and 2) the surface tension force, where the initial bubble expansion can be interpreted as an increase of elastic potential energy, that is then released through the various mechanisms observed (pinching, retraction, etc.) as the system relaxes to small and stable droplets. The two adversarial effects act concurrently without substantially increasing the total surface area. For the slight variations in γ observed for $t^* > 2$, various factors can be considered, including the effect of liquid viscosity (or lack thereof), continued droplet vaporization that tends to eliminate early-formed small droplets and the loss of significant liquid volume through the domain boundaries. In particular for case A-50, with $\mathrm{Re}_b = 2 \times 10^2$ a departure from laminar flow can be expected and the breakup becomes influenced by chaotic flow in both phases, akin of aerodynamic breakup. This observation and interpretation of the $\gamma(t^*)$ curves is in line with the initial reasoning for the D_{ref} estimator (Eq. (5.5)) as a balance of dynamic pressure associated with $\dot{R}$ and the Laplace pressure acting to form a small droplet.

Figure 5.11 provides a summary of the results for the area weighted mean droplet sizes $\overline{D}_A$ (SMD), as as function of R_f^* and compared with the estimator D_{ref} (dashed lines). The vertical error bars represent the $\overline{D}_A \pm 2\sigma_A$ interval, that represents over 95% of spray area and volume. For comparison the results for droplet size obtained using the cubic lattice arrangement of Sec. 5.1 are also shown (without variance interval).

It is noteworthy that, in-spite of its simplicity, D_{ref} provides an excellent estimation of the $\overline{D}_A$ for cases with $R_f^* \approx 10$ across all thermodynamic conditions (p_∞ and T_∞) simulated, i.e. cases in the *ligament stretching* regime, that also correspond to the point of maximum bubble growth velocity according to the RP-e model. The estimator, however, does not take into consideration the different types of breakup observed, that depend primarily on We_b. The deviation from the reference seems to be consistent for all case sets: sizes lower than estimated for *merging drops* regime with $\mathrm{We}_b < 2$ and larger than estimated for the *thin lamella* regime with $\mathrm{We}_b > 20$. By plotting the $\overline{D}_A/D_{\mathrm{ref}}$ ratio against We_b, as shown in Fig. 5.12 on a logarithmic scale, the deviation from the reference can be fitted by least-squares regression to the log of the data points. A DNS-calibrated model is thus produced as

$$\frac{D_A^{\mathrm{fit}}}{D_{\mathrm{ref}}} = 0.294\,\mathrm{We}_b^{0.526} \qquad \Rightarrow \qquad D_A^{\mathrm{fit}} \approx \frac{10}{3}\sqrt{\frac{\sigma R_f}{\rho_\ell \dot{R}^2}}, \tag{5.7}$$

where the approximated version makes use of Eqs. (5.1) and (5.5). Here $\dot{R}$ and σ are

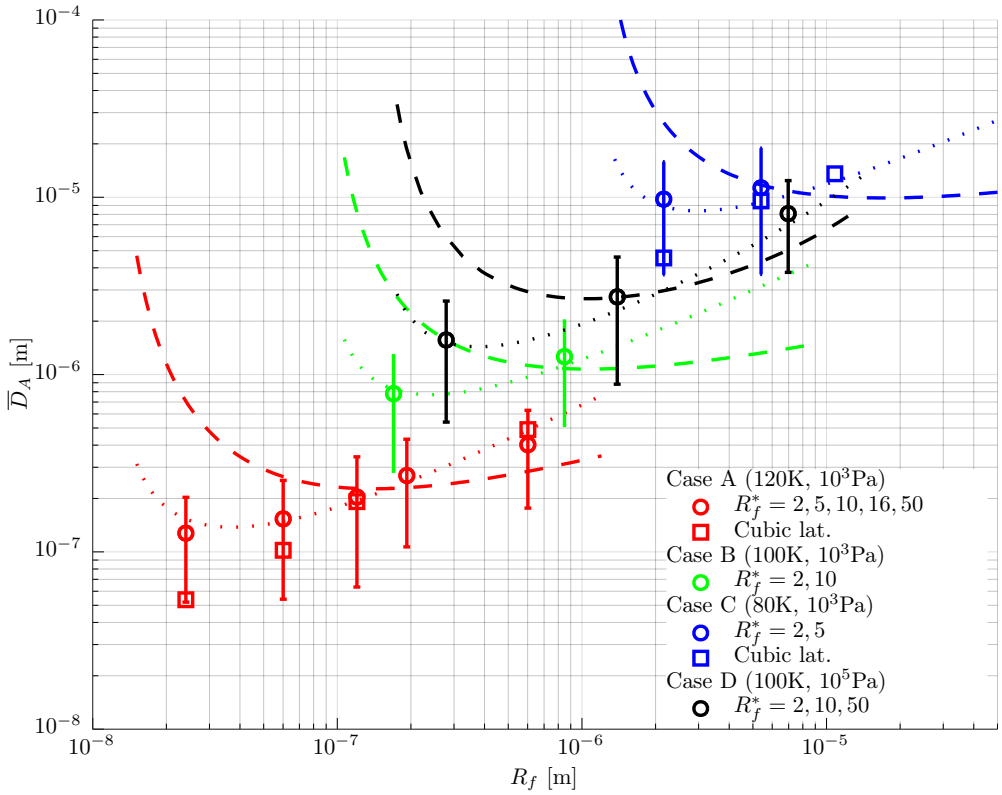

Figure 5.11: Mean droplet sizes obtained by DNS as function of R_f, given by the area-weighted mean diameter, $\overline{D}_A$, (equiv. SMD) compared with the D_{ref} estimator (dashed lines). The error bars represent the area fraction interval given by $\overline{D}_A \pm 2\sigma_A$. The square symbols show results obtained using for cubic lattice setup. The dotted line presents fits given by Eq. (5.7).

the growth rate and surface tension coefficient estimated at the coalescence radius R_f, given in this work (but not necessarily) by RP-e. The fitted curves are included in Fig. 5.11 as dotted lines.

The result provided by Eq. (5.7) may serve as the primary model for the purpose of estimating SMD droplet sizes under certain conditions, particularly relevant for comparison with experimental data. However, it may not immediately serve as a reference to model sub-grid-scale modelling in LES or RANS simulations (e.g. [44, 47]). These typically require a source term for a transported surface area density scalar, i.e. a rate of surface area generation, that can be provided by the time derivative of γ. Having observed in Fig. 5.10 that the total surface area of the spray is determined early on at $t^* < 2$ followed by a plateau, the most relevant result becomes the determination of the peak of surface generation rate, $\dot{\gamma}_{\max} = \max(\dot{\gamma})$, or its normalized value $\dot{\gamma}^*_{\max} = \max(\dot{\gamma})/\dot{\gamma}_{R_f}$. This result, computed for each case along with the corresponding γ and respective reference values used for normalization, are

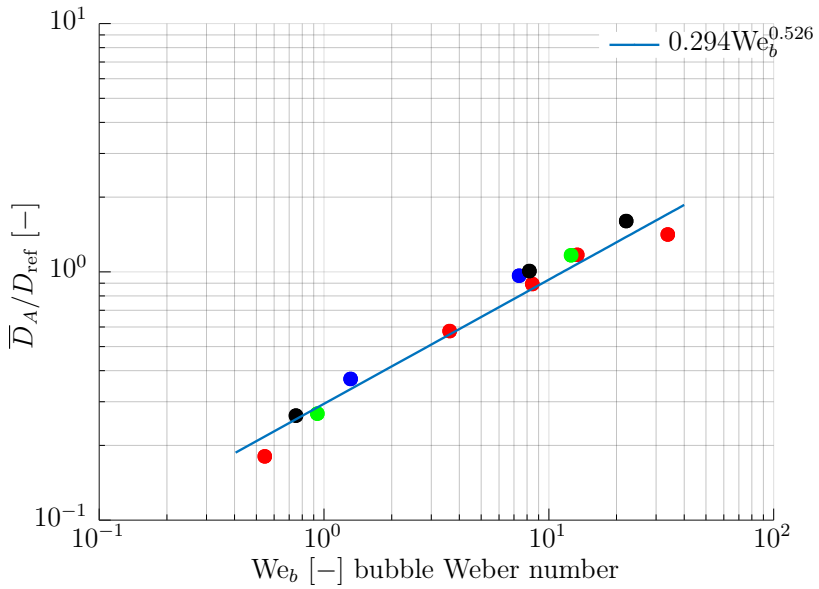

Figure 5.12: Deviation of the SMD relative to the D_{ref} estimator as function of the We_b fitted to an exponential model.

collected in Table 5.2. The peak occurs roughly at $0.5 < t^* < 1$, with deviations for each case depending on the We_b number.

Similarly to the process used to obtain Eq. (5.7), the deviation of the DNS results to the reference given by $\dot{\gamma}_{R_f}$, can be plotted against We_b (Fig. 5.13) and approximated by a least-squares regression to the log of the data points. The peak values $\dot{\gamma}_{\max}$ can thus be given as a DNS-calibrated model by

$$\frac{\dot{\gamma}_{\max}^{\text{fit}}}{\dot{\gamma}_{R_f}} = 0.283\,\text{We}_b^{0.191} \qquad \Rightarrow \qquad \dot{\gamma}_{\max}^{\text{fit}} \approx 1.87\,\text{We}_b^{\frac{1}{5}}\frac{\dot{R}}{R_f^2}, \tag{5.8}$$

where $\dot{\gamma}_{R_f}$ (Eq. (C24)) is derived in Sec. C4 based only on the simulation parameters assuming coalescence at $t^* = 1$ and with $\dot{R}(R_f)$ given by the reference solution RP-e. The approximated form of Eq. (5.8) is obtained with $\dot{\gamma}_{R_f} \approx 6.59\frac{\dot{R}}{R_f^2}$, by assuming high liquid-vapour density ratios and $\eta_f = \pi/6$. The exponents on the equation highlight that $\dot{\gamma}_{\max}$, is primarily determined by $\dot{R}$, as would be expected. The We_b number, that accounts for deviations from the simplified analytical model, represents the amount of interface deformation that can occur until bubble coalescence and the start of the actual breakup process. The relevance of this result and its applicability in SGS modelling for other numerical methods is discussed in the next chapter.

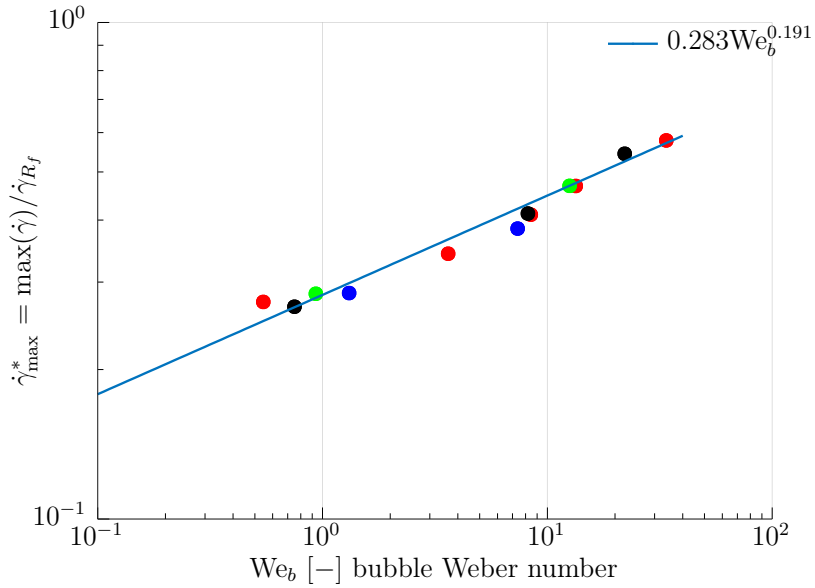

Figure 5.13: Deviation of the maximum surface area generation rate $\dot{\gamma}_{\max}$ relative to the $\dot{\gamma}_{R_f}$ estimator as function of the We_b fitted to an exponential model.

Table 5.2: Table of results for the surface area density and its generation rate, with reference normalization values (at $t^* = 1$) provided by γ_{R_f} and $\dot{\gamma}_{R_f}$. The DNS obtained values γ and $\dot{\gamma}_{\max}$ correspond to the peak of surface area generation, occurring at the instant given by $t(\dot{\gamma}_{\max})$ and $t^*(\dot{\gamma}_{\max})$.

DNS case	A-2	A-5	A-10	A-16	A-50	B-2
We_b [−]	0.54	3.62	8.44	13.38	33.80	0.93
R_f [µm]	0.024 04	0.0601	0.1202	0.1923	0.601	0.1697
γ_{R_f} [m²/m³]	1.372×10^8	5.486×10^7	2.743×10^7	1.715×10^7	5.486×10^6	1.943×10^7
$\dot{\gamma}_{R_f}$ [m²/m³s]	1.062×10^{17}	2.883×10^{16}	8.024×10^{15}	3.185×10^{15}	3.075×10^{14}	1.227×10^{15}
γ [m²/m³]	4.705×10^7	3.91×10^7	2.947×10^7	2.227×10^7	1.491×10^7	7.686×10^6
$\dot{\gamma}_{\max}$ [m²/m³s]	2.908×10^{16}	9.865×10^{15}	3.29×10^{15}	1.492×10^{15}	1.78×10^{14}	3.487×10^{14}
$t(\dot{\gamma}_{\max})$ [s]	1.506×10^{-9}	2.561×10^{-9}	5.848×10^{-9}	8.164×10^{-9}	3.011×10^{-8}	1.769×10^{-8}
$t^*(\dot{\gamma}_{\max})$	0.5507	0.6414	0.8208	0.7306	0.8205	0.5508
DNS case (cont.)	B-10	C-2	C-5	D-2	D-10	D-50
We_b [−]	12.56	1.31	7.38	0.75	8.19	22.08
R_f [µm]	0.8487	2.161	5.404	0.2788	1.394	6.971
γ_{R_f} [m²/m³]	3.885×10^6	1.526×10^6	6.101×10^5	1.183×10^7	2.365×10^6	4.73×10^5
$\dot{\gamma}_{R_f}$ [m²/m³s]	8.289×10^{13}	2.847×10^{12}	6.854×10^{11}	3.181×10^{14}	1.937×10^{13}	5.848×10^{11}
γ [m²/m³]	4.757×10^6	6.151×10^5	5.308×10^5	3.826×10^6	2.187×10^6	7.413×10^5
$\dot{\gamma}_{\max}$ [m²/m³s]	3.885×10^{13}	8.117×10^{11}	2.636×10^{11}	8.512×10^{13}	7.985×10^{12}	3.182×10^{11}
$t(\dot{\gamma}_{\max})$ [s]	8.63×10^{-8}	5.91×10^{-7}	1.303×10^{-6}	3.477×10^{-8}	1.803×10^{-7}	1.337×10^{-6}
$t^*(\dot{\gamma}_{\max})$	0.9107	0.5502	0.7305	0.4611	0.7301	0.82

Chapter 6

Discussion

This chapter provides an overview and discussion of the main results with focus on their relevance and applicability. At this point it worth recalling the specific objectives for this work, enumerated in Sec. 1.2. The first objective referred to the affordability of a methodology to perform DNS of flash atomization. Some key points to be highlighted are the use of a very precise model for bubble growth that allowed the calibration of thermodynamic effects in the DNS, investigation of mesh resolution criteria and the relatively low computational cost (cf. Appendix B) that allowed testing of a wide range of thermodynamic conditions and the collection of statistically representative data. Some trade-offs resulting from the pure fluid-mechanical and incompressible framework adopted are also discussed in this chapter.

The second objective, stated as to explore and provide a qualitative characterization of the primary breakup mechanics, was covered by the results in Sec 5.1 and confirmed by the results of Sec. 5.3. Additional discussion of the applicability of the results will now be covered in Sec 6.1 with particular emphasis on a comparison with previous assumptions made in the background literature covered in Sec. 2.2.

Objective number 3 was the collection of statistical data and other spray characteristics and has been achieved with the results presented in Sec. 5.3. Sec. 6.2 covers how the results collected and proposed fitted to the DNS results can, to a limited extent, be compared with available empirical data. The last objective, referring to the development of SGS models, has also been covered in Sec. 5.3. Section 6.3 discusses at a high level how the DNS calibrated models can be employed as future sub-grid models in large scale simulations of the flow. Finally, in Sec. 6.4 some limitations of the methodology used are discussed, leading to suggestions for future improvements to the method at technical level.

6.1 Breakup mechanics

A series of droplet formation mechanisms has been identified and correlated to a range of We_b and Oh_b numbers. These are defined relative to the microscopic bubbles within the flashing jet, rather than the conventional approach of relating them to the macroscopic jet, or injection conditions. While droplet formation is a widely studied subject in industry and academia [82, 83, 32, 84, 85, 52], this is the first time that such classification has been performed for flash boiling atomization in the form of numerical experiments. The mechanics observed can be directly compared to previously hypothesised models reviewed in Sec. 2.2, particularly the *bubble coalescence* in a densely packed matrix and the *micro-explosion* hypothesis.

The mechanics observed for the intermediate $2 < We_b < 20$ range seem to agree with the hypothesis of Sher and Elata [7] and Senda et al. [38], that the main droplet size is primarily related with the void fraction, or interstitial liquid between equal bubbles in a closely packed bubble arrangement. This implies the droplet number and size is thus directly determined by the number and size of the bubbles. It has been demonstrated here, however, that this does not hold true outside this range of We_b. Within the range, the DNS notably shows that the resulting droplet is similar when the bubbles are regularly or randomly distributed, given that the volume of liquid per bubble nuclei is the same at initialisation. The main distinctions between the present study and the assumptions in the cited works are 1) the breakup is driven by bubble growth according to the Rayleigh-Plesset mechanics instead of global energy conservation considerations, and 2) the type of bubble close-packing arrangement assumed at the instant of coalescence. The first affects only the correlation between the thermodynamic variables (T_∞ and p_∞ or level of superheat) and We_b and Oh_b that ultimately determine the expected breakup behavior or droplet size. The second has implications on the detail of the breakup mechanics.

Sher and Elata [7] and Senda et al. [38] assume the densest packing arrangement of $\eta_f = \pi/3\sqrt{2} = 0.74$, while the cubic lattice array assumption used in this work corresponds to the least dense packing factor $\eta_f = \pi/6 = 0.52$. Besides the trivial 30% difference in the available interstitial volume to form each droplet, it is important to note that the densest packing assumption would effectively suppress the presence of inter-droplet ligaments. These play an important role in the re-coalescence of multiple drops in the $We_b < 2$ regime (see Fig. 5.3(a) $t^* = 1.5$), as well as being responsible for the formation of satellite droplets in the $10 < We_b < 20$ region (Fig. 5.3(b) $t^* = 3.2$). Both effects are thus neglected in the original theoretical

models. Furthermore, a natural random packing of equal spheres would correspond to an intermediate η_f that cannot be explicitly estimated. However, it can be argued that the least dense extreme is a better approximation, since there is no particular physical mechanism to promote a re-arrangement of the bubbles towards a denser packing, such as the case of a solid atomic structure. Instead, at least for the lower We_b regimes, the bubbles tend to coalesce and initiate the breakup process upon first contact with the nearest neighbour. Further discussion on the choice η_f and a possible alternative approach can be found in Loureiro et al. [5]. This issue is however somewhat artificial, since it arises from the basic assumption that all bubbles in the control volume nucleate simultaneously and later coalesce with equal sizes. This assumption is made in the theoretical models, as well as the present work, out of necessity to reduce the number of free variables. Such assumption is fundamentally not necessary for more detailed DNS studies, as will be further discussed.

Alternative approaches to model the primary breakup mechanics proposed by Razzaghi [8], Zeng and Lee [39] and Price et al. [40], that can be classified as the *micro-explosion* hypothesis, are based on the assumption of a single bubble nucleating within an existing droplet, with droplets resulting from Rayleigh-Taylor instability in the spherical liquid film surrounding the growing bubble. The DNS shows that such conditions are virtually impossible, except for the particular case that a single nuclei is perfectly positioned in the centre of a spherical primary drop. Any deviation from this condition would cause the bubble to puncture through the liquid film at a localized (thinnest) point followed by either A) the complete retraction of the liquid into a new stable droplet shape at low We_b numbers, or B) the formation and bursting of a thin lamella at high We_b numbers. Although not documented in the present work, preliminary DNS test cases with only a few bubble nuclei in the low We_b regime clearly support condition A), showing that the trapped vapour can quickly escape the primary liquid blob, resulting in a single drop of size similar to the initial control volume. For this reason, tests in the low We_b regime were ultimately performed with up to 1000 nuclei, still resulting in a relatively small number of droplets. Condition B) can be generally observed in high We_b cases such as A-50, even though they are initialized with a relatively large number of nuclei.

Although it can be argued that the instability of the thin lamellae could be modeled according to classical Taylor instability models first proposed by Razzaghi [8], it is evident in the DNS that these droplets represent only a very small fraction of the spray mass. Furthermore, the DNS shows that the lamellae also tend to burst at localized points, rather than from uniformly growing instabilities with a specific

wavelength. The subsequent droplet ejection seems to be regulated by Taylor-Culick mechanics [80, 81]. It is, however, not possible to use this theory as a basis for prediction of the secondary droplet size in the present context, since the Taylor-Culick velocity depends on the film thickness. The later is related with the limit of mesh resolution in the DNS, unless the initial puncturing is artificially triggered.

The thin-lamellae type of breakup is notably one of the few instances of direct empirical observation of breakup in flashing conditions, observed in detail by Alghamdi et al. [24]. Their setup employing very small nozzles of the order of 100 µm and very high injection pressures promotes external flashing and allows the observation of individual bubbles bursting within the jet. The observations are very much in line with the mechanics observed in the DNS for cases such A-50 and D-50 (cf. Fig. 5.9) in the early stages of breakup. This, however, does not exclude the possibility of other breakup mechanics in fully flashing conditions promoted by different experimental setups and injection parameters [19, 26, 23, 27], particularly for larger aperture injector nozzles.

Generally, it is important to consider that a particular reference model for 1D bubble growth in superheat liquid (RP-e) has been used as a reference to both determining the reference We_b and Oh_b dimensionless numbers, as well as to accounting for key thermodynamic parameters in an otherwise pure fluid-mechanical DNS framework. Still, the classification of breakup patterns in terms of We_b and Oh_b provides a precise tool to predict the type of breakup expected that is independent of the exact reference model used. I.e., if the key variables $\dot{R}$ and R_f are known for a given level of superheat by any means of estimation, in addition to the fluid properties (ρ_ℓ, σ and μ_ℓ), then the breakup patterns observed are expected to maintain the correlation with the dimensionless numbers defined. Furthermore, these findings can be generalized to cover the flashing breakup behaviour of other fluids, e.g. by computing their respective RP-e reference solutions or using a suitable alternative model. Solutions of the RP-e and resulting We_b and Oh_b curves have been computed for relevant cryogenic propellants in addition to LOx, namely N_2, CH_4 and H_2, as well as water. They are provided for reference in Appendix E.

6.2 Droplet size

The second major contribution of this work is the provision of a predictive approach to estimate droplet sizes resulting from the primary breakup for a given bubble number density. The method is predictive in the sense that it does not require

empirical calibration. Instead, the foundation is the reference solution for bubble growth, RP-e, which is in turn based on well established ab-initio models.

The D_{ref} estimator (Eq. (5.5)) provides a preliminary order of magnitude estimation for the average droplet size (SMD), based on the expected instantaneous bubble size and growth rate at the point of coalescence. The statistical analysis of the DNS results shows a general agreement with the D_{ref} prediction, but local deviations are observed that can be correlated with the different breakup regimes controlled by the We_b number. The same applies to the proposed estimator for the surface area generation rate $\dot{\gamma}_{\max}$. These deviations, which include the contribution of bubble non-sphericity, secondary satellite droplets, lamellae bursting and transition to aerodynamic breakup, can be consistently accounted for via the DNS-fitted models given by Eqs. (5.7) and (5.8) that specify a given We_b dependence.

Since both the D_{ref}, $\dot{\gamma}_{R_f}$ estimators and We_b are associated with the fluid properties and growth rate via the RP-e solution for bubble growth, these results can also be generalized for other fluids and injection conditions, provided that they fall within the range of We_b and Oh_b numbers covered by the DNS. However, bubble number density, n, (that defines R_f^* and corresponding $\dot{R}$) remains a free, unknown variable. Still, the dependence of D_{ref} with the free parameter R_f^* reveals a minimum that is associated with the peak value of bubble growth rate for a given level of superheat. This means that even if the bubble number density cannot be reliably estimated or varies drastically within the macroscopic flow, an absolute minimum droplet size can be estimated for a given fluid temperature.

The results obtained here can be compared with various experimental studies [29, 30, 25, 27] where droplet size statistics are obtained via phase Doppler anemometry (PDA). In spite of a wide variety of fluids being employed, these works generally find droplet SMD of the order of 10-30 µm in fully flashing conditions, or larger for partially flashing flows. This range of droplet sizes may at first seem in stark contrast with the range of droplet sizes obtained via DNS, that range from 0.1 µm to 10 µm. It is important to note, however, that the DNS simulations have primarily focused on cases of extreme superheat (cf. table 3.1) with the assumption of high bubble number density (small R_f^*), as these tend to be computationally more affordable and provide the most interesting breakup mechanics. Besides the particular focus on LOx as the working fluid, for which no experimental data is available, such conditions are generally beyond the range of superheat levels tested experimentally.

Rees et al. [27] provides the only known empirical data for SMD in cryogenic fluids, specifically LN2, as a surrogate for LOx and other cryogenic rocket propellants.

In Fig. 6.1 these results are compared with the simple D_{ref} (Eq. (5.5)) estimator as well as the proposed model calibrated to the DNS data D_A^{fit} (Eq. (5.7)) obtained using the RP-e model applied to LN2. The experimental data range can be compared

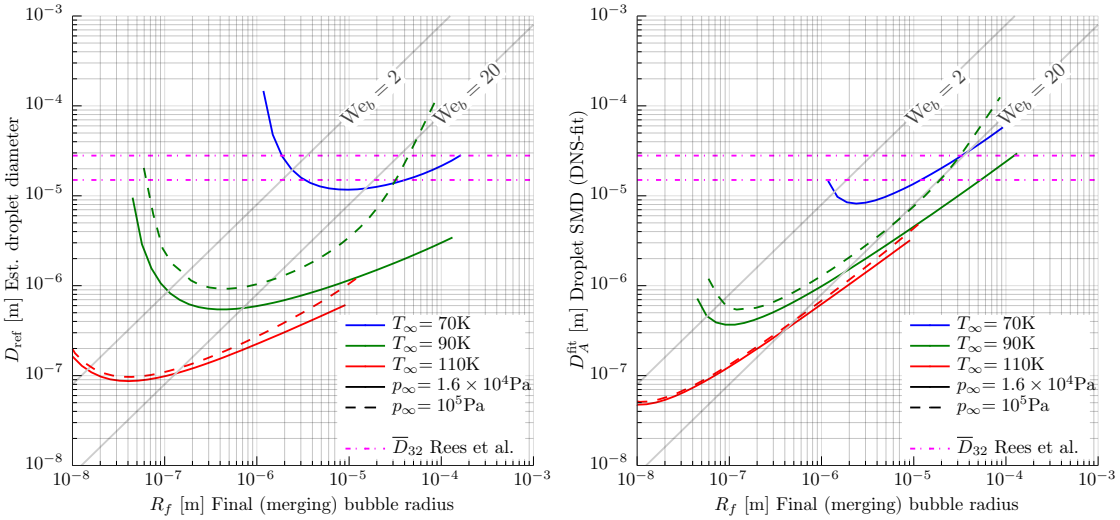

Figure 6.1: D_{ref} estimator (left) and DNS fitted model D_A^{fit} (right) as function of R_f for LN2 at T_∞ indicated by line colour and p_∞ by line type. Compared is the range of $\overline{D}_{32}$ measured at different spray locations by Rees et al. [27] (LN2 at $p_{\text{chamber}} = 7300\,\text{Pa}$, $T_0 = 89.9\,\text{K}$)

firstly to the closest solution obtained for $T_\infty = 90\,\text{K}$ $p_\infty = 1.58\,\text{Pa}$ (green solid line) that is just above the triple point pressure of N_2 ($1.25 \times 10^4\,\text{Pa}$). While the D_{ref} estimator makes a poor prediction of the droplet sizes measured, the D_A^{fit} model based on DNS results seems to intersect the empirical data range in the high We_b region. This implies bubbles coalescing at sizes that are of the order of 1000 times larger than the critical radius, or relatively low nuclei number densities. Although it can be inferred that the type of breakup would correspond to the thin lamella regime, it is important to note that this point extrapolates beyond the range of the DNS test cases. In fact, with We_b of the order of 100 and Re_b of the order 1000, it is expected that the mechanics of bubble coalescence would have minimal influence on the droplet size, with the breakup being mainly aerodynamically driven in a turbulent flow.

Recalling that the T_∞ and p_∞ parameters of the DNS are only local variables within the context of the large scale flow, it is also worth comparing the experimental data with the high pressure case at the same temperature (green dashed line) and the low temperature case at low pressure (solid blue). Both intersect the experimental data range at points corresponding to smaller bubble radii and $\text{We}_b \leq 20$, where the

breakup mechanics have been covered by DNS. These two cases are referred here as limit examples, as the exact pressure and temperature distributions within the large scale flow are generally not known.

Actually, it can be argued that the level of superheat associated with a given experimental condition, is never "felt" in the regions within the jet or spray plume where the atomization process is taking place. Pressures higher than p_{chamber} can be expected closer to the nozzle exit as the sonic two phase flow relaxes towards the vacuum through a system of shocks [19, 23, 16]. Furthermore, within a large section of the jet containing a large number of bubble nuclei, it has been shown by Dietzel et al. [60] that pressure waves induced by bubble expansion lead to a pressure gradient towards the jet core or centre of the primary liquid blob, where the effective level of superheat is significantly reduced. Finally, a reduction in bulk liquid temperature is expected in the downstream spray direction due to the evaporative cooling effect. These effects may affect not only the bubble growth rates according to the RP-e model but also reduce the nucleation rate leading to a larger coalescence radius R_f.

Also shown in Fig. 6.1 as well as in Fig. 5.5 is a relative insensitivity to pressure for the higher temperature cases (red lines). These predict droplet sizes 2 orders of magnitude smaller than the ones measured experimentally, across a wide range of fluids. Such small droplets, if present, are likely to completely evaporate within a time frame that is too short to be captured empirically and would be generally treated as vapour. As the temperature increases further and the critical limit is reached, no phase distinction would exist.

In addition to the figures previously shown, Appendix E compiles an evaluation of D_A^{fit} and $\dot{\gamma}_{\text{max}}^{\text{fit}}$ models for O_2, N_2, CH_4 and H_2. The general behaviour of the D_A^{fit} model as function of R_f does not vary across the range of cryogenic fluids. At the highest levels of superheat evaluated, the minimum of the D_A^{fit} curve generally corresponds to values in the vicinity of 0.5 to 0.1 µm. Towards lower temperatures, the expected droplet sizes are in the region of 1–10 µm. Notably it can be interpolated that for N_2 at 80 K it should be expected to generate droplets that are significantly smaller than O_2 at the same temperature. This could have implications when using LN2 as a surrogate for LOx in engineering tests. The relative sensitivity of the droplet size with temperature can vary substantially depending on the fluid. Hydrogen, which has a narrow 18 K band of temperatures between critical and triple point, shows an order of magnitude change in D_{ref} for a 5 K variation of T_∞. This contrasts with CH_4, for which a 5× variation of D_{ref} can be expected across a 30 K

temperature variation. For O_2 and N_2, the variation is approx. one order of magnitude per 20 K. At higher pressures (low superheats), just like O_2, CH_4 and N_2 can show a significant increase of the droplet size for large R_f^* values, corresponding to the beginning of thermal effects that slow the bubble growth.

6.3 Towards SGS Modeling

For the reasons stated in Sec. 6.2, it is generally not appropriate to directly compare the estimates based on RP-e or the DNS results with experimental data for a given level of superheat associated with the global injection conditions. Instead, the present results are especially well suited to act as sub-grid scale (SGS) models in large-scale CFD of the macroscopic flow (reviewed in Sec. 2.3.1), where local temperature and pressure are readily available as implicit field variables. For most of the cases tested, the DNS domain size and simulation time are of the order of typical grid cell size and time step, respectively.

Both DNS-calibrated models proposed, D_A^{fit} (Eq. (5.7)) and $\dot{\gamma}_{\max}$ (Eq. (5.8)), are suitable for SGS implementation. Furthermore, comprehensive statistical data – in the form of weighted means and standard variance for the number-probability, surface area and volume distribution – have been provided in table 5.1, from which more detailed DNS-fitted models can, in principle, be derived. To calculate a local We_b (Eq. (5.1)) and evaluate these models, RP-e or an equivalent analytical model would be used to estimate the bubble growth rate $\dot{R}$. Additionally, it is necessary to provide an estimate for the bubble number density n or R_f (interchangeable via Eq. (4.18)). This must be determined based on a transported nuclei number density, surface area density or calculated locally according to a nucleation rate model (e.g. Eq. (3.11)) as function of the local p and T, such that a closed system of equations for SGS modelling can be established. Although the DNS being parameterised based on an average spacing of bubble nuclei is an undesired feature, this approximation is generally compatible with SGS modelling and implies no loss of information. This is because, in the context of LES or RANS methods, the relevant input variables also represent average values within the computational cell.

The model related with surface area generation, $\dot{\gamma}_{\max}$ (Eq. (5.8)), is particularly well suited for ELSA/Σ-Y type of frameworks [49, 44, 45, 47], where it may be used as a reference for a surface area density source term ($\dot{\Sigma}$). It is worth recalling that $\dot{\gamma}_{\max}$ is associated with the *rate* of surface area generation, that peaks during the initial bubble growth, while D_A^{fit} corresponds to the *final* spray SMD, that in turn is

equivalent to the ratio of surface area to volume (Σ). Thus, both results can be used independently or in conjunction as necessary for a given SGS modelling approach. In this context, it is also worth to highlight that the results obtained in this work rely on independent evaluations of each droplet's surface area and volume as detailed in Appendix C. This is only achievable via interface-capturing DNS, while empirical PDA-based methods rely on the assumption of droplet sphericity.

Finally, it should be noted that the proposed models are representative of only the initial stages of flash boiling atomization, where the liquid breakup is driven by bubble growth and the bubble surface tension plays a significant role. In areas where the nucleation rate is reduced, the breakup is expected to become dominated by common aerodynamic/turbulent processes. SGS models should thus transition to an adequate secondary atomization model (e.g. [82, 83]).

6.4 Limitations and paths for improvement

With the goal of investigating the primary breakup process, a decision was made to focus on the pure fluid mechanics of droplet formation and decouple the thermodynamic effects, except for the initial setup calibration based on the reference 1D model RP-e. This introduced some artificial variables and approximations, found to be compatible with the goal of systematically characterizing the breakup process and producing data suitable to be used in SGS modeling. However, it also limited the range of results that can be extracted.

One of the main limiting aspects previously noted is the assumption that all bubbles in the domain nucleate simultaneously and with equal or average spacing that is treated as a free variable. This was necessary to allow the use of a globally calibrated vaporization rate or $\dot{R}$ and was partially motivated by the lack of a reliable model to predict the nuclei number density. This assumption is artificial since bubbles would nucleate continuously at a rate determined by the thermodynamic parameters T_∞ and p_∞ or superheat level. To avoid this assumption, for a given nucleation rate, the growth rate must be time dependent and calculated independently for each bubble. More generally, vaporization mass fluxes should be computed in each interface cell based on local pressure and temperature, implying the solution of an energy equation in the DNS.

Even though such capabilities are available and fully developed in `FS3D` [56, 59], it was ultimately unsuitable for the present study due to the mesh resolution required to capture the thin thermal boundary layer developing around the bubbles.

Using the RP-e model, the TBL thickness, defined as the point of $0.99\,T_\infty$,has been computed to vary between 25 and 5% of the instantaneous bubble radius.

In addition to a sufficiently resolved temperature gradient, the mass fluxes can only be accurately computed when taking into account the variation in vapour density, as the internal pressure inside each bubble relaxes towards p_∞. This requires the use of a weakly compressible formulation, i.e. the use of an equation of state for the gas phase, even if the propagation of pressure waves is not necessarily resolved in time.

With increasing availability of HPC power, such approach is possible to implement with `FS3D`. However, it would remain computationally inefficient due to the use of uniform structured meshes. Alternatively, adaptive mesh refinement techniques available in commercial solvers would provide an essential advantage.

One important result that has been omitted in this work, is droplet velocity statistics. Although such data is readily available in post-processing, it was found to be non-significant. As noted in Sec. 4.2, there is a direct relationship between the expected flow velocities in the outer regions of the domain and the number of bubbles included in the simulation. This is due to the cumulative effect of multiple bubbles growing along a radial direction from the centre of the domain. Consequently, there is a direct influence of the number of bubbles initialized for each case on the speed of the ejected droplets. With the assumption of incompressibility, the droplet velocity is thus effectively proportional to $\sqrt[3]{N_{\mathrm{bub}}}\dot{R}$. With more detailed modeling, pressure gradients would develop towards the centre of the cluster as a reaction to the bubble expansion, causing a progressive reduction of the growth rate towards the centre of the domain, as demonstrated by Dietzel et al. [60]. Additionally, they demonstrated that along a radial direction, the number of bubbles that experience a significant growth is limited to less than 10. This is in line with the number of bubbles initialized in the DNS domain for the present work, although compressibility effects are not considered. Even though the cumulative velocity effect was not observed to have a significant influence on the breakup process itself, a compressible framework would again be required to obtain relevant data on droplet velocity after breakup.

Finally, the inclusion of energy transport in the DNS would also provide valuable information on the droplet temperature after breakup, which has important implications for combustion applications. It is expected that droplets are cooled by different degrees depending on the breakup regime or stage of bubble growth at which they are formed. Furthermore, they would continue to evaporate into the low pressure environment at a rate that may be significantly higher than the one

calculated for the internal bubble interface. Rapid droplet vaporization can also explain the lack of empirical evidence for sub-micron droplet sizes, that have been predicted for higher temperatures by the pure fluid-mechanical DNS.

Chapter 7

Conclusions and Outlook

7.1 Conclusion

This work has sought to, for the first time, simulate the primary breakup mechanism driving flash boiling atomization of cryogenic fluids. This has been achieved using DNS methods, fully resolving the liquid vapour interface for very large numbers of bubbles and droplets at the microscopic scale. The methodology used here strikes a balance between computational cost and physical accuracy by simulating only the pure fluid-mechanics after an initial calibration step of the thermodynamic variables. The approach has also allowed levels of mesh resolution below the Kolmogorov and Hinze scales, not previously reached by atomization DNS studies found in the literature.

Across a wide range of initial conditions, a series of distinct primary breakup regimes has been verified. The regimes are characterized in terms of dimensionless Weber and Ohnesorge numbers, allowing the prediction of the expected breakup behaviour and resulting spray qualities. The observations are in partial agreement, but extending beyond previously hypothesised breakup mechanics and empirical observation.

It has been shown that in addition to the fluid temperature that defines the initial conditions, the type of breakup observed is largely dependent on the initial nuclei spacing, which is treated as a free variable in this study. This degree of freedom can in principle be suppressed as long as a local nucleation rate can be accurately estimated.

A series of large test cases provides statistical data, that can be used to predict mean droplet sizes generated at different thermodynamic conditions. An essential advantage of DNS is the provision of independent measurements of droplet volume

and area to calculate a "true" Sauter mean diameter. Furthermore, conditions simulated probe into extreme spatio-temporal scales and may represent regions of the spray that are not accessible via experimental methods.

The results suggest that, for relatively high fluid temperatures or high levels of local superheat, droplets can be formed in the sub-micron range and at equally small time scales. These are beyond the range accessible by empirical methods. At more conservative levels of superheat, the method suggests droplets in the one to ten micron range, that is compatible with empirical evidence. However, this is at the limit of the range tested by DNS and implies higher computational cost.

The results, normalized in terms of Weber number, provide predictive models that can be applied to a range of conditions and fluids, to estimate the rate of surface area generation and final droplet size distribution. These models are particularly well suited to be used as sub-grid-scale (SGS) closure in large scale simulations of the complete spray for practical engineering applications.

Overall, this PhD thesis provides new insights into the flash atomization of cryogenic rocket propellants, with potential applications in the design and optimization of rocket engines. The findings may have significant implications for the development of more efficient and reliable rocket propulsion systems, contributing to the advancement of space exploration and the broader field of aerospace engineering.

7.2 Outlook and suggestions for future work

Technical improvements to the methodology presented here, in particular the use of a weakly compressible framework and the inclusion of the energy transport equation, could significantly extend the range of results that can be extracted. This includes final droplet temperature and droplet ejection velocities. This level of physical accuracy is within the capabilities of current CFD codes and HPC, including the ones used in this work. However, it would benefit from adaptive mesh refinement techniques to allow sufficient and affordable resolution of the liquid-vapour interfaces.

The overlap of the DNS results with available empirical data seems to occur at the end of the range of conditions tested, that is associated with the largest time and length scales. Thus, it is worth evaluating conditions beyond this range. A combination of the flash atomization mechanisms found here and common secondary aerodynamic breakup should be considered. At larger scales it also becomes important to consider macroscopic velocity gradients, e.g, associated with the nozzle geometry, which can enhance the breakup process.

The breakup mechanics suggested by this study, including the lower Weber number regime and higher levels of superheat, can, in principle, be empirically verified. For this, small jets of the order of 10 to 100 µm in diameter and high flow velocities should be considered, such that external flashing and homogeneous nucleation is promoted. Shadowgraphy techniques can then be used employing in-vacuum microscope objectives together with high intensity short-pulsed illumination and high speed cameras. State-of-the-art high speed imaging capture technologies currently allow for sequential acquisition times the order of 200 ns. Similar levels of time resolution are also achievable as individual snapshots with conventional cameras, through the use of very short light pulses. However, to observe the breakup dynamics at the level of the critical radius, the required level of optical magnification is at the limit of resolution achievable by visible light (0.5 µm), suggesting the need for shorter wave-length light, such as X-ray.

Although outside the scope of the present work, the author has found that the above suggested experimental approach has a great potential, resulting from subsequent professional activities at the time of the writing of this thesis. This is evidenced by the images provided in Fig. 7.1, which were obtained using the *CryoJet* platform currently under development at HED - European XFEL, where world-class X-ray laser diagnostics are also provided.

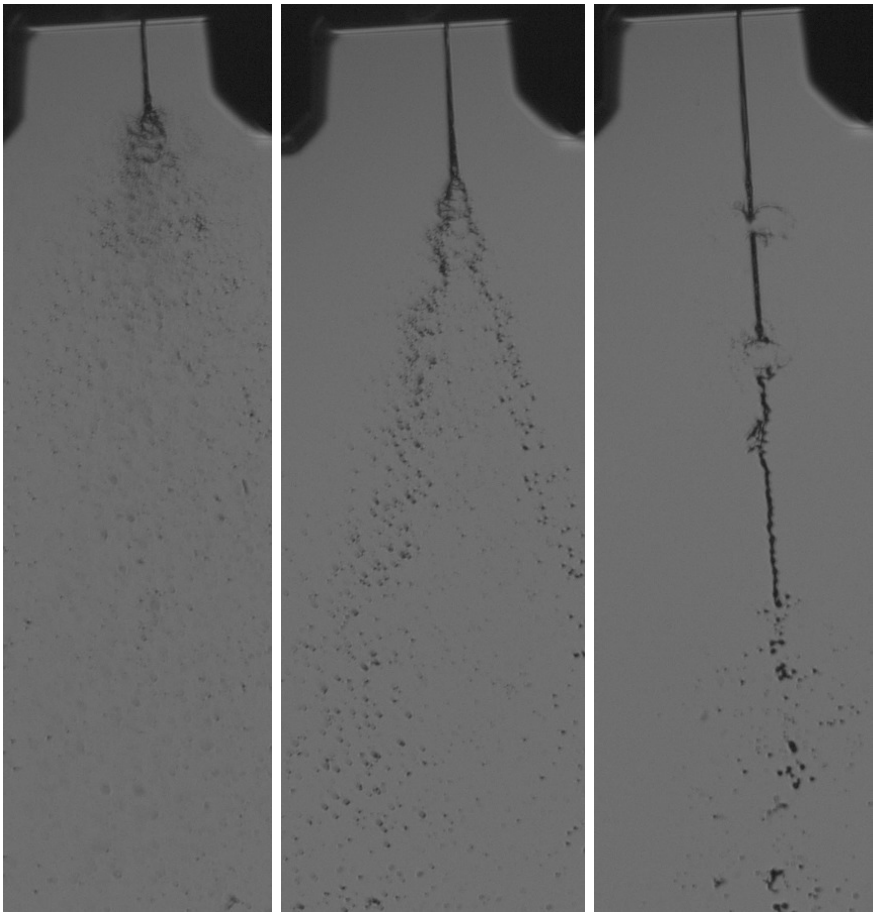

Figure 7.1: Experimental evidence for a LN2 jet (diam. 20 µm) undergoing external flash boiling under controlled steady-state conditions in high-vacuum (5×10^{-5} mbar) at temperatures ranging from 83 to 74K (from left to right). With decreasing temperature and implied reduction of the nucleation rate, the flashing regime transitions from a fine spray with sub-micron droplets to localized micro-explosions, that are respectively comparable to the low and high We_b regimes covered in this work. The images are obtained with short-pulsed illumination of 0.2 µs and conventional scientific camera (Basler) behind a long-distance microscope (in air). *Unpublished images produced by the author, included with permission from the responsible scientist at HED - European XFEL, Dr. Sebastian Göde.*

Bibliography

[1] Daniel D. Loureiro, Jonathan Reutzsch, Dirk Dietzel, Andreas Kronenburg, Bernhard Weigand, and Konstantina Vogiatzaki. DNS of multiple bubble growth and droplet formation in superheated liquids. In *14th International Conference on Liquid Atomization and Spray Systems ,Chicago, IL, USA*, July 2018. doi: 10.18419/opus-10342.

[2] Daniel D. Loureiro, Jonathan Reutzsch, Andreas Kronenburg, Bernhard Weigand, and Konstantina Vogiatzaki. Resolving breakup in flash atomization conditions using DNS. In *10th International Conference on Multiphase Flow, Rio de Janeiro*, July 2019. doi: 10.18419/opus-10488.

[3] Daniel D. Loureiro, Jonathan Reutzsch, Andreas Kronenburg, Bernhard Weigand, and Konstantina Vogiatzaki. Towards full resolution of spray breakup in flash atomization conditions using DNS. In *High Performance Computing in Science and Engineering '19*, pages 209–224. Springer International Publishing, 2021. ISBN 978-3-030-66792-4. doi: 10.1007/978-3-030-66792-4.

[4] Daniel D. Loureiro, Jonathan Reutzsch, Andreas Kronenburg, Bernhard Weigand, and Konstantina Vogiatzaki. Primary breakup regimes for cryogenic flash atomization. *International Journal of Multiphase Flow*, 132:103405, 2020. ISSN 0301-9322. doi: 10.1016/j.ijmultiphaseflow.2020.103405.

[5] Daniel D. Loureiro, Andreas Kronenburg, Jonathan Reutzsch, Bernhard Weigand, and Konstantina Vogiatzaki. Droplet size distributions in cryogenic flash atomization. *International Journal of Multiphase Flow*, 142:103705, 2021. ISSN 0301-9322. doi: 10.1016/j.ijmultiphaseflow.2021.103705.

[6] Hengjie Guo, Xiao Ma, Yanfei Li, Shuai Liang, Zhi Wang, Hongming Xu, and Jianxin Wang. Effect of flash boiling on microscopic and macroscopic spray characteristics in optical gdi engine. *Fuel*, 190:79–89, 2017. ISSN 0016-2361. doi: 10.1016/j.fuel.2016.11.043.

[7] Eran Sher and Chaim Elata. Spray formation from pressure cans by flashing. *Industrial & Engineering Chemistry Process Design and Development*, 16(2): 237–242, 1977.

[8] Minoo Razzaghi. Droplet size estimation of two-phase flashing jets. *Nuclear Engineering and Design*, 114(1):115 – 124, 1989. ISSN 0029-5493. doi: 10.1016/0029-5493(89)90130-1.

[9] John D. Clark. *Ignition!: An Informal History of Liquid Rocket Propellants*. Rutgers University Press, 1972. ISBN 9780813507255.

[10] Eric Wernimont and Mark Ventura. *Review of US Historical Rocket Propellants: Accidents, Mishaps and Fatalities*. 2007. doi: 10.2514/6.2007-5648.

[11] Eric Hurlbert, John Applewhite, Tien Nguyen, Brian Reed, Zhang Baojiong, and Wang Yue. Nontoxic Orbital Maneuvering and Reaction Control Systems for Reusable Spacecraft. *Journal of Propulsion and Power*, 14(5):676–687, 1998. ISSN 0748-4658. doi: 10.2514/2.5330.

[12] Amir S. Gohardani, Johann Stanojev, Alain Demairé, Kjell Anflo, Mathias Persson, Niklas Wingborg, and Christer Nilsson. Green space propulsion: Opportunities and prospects. *Progress in Aerospace Sciences*, 71:128–149, 2014. ISSN 0376-0421. doi: 10.1016/j.paerosci.2014.08.001.

[13] Marco De Rosa, Jo Sender, Herbert Zimmermann, and Michael Oschwald. *Cryogenic Spray Ignition at High Altitude Conditions*. 2006. doi: 10.2514/6.2006-4539.

[14] Chiara Manfletti. Laser Ignition of an Experimental Cryogenic Reaction and Control Thruster: Pre-Ignition Conditions. *Journal of Propulsion and Power*, 30(4):925–933, 2014.

[15] Matthew J Atwell, Eric A Hurlbert, John C Melcher, and Robert L Morehead. Characterization of a pressure-fed lox/lch4 reaction control system under simulated altitude and thermal vacuum conditions. In *53rd AIAA/SAE/ASEE Joint Propulsion Conference*, page 4668, 2017.

[16] Jan Wilhelm Gärtner, Andreas Kronenburg, Andreas Rees, Joachim Sender, Michael Oschwald, and Grazia Lamanna. Numerical and experimental analysis of flashing cryogenic nitrogen. *International Journal of Multiphase Flow*, 130: 103360, 2020. ISSN 0301-9322. doi: 10.1016/j.ijmultiphaseflow.2020.103360.

[17] Ralph Brown and J. Louis York. Sprays formed by flashing liquid jets. *AIChE Journal*, 8(2):149–153, 1962. doi: 10.1002/aic.690080204.

[18] Eran Sher, Tali Bar-Kohany, and A Rashkovan. Flash-boiling atomization. *Progress in Energy and Combustion Science*, 34:417–439, 08 2008.

[19] Grazia Lamanna, Hend Kamoun, Bernhard Weigand, and Johan Steelant. Towards a unified treatment of fully flashing sprays. *International Journal of Multiphase Flow*, 58:168 – 184, 2014.

[20] Andrew S. Thompson and Stephen D. Heister. Characteristics Of Flashing Flows Within a High Aspect Ratio Injector. *Atomization and Sprays*, 26(7): 633–658, 2016. ISSN 1044-5110.

[21] Tali Bar-Kohany and Moti Levy. State of the art review of flash-boiling atomization. *Atomization and Sprays*, 26(12):1259–1305, 2016. ISSN 1044-5110.

[22] Yoshiro Kitamura, Hiroichi Morimitsu, and Teruo Takahashi. Critical superheat for flashing of superheated liquid jets. *Industrial & engineering chemistry fundamentals*, 25(2):206–211, 1986.

[23] M. M. Vieira and J. R. Simões-Moreira. Low-pressure flashing mechanisms in iso-octane liquid jets. *Journal of Fluid Mechanics*, 572:121–144, 2007. doi: 10.1017/S0022112006003430.

[24] Tariq Alghamdi, Sigurdur T. Thoroddsen, and J.F. Hernández-Sánchez. Ultra-high speed visualization of a flash-boiling jet in a low-pressure environment. *International Journal of Multiphase Flow*, 110:238–255, 2019. ISSN 0301-9322. doi: 10.1016/j.ijmultiphaseflow.2018.08.004.

[25] Vincent Cleary, Phil Bowen, and Henk Witlox. Flashing liquid jets and two-phase droplet dispersion: I. experiments for derivation of droplet atomisation correlations. *Journal of Hazardous Materials*, 142(3):786 – 796, 2007. ISSN 0304-3894. doi: 10.1016/j.jhazmat.2006.06.125.

[26] Meng Luo and Oskar J. Haidn. Characterization of Flashing Phenomena with Cryogenic Fluid Under Vacuum Conditions. *Journal of Propulsion and Power*, 32(5):1253–1263, 2016. ISSN 0748-4658. doi: 10.2514/1.B35963.

[27] Andreas Rees, Lucio Araneo, Heiko Salzmann, Grazia Lamanna, Joachim Sender, and Michael Oschwald. Droplet velocity and diameter distributions

in flash boiling liquid nitrogen jets by means of phase doppler diagnostics. *Experiments in Fluids*, 61(8):1–18, 2020.

[28] Renaud Lecourt, Philippe Barricau, and Johan Steelant. Spray velocity and drop size measurements in flashing conditions. *Atomization and Sprays*, 19(2): 103–133, 2009. doi: 10.1615/AtomizSpr.v19.i2.10.

[29] M. Levy, Y. Levy, and E. Sher. Spray structure as generated under homogeneous flash boiling nucleation regime. *Applied Thermal Engineering*, 73(1):416 – 423, 2014. doi: 10.1016/j.applthermaleng.2014.08.008.

[30] Henk W.M. Witlox, Mike Harper, Adeyemi Oke, Philip J. Bowen, and Peter Kay. Sub-cooled and flashing liquid jets and droplet dispersion i. overview and model implementation/validation. *Journal of Loss Prevention in the Process Industries*, 23(6):831–842, 2010. doi: 10.1016/j.jlp.2010.07.004.

[31] J. O. Hinze. Fundamentals of the hydrodynamic mechanism of splitting in dispersion processes. *AIChE Journal*, 1(3):289–295, 1955. doi: 10.1002/aic.690010303.

[32] Nasser Ashgriz. *Handbook of atomization and sprays: theory and applications*. Springer Science & Business Media, 2011.

[33] Grazia Lamanna, H. Kamoun, Bernhard Weigand, C. Manfletti, A. Rees, J. Sender, M. Oschwald, and Johan Steelant. Flashing behavior of rocket engine propellants. *Atomization and Sprays*, 25(10):837–856, 2015. ISSN 1044-5110.

[34] M So Plesset and So A Zwick. The growth of vapor bubbles in superheated liquids. *Journal of applied physics*, 25(4):493–500, 1954.

[35] Rajshekhar D. Oza and James F. Sinnamon. An experimental and analytical study of flash-boiling fuel injection. *SAE Transactions*, 92:948–962, 1983.

[36] Ho Sung Lee and Herman Merte. Spherical vapor bubble growth in uniformly superheated liquids. *International Journal of Heat and Mass Transfer*, 39(12): 2427–2447, 1996.

[37] Andrea Prosperetti. Vapor bubbles. *Annual review of fluid mechanics*, 49, 2017.

[38] Jiro Senda, Yoshiyuki Hojyo, and Hajime Fujimoto. Modeling on atomization and vaporization process in flash boiling spray. *Jsae Review*, 15(4):291–296, 1994.

[39] Yangbing Zeng and Chia-Fon F Lee. An atomization model for flash boiling sprays. *Combustion Science and Technology*, 169(1):45–67, 2001.

[40] Christopher Price, Arash Hamzehloo, Pavlos Aleiferis, and David Richardson. Numerical modelling of droplet breakup for flash-boiling fuel spray predictions. *International Journal of Multiphase Flow*, 125:103183, 2020. ISSN 0301-9322. doi: 10.1016/j.ijmultiphaseflow.2019.103183.

[41] Geoffrey Ingram Taylor. The dynamics of thin sheets of fluid ii. waves on fluid sheets. *Proceedings of the Royal Society of London. Series A. Mathematical and Physical Sciences*, 253(1274):296–312, 1959. doi: 10.1098/rspa.1959.0195.

[42] RK Calay and AE Holdo. Modelling the dispersion of flashing jets using cfd. *Journal of Hazardous Materials*, 154(1-3):1198–1209, 2008.

[43] J. Lee, R. Madabhushi, C. Fotache, S. Gopalakrishnan, and D. Schmidt. Flashing flow of superheated jet fuel. *Proceedings of the Combustion Institute*, 32(2): 3215 – 3222, 2009. ISSN 1540-7489. doi: 10.1016/j.proci.2008.06.153.

[44] J. Chesnel, Julien Reveillon, Thibaut Menard, and Francois-Xavier Demoulin. Large eddy simulation of liquid jet atomization. *Atomization and Sprays*, 21 (9):711–736, 2011. ISSN 1044-5110.

[45] S Navarro-Martinez. Large eddy simulation of spray atomization with a probability density function method. *International Journal of Multiphase Flow*, 63: 11–22, 2014.

[46] IK Karathanassis, P Koukouvinis, and M Gavaises. Comparative evaluation of phase-change mechanisms for the prediction of flashing flows. *International Journal of Multiphase Flow*, 95:257–270, 2017.

[47] Salvador Navarro-Martinez, Giovanni Tretola, Mohammad Reza Yosri, Robert L Gordon, and Konstantina Vogiatzaki. An investigation on the impact of small-scale models in gasoline direct injection sprays (ecn spray g). *International Journal of Engine Research*, 21(1):217–225, 2020. doi: 10.1177/1468087419889449.

[48] Roland Schmehl and Johan Steelant. Computational analysis of the oxidizer preflow in an upper-stage rocket engine. *Journal of Propulsion and Power*, 25 (3):771–782, 2009.

[49] R. Lebas, T. Menard, P.A. Beau, A. Berlemont, and F.X. Demoulin. Numerical simulation of primary break-up and atomization: DNS and modelling study. *International Journal of Multiphase Flow*, 35(3):247 – 260, 2009. doi: 10.1016/j.ijmultiphaseflow.2008.11.005.

[50] Mikhael Gorokhovski and Marcus Herrmann. Modeling primary atomization. *Annual Review of Fluid Mechanics*, 40(1):343–366, 2008. doi: 10.1146/annurev.fluid.40.111406.102200.

[51] Olivier Desjardins, Vincent Moureau, and Heinz Pitsch. An accurate conservative level set/ghost fluid method for simulating turbulent atomization. *Journal of Computational Physics*, 227:8395–8416, 09 2008. doi: 10.1016/j.jcp.2008.05.027.

[52] J Shinjo and A Umemura. Simulation of liquid jet primary breakup: Dynamics of ligament and droplet formation. *International Journal of Multiphase Flow*, 36(7):513–532, 2010.

[53] Moritz Ertl, Jonathan Reutzsch, Arne Nägel, Gabriel Wittum, and Bernhard Weigand. Towards the implementation of a new multigrid solver in the DNS code FS3D for simulations of shear-thinning jet break-up at higher reynolds numbers. In *High Performance Computing in Science and Engineering ' 17*, pages 269–287. Springer International Publishing, 2018. ISBN 978-3-319-68394-2.

[54] J.-L. Estivalezes, W. Aniszewski, F. Auguste, Y. Ling, L. Osmar, J.-P. Caltagirone, L. Chirco, A. Pedrono, S. Popinet, A. Berlemont, J. Magnaudet, T. Ménard, S. Vincent, and S. Zaleski. A phase inversion benchmark for multiscale multiphase flows. *Journal of Computational Physics*, 450:110810, 2022. ISSN 0021-9991. doi: 10.1016/j.jcp.2021.110810.

[55] Xiaodong Chen, Dongjun Ma, Vigor Yang, and Stephane Popinet. High-fidelity simulations of impinging jet atomization. *Atomization and Sprays*, 23(12):1079–1101, 2013. ISSN 1044-5110.

[56] J. Schlottke and B. Weigand. Direct numerical simulation of evaporating droplets. *Journal of Computational Physics*, 227:5215–5237, 2008.

[57] Christian Kunkelmann and Peter Stephan. Cfd simulation of boiling flows using the volume-of-fluid method within openfoam. *Numerical Heat Transfer, Part A: Applications*, 56(8):631–646, 2009. doi: 10.1080/10407780903423908.

[58] John Palmore and Olivier Desjardins. A volume of fluid framework for interface-resolved simulations of vaporizing liquid-gas flows. *Journal of Computational Physics*, 399:108954, 2019. ISSN 0021-9991. doi: https://doi.org/10.1016/j.jcp.2019.108954.

[59] Jonathan Reutzsch, Corine Kieffer-Roth, and Bernhard Weigand. A consistent method for direct numerical simulation of droplet evaporation. *Journal of Computational Physics*, 413:109455, 2020. ISSN 0021-9991. doi: 10.1016/j.jcp.2020.109455.

[60] D. Dietzel, T. Hitz, C.-D. Munz, and A. Kronenburg. Numerical simulation of the growth and interaction of vapour bubbles in superheated liquid jets. *International Journal of Multiphase Flow*, 121:103 – 112, 2019. doi: 10.1016/j.ijmultiphaseflow.2019.103112.

[61] VP Carey. *Liquid-vapor phase-change phenomena.* Taylor & Francis Inc., Bristol PA, USA, 1992.

[62] Ian H. Bell, Jorrit Wronski, Sylvain Quoilin, and Vincent Lemort. Pure and pseudo-pure fluid thermophysical property evaluation and the open-source thermophysical property library coolprop. *Industrial & Engineering Chemistry Research*, 53(6):2498–2508, 2014. doi: 10.1021/ie4033999.

[63] Lord Rayleigh. Viii. on the pressure developed in a liquid during the collapse of a spherical cavity. *The London, Edinburgh, and Dublin Philosophical Magazine and Journal of Science*, 34(200):94–98, 1917.

[64] A.J. Robinson and R.L. Judd. The dynamics of spherical bubble growth. *International Journal of Heat and Mass Transfer*, 47(23):5101 – 5113, 2004. ISSN 0017-9310. doi: 10.1016/j.ijheatmasstransfer.2004.05.023.

[65] B.B Mikic, W.M Rohsenow, and P Griffith. On bubble growth rates. *International Journal of Heat and Mass Transfer*, 13(4):657 – 666, 1970. ISSN 0017-9310. doi: 10.1016/0017-9310(70)90040-2.

[66] Osamu Miyatake, Itsuo Tanaka, and Noam Lior. A simple universal equation for bubble growth in pure liquids and binary solutions with a nonvolatile solute. *International Journal of Heat and Mass Transfer*, 40(7):1577–1584, 1997. ISSN 0017-9310. doi: 10.1016/S0017-9310(96)00224-4.

[67] M. Shusser, T. Ytrehus, and D. Weihs. Kinetic theory analysis of explosive boiling of a liquid droplet. *Fluid Dynamics Research*, 27(6):353 – 365, 2000. ISSN 0169-5983. doi: 10.1016/S0169-5983(00)00015-0.

[68] Aaron H Persad and Charles A Ward. Expressions for the evaporation and condensation coefficients in the hertz-knudsen relation. *Chemical reviews*, 116 (14):7727–7767, 2016.

[69] E Lauer, XY Hu, Stefan Hickel, and Nikolaus Andreas Adams. Numerical modelling and investigation of symmetric and asymmetric cavitation bubble dynamics. *Computers & Fluids*, 69:1–19, 2012.

[70] Dirk Dietzel. *Modeling and simulation of flash-boiling of cryogenic liquids*. PhD thesis, Universität Stuttgart, 2020.

[71] Raunak Bardia and Mario F. Trujillo. Assessing the physical validity of highly-resolved simulation benchmark tests for flows undergoing phase change. *International Journal of Multiphase Flow*, 112, 12 2018. doi: 10.1016/j.ijmultiphaseflow.2018.11.018.

[72] K. Eisenschmidt, M. Ertl, H. Gomaa, C. Kieffer-Roth, C. Meister, P. Rauschenberger, M. Reitzle, K. Schlottke, and B. Weigand. Direct numerical simulations for multiphase flows: An overview of the multiphase code FS3D. *Journal of Applied Mathematics and Computation*, 272(2):508–517, 1 2016.

[73] Francis H Harlow and J Eddie Welch. Numerical calculation of time-dependent viscous incompressible flow of fluid with free surface. *The physics of fluids*, 8 (12):2182–2189, 1965.

[74] Martin Rieber. *Numerische Modellierung der Dynamik freier Grenzflächen in Zweiphasenströmungen*. PhD thesis, Universität Stuttgart, 2004.

[75] William J Rider and Douglas B Kothe. Reconstructing volume tracking. *Journal of computational physics*, 141(2):112–152, 1998.

[76] Bruno Lafaurie, Carlo Nardone, Ruben Scardovelli, Stéphane Zaleski, and Gianluigi Zanetti. Modelling merging and fragmentation in multiphase flows with surfer. *Journal of Computational Physics*, 113(1):134 – 147, 1994. ISSN 0021-9991.

[77] M. Liu and D. Bothe. Numerical study of head-on droplet collisions at high weber numbers. *Journal of Fluid Mechanics*, 789:785–805, 2016. doi: 10.1017/jfm.2015.725.

[78] Donald Ervin Knuth. *The Art of Computer Programming, Vol. 2, 3rd ed.* Addison-Wesley, 1997. ISBN 0-201-89684-2.

[79] Stephen B Pope and Stephen B Pope. *Turbulent flows*. Cambridge university press, 2000.

[80] Fred EC Culick. Comments on a ruptured soap film. *Journal of applied physics*, 31(6):1128–1129, 1960.

[81] Gilou Agbaglah, Christophe Josserand, and Stéphane Zaleski. Longitudinal instability of a liquid rim. *Physics of Fluids*, 25(2):022103, 2013. doi: 10.1063/1.4789971.

[82] Rolf D Reitz and R Diwakar. Effect of drop breakup on fuel sprays. *SAE transactions*, pages 218–227, 1986.

[83] Peter J O'Rourke and Anthony A Amsden. The tab method for numerical calculation of spray droplet breakup. Technical report, SAE technical paper, 1987.

[84] P Vassallo and N Ashgriz. Satellite formation and merging in liquid jet breakup. *Proc. R. Soc. Lond. A*, 433(1888):269–286, 1991.

[85] Ilia V Roisman. Dynamics of inertia dominated binary drop collisions. *Physics of Fluids*, 16(9):3438–3449, 2004.

[86] Suhas V Patankar. *Numerical heat transfer and fluid flow*. CRC press, 2018.

[87] John W. Eaton, David Bateman, Søren Hauberg, and Rik Wehbring. *GNU Octave version 5.2.0 manual: a high-level interactive language for numerical computations*, 2020. URL `https://www.gnu.org/software/octave/doc/v5.2.0/`.

Appendix A

Boundary condition implementation

Two types of boundary conditions (BC), *Symmetry* and *Outflow*, are used in this work, that must be applied to the three components of the velocity field $\boldsymbol{u}$ and the VOF scalar f. The boundary values for p, gradients and other intermediate variables are then computed as described in Sec. 4.1. In `FS3D` the BC are implemented through the use of ghost cells at the edges of the domain where the values of the field variables are asserted according to rules that provide the intended gradients or fixed values. For an N-cell domain in a given direction where u is the normal velocity component, this is implemented as follows.[1]

In the case of symmetry BC, the values in the two ghost cells are copied from the last two cells of the domain in reverse order, creating a mirror image and gradients with opposite signs

$$f_{N+1} = f_N \qquad \text{and} \qquad f_{N+2} = f_{N-1} \tag{A1}$$

The resulting zero-gradient implies that the PLIC reconstructed interface plane is always perpendicular to the domain edge (Eq. (4.8)). For the velocity field, symmetry is equivalent to a free-slip wall implying a zero-velocity component in the direction normal to the domain edge u,

$$u_N = u_{N+1} = u_{N+2} = 0 \tag{A2}$$

[1]For brevity BCs are defined here for one face of the domain and its normal velocity component u, with the subscript N being used to refer to the index of last cell of the domain (boundary cell) in the x direction. Indexes $N+1$ and $N+2$ are the ghost cells that define the type of boundary condition. The BCs can be promptly generalized for the first cell (where index is 1 and the ghost cells are 0 and -1) and to the y and z directions. Due to the use of a MAC staggered grid, the velocity is computed at the cell boundary, so index 0 and N correspond to ghost values the outer edges of the first and last cells.

and zero-gradient for the parallel components v and w.

The outflow BC, also known as *continuative*, implies that all fields are constant beyond the edges of the domain and thus have a zero-gradient. This suggests

$$f_{N+1} = f_{N+2} = f_N \tag{A3}$$

for the VOF, assuming that cell N contains pure liquid ($f_N = 1$) or pure vapour ($f_N = 0$). Analogously, for the velocity

$$u_N = u_{N+1} = u_{N+2} = u_{N-1} \tag{A4}$$

Although it is customary to place the outflow boundary conditions far from the region of interest with large buffer zones, in this work this is not always possible without dramatically increasing the computational cost. Due to the bubble expansion and some drops being ejected at high velocities, the liquid vapour interface will eventually reach the BC, either in the form of a growing bubble submerged in liquid or a droplet surrounded by gas. This implies $0 < f_N < 1$ and an immediate smearing of the interface in the ghost cells through Eq. (A3). Furthermore $\dot{m}'' > 0$ implies $\nabla \cdot \boldsymbol{u} \neq 0$ that is inconsistent with the imposed velocities. This results in solver instability that effectively halts the simulation once an interface reaches the edge of the domain. Thus an adapted outflow condition was implemented.

First, $\dot{m}'' = 0$ is imposed in the ghost cells, independently of the presence of an interface. Second, to ensure that there is no inflow due to surface tension forces, the normal component of the velocity is set to zero in the ghost cells, if the value in the last cell is negative (or positive for BC at cell 1):

$$u_N = u_{N+1} = u_{N+2} = \begin{cases} u_{N-1} & \text{if} \quad u_{N-1} \geq 0 \\ 0 & \text{if} \quad u_{N-1} < 0 \end{cases} \tag{A5}$$

Finally, for the f value, a more complex treatment is required. The ghost cells must be able to switch from $f = 1$ to $f = 0$ for an approaching bubble interface, or vice-versa for an approaching droplet (in both cases the interface is locally parallel to the domain edge). The solution must, however, also be able to take values $0 < f < 1$ if the interface has crossed the boundary and is not parallel, e.g. if $f_{N-1} = f_N$ then $\frac{df}{dx} = 0$ and the interface is normal to the boundary, so the ghost cells should both take an intermediate value. This suggests that the ghost f values should be extrapolated based on the f value and its gradient at the boundary. Assuming a

constant cell width, the linear extrapolation becomes

$$f_{N+1} = 2f_N - f_{N-1}$$
$$f_{N+2} = 2f_{N+1} - f_N. \tag{A6}$$

Contrary to the symmetry case, here the gradient in the ghost cells has the same direction as the boundary cells. To ensure $0 \leq f \leq 1$, this must be followed by a second operation that caps the f value. On one hand, to prevent interface smearing, it is desirable to exaggerate the change as a step function, such that ghost cells immediately take the value 1 or 0 based on the direction of the gradient. This can be simply achieved by an integer-rounding operation. On the other hand, a smooth and continuous function is required for solver stability, that still permits an extrapolated value when $0 < f < 1$ and $\frac{df}{dx} \approx 0$.

The solution is achieved through an S-curve (Logistic function) given by

$$f_s = \frac{1}{2} + \frac{1}{2}\tanh\left(a_s\left[f_e - \frac{1}{2}\right]\right) \tag{A7}$$

where f_e is the extrapolated value given by Eq. (A6), and a_s can be adjusted to define the steepness of the S-curve. I.e., with low a_s values f_s tend to the extrapolated value given by (A6) (capped to 0 or 1), while for large a_s values it tends to the square step given by a rounding operation. For the cases tested $a_s = 50$ seems to be a good compromise, allowing all interface orientations to contact the BC, without affecting the solver stability for a wide range of mesh resolutions. It should be noted, however, that this simple implementation is only to improve solver stability and may still cause artificial effects on the interface reconstruction at the domain boundary.

Appendix B

Cost projection in HPC

The simulations with the `FS3D` code were initially performed on the *Hazel-Hen* HPC system at the High Performance Computing Center Stuttgart (HLRS). It was later succeeded by the *Hawk* system, which was used for the simulations presented in Secs. 5.1 and 5.3. In particular, the simulations with 512^3 and 1024^3 meshes would not be possible without the use of a HPC and parallelization of the order of 2000 CPU-cores. Although test cases are still relatively small for this kind of state-of-the-art HPC, it is important to consider the aim to perform a relatively large number of test cases, covering a significant range of initial thermodynamic conditions or points in the We_b-Oh_b range, rather than a single very large representative test case.

All simulations make use of Message Passing Interface (MPI) parallelization technique implemented in the `FS3D`. One important metric for the HPC performance of a CFD code is the strong-scaling factor, which has been evaluated with the *Hazel-Hen* system. Figure B1 shows the computational speed, ν, as a function of N_{proc}. The annotated percentages indicate the corresponding efficiency η for each case. It was found that for a 1024^3 mesh, the peak performance is obtained with 2048 cores or, equivalently, when each CPU core solves a sub domain of $64 \times 64 \times 128$ (0.5 million) cells. This allocation was used in subsequent work in spite of a relatively poor scaling efficiency of 59%. The latter was improved with the transition to the Hawk system and improvements to the solver.

For a DNS simulation with explicit time integration and a constant time-step, the wall-time is roughly the time it takes to solve the system of equations for one time step multiplied by the number of time steps necessary to reach the desired physical time. Physically larger domains could, in principle, be simulated within the same wall-time if the mesh and number of processors is increased proportionally (weak scaling). Conversely, increasing resolution for the same domain size leads to

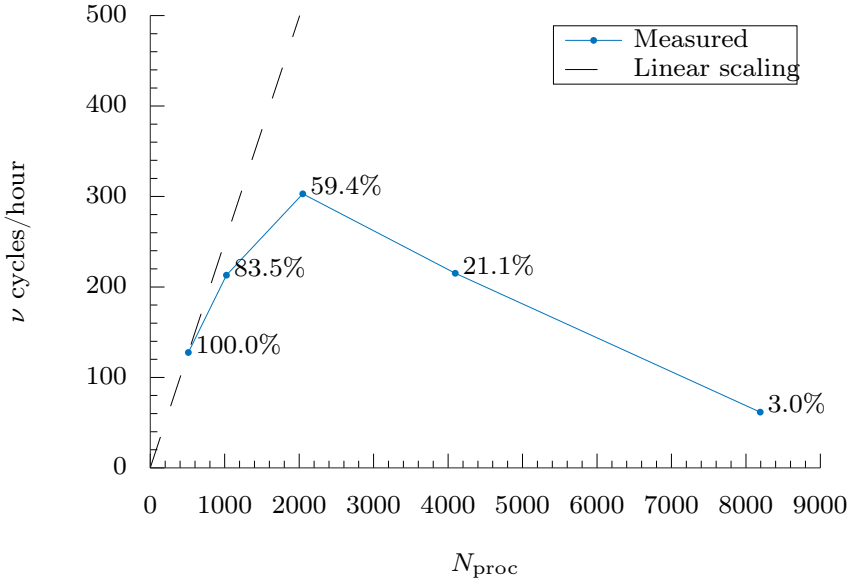

Figure B1: Results for strong-scaling on a 1024^3 grid grid, comparing compute speed to ideal linear scaling (scaling efficiency in annotations).

an increase in wall-time (in spite of proportional computing power) due to an implied reduction of the time-step. No limitations have been found in terms weak-scaling. However, the use of meshes larger than 1024^3 was not pursued in this work due to practical limitations in terms of data storage and post-processing, given the need for a fine resolution in the time domain.

The time-step is limited by the stability criterion for the explicit time integration, known as the Courant–Friedrichs–Lewy (CFL) condition [86]. In `FS3D` the CFL condition is generalized to account not only for the time scale of fluid advection, but also viscous dissipation and surface tension or capillary wave propagation speed. As a consequence, the criterion for stability and thus the computational cost can change non-linearly for different thermodynamic conditions simulated, depending on the relative strength of fluid dynamic pressure (or velocity), viscous dissipation or surface tension effects, that are also correlated with the We_b and Oh_b numbers. When taking into account the different limiting factors of the time step, the spacial resolution criteria defined found in 5.2, as well as the optimal level of parallelization given by the strong-scaling test, it is possible to make a reasonably accurate estimation of the computational cost of each case. The projections are plotted in Fig. B2 as a function of the primary variables R_f^*, p_∞ and T_∞, taking into account the fluid properties given by the EOS and RP-e.

The stepped behaviour of the graphs is partially a result of the necessity to

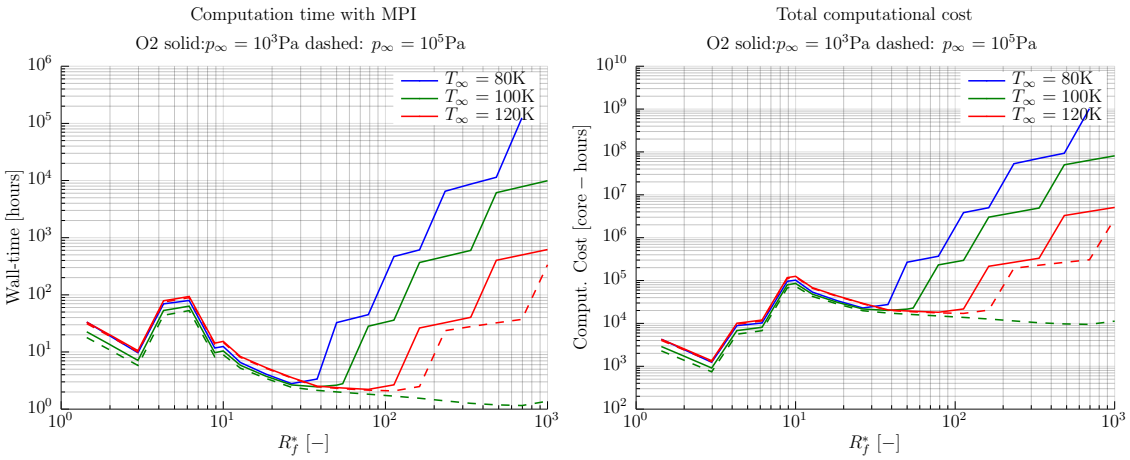

Figure B2: Projections of computational wall-time and total cost for LOx simulations with $N_{\text{bub}} = 125$ and a minimum 64^3 cells per CPU core.

partition the mesh into equal blocks that can be distributed on a discrete number of compute nodes. Cases with $R_f^* < 10$ (Low We_b and high Oh_b) can be simulated in relatively small domains and are sufficiently resolved by 512^3 meshes having a low total computational cost, but a high wall-time due to the dominance of surface tension effects that limit the time step. Cases $10 < R_f^* < 100$ can be simulated relatively quickly (within 24 hours) but require larger domains and more CPU cores resulting in a higher total cost. Here, the flow is controlled by the growth rate of the bubbles and high advection velocities. The cost of cases with higher R_f^*, especially for the lower temperatures, increases rapidly as the flow becomes more complex (turbulent) due to reduced viscous effects. This is determined by the Kolmogorov resolution criterion (Eq. (5.4)) associated with low Oh_b, high Re_b. This range is also associated with aerodynamically driven breakup and has been excluded in this work.

Appendix C

Post-processing and analysis of spray data

Compared to most experimental methods and theoretical models, DNS has the advantage of providing independent measurements of the area and volume of each individual droplet, ligament or other liquid structures. Thus, accurate computations of the spray surface area can be made throughout the whole breakup process. In post-processing of the DNS field data, each droplet and ligament is individually measured in regularly sampled time steps of the simulation. The post-processing algorithm detailed in Sec. C1. The data is then used to compute the statistical results using the various definitions detailed in Sec. C3 as well as the total spray surface area evolution covered in Sec. C4.

C1 Post-Processing algorithm

Post-processing of the DNS field data into spray statistics is done using a purposely developed code `SprayFS3D` written in the `GNU Octave` language [87]. The main algorithm implemented in `SprayFS3D` is adapted from previous works (e.g. [53]) and was extensively modified for computational efficiency and to obtain precise surface area measurements.

The first step is a zone identification process consisting of a domain search in the VOF field to find the limits of continuous regions with $f > 0.01$ that correspond to a droplet or any other liquid structure, providing an identification number i. Cells with $f < 0.01$ are treated as pure vapour. The 0.01 threshold acts as a sharpening effect and helps prevent the influence of numerical noise in the VOF field. For every cell added to droplet i the algorithm verifies the f value of its 6 neighbouring cells, to

which the same i identification value is attributed if containing any amount of liquid. Once no more neighbouring cells containing liquid are found, the program advances to the nearest $f > 0.01$ cell starting the identification process for droplet $i + 1$. The simple recursive algorithm can become highly inefficient for very large droplets. In this work the method was adapted to be used in very large domains with up to 10^9 cells by subdividing the domain in blocks of relatively small size. Each block can be processed independently in sequence or using asyncronous parallelization, at the cost of an additional re-build step that maps continuous liquid structures across the block faces to the same i. Even when implemented in a non-compiled scripting language, the method was effective in processing liquid structures with a number of cells of the order of 1×10^8 as long as memory allocation is strictly minimized to use the only the original data fields (f, a_Γ, etc.) and making use of 3D matrix operations in all computation steps necessary to obtain the properties of each droplet, as follows.

For each identified droplet, i, comprised by n_k cells, we use the VOF field, f, to determine its volume

$$V_i = \sum_{k=1}^{n_k} f_k (\Delta x_k)^3, \tag{C1}$$

and the PLIC-based area using the area density field a_Γ,

$$A_i^{\mathrm{PLIC}} = \sum_{k=1}^{n_k} a_{\Gamma k} (\Delta x_k)^3. \tag{C2}$$

Since the CSS model for surface tension is expected to generate artificial droplets when the distance between two interfaces is less than 4 cells, any identified droplets with a total VoF less than 4^3 are also ignored and treated as vapour in the results presented in this work. For the mesh resolutions used here, this typically accounts for less than 0.1% of the total spray volume. Due to resolution limitations in the PLIC reconstruction and its use of flat planes, the droplet area can be underestimated in locations of high curvature like thin ligaments and poorly resolved small droplets. Thus, a second area measurement is made based on an equivalent ellipsoid that is fitted for each liquid structure, based on its moment of inertia, as described in Sec. C2. The resulting optimized areas A_i together with V_i are used to compute equivalent mean diameters and perform a statistical analysis using the definitions detailed in Sec. C3.

C2 Equivalent ellipsoid

For each droplet the moment of inertia tensor $[I]$ is calculated assuming unitary density using the liquid volumes in each cell, $f_k(\Delta x_k)^3$, and their distance to the droplet's centre of mass (thus given in units of [length]^5). The principal moments of inertia, M_{xx}, M_{yy} and M_{zz}, are calculated by eigendecomposition giving

$$[I] = [R]\,[M]\,[R]^{\mathsf{T}} \tag{C3}$$

where $[M]$ is diagonal matrix containing the principal moments (eigenvalues) and $[R]$ is the rotation matrix, that can be used to reconstruct orientation of the droplets in space. Based on the droplet moment of inertia, the equivalent ellipsoid with the semi-axes a, b, c is given by

$$\begin{aligned} a^2 &= \frac{5\left(-M_{xx} + M_{yy} + M_{zz}\right)}{2V_M}, \\ b^2 &= \frac{5\left(M_{xx} - M_{yy} + M_{zz}\right)}{2V_M}, \\ c^2 &= \frac{5\left(M_{xx} + M_{yy} - M_{zz}\right)}{2V_M} \end{aligned} \tag{C4}$$

and its volume calculated as

$$V_i^{\text{ell}} = \frac{4}{3}\pi abc; \tag{C5}$$

and the area

$$A_i^{\text{ell}} \approx 4\pi \left(\frac{(ab)^{1.6} + (ac)^{1.6} + (bc)^{1.6}}{3} \right)^{1/1.6}, \tag{C6}$$

In Eq. (C4), V_M is the volume of an ellipsoidal droplet that has the same moment of inertia as the original droplet. However, for arbitrarily deformed and slender ligaments, its volume tends to be larger. To recover the original droplet volume, the semi-axis are proportionally scaled to match the real droplet volume, with M_{xx}, M_{yy} and M_{zz} simply providing the relative size between a, b and c. For this, we impose

$$V_i = V_i^{\text{ell}} \Leftrightarrow V_i = \frac{4}{3}\pi abc; \tag{C7}$$

where a, b and c are substituted by Eqs. (C4). The equation is solved for V_M, giving

$$V_M = \frac{5}{2}\left(\frac{\frac{4}{3}\pi L}{V_i} \right)^{2/3}, \tag{C8}$$

where V_i is the original droplet volume based on the VOF field (Eq. (C1)) and L is a purely algebraic auxiliary variable given by

$$L = \sqrt{\left(-M_{xx} + M_{yy} + M_{zz}\right) . \left(M_{xx} - M_{yy} + M_{zz}\right) . \left(M_{xx} + M_{yy} - M_{zz}\right)}, \quad \text{(C9)}$$

with dimensions $\left([\text{length}]^5\right)^{3/2}$. Finally, applying Eqs. (C4) and (C6), we obtain the semi-axis and area of the ellipsoid that has the same volume as the original droplet and a similar aspect ratio that determines its area. This solution tends to underestimate the surface area for highly irregular ligaments or generally convex shapes, but is always larger than (or equal to) the volume based area assuming sphericity ($A_i^V = \left(36\pi V_i^2\right)^{1/3} \leq A_i^{\text{ell}}$).

Considering the advantages and limitations of A_i^{PLIC} and A_i^{ell}, the two are compared for each droplet or liquid region and the larger value is used, ie.,

$$A_i = \max\left\{A_i^{\text{PLIC}}, A_i^{\text{ell}}\right\}. \quad \text{(C10)}$$

This means that an ellipsoidal shape is only assumed when the area is larger than the result given by the PLIC reconstruction (Eq. (C2)), which typically occurs for small, possibly poorly resolved droplets, that also tend to have near spherical shapes due to surface tension. The ellipsoid area is also used in the case of possible unaccounted errors in the PLIC area such as droplets bisected by boundary conditions. In fig. C1 the reconstructed domain based on the reduced data is compared to the original VOF field data. The colour scale represents the ratio between the ellipsoid-based and PLIC-based areas calculated for each droplet.

C3 Weighted average definitions

Using independent measurements of volume V_i and surface area A_i, provided by Eqs. (C1) and (C10), the equivalent diameter of each droplet or liquid structure is defined using the Sauter diameter,

$$D_i = \frac{6V_i}{A_i}, \quad \text{(C11)}$$

which preserves the volume to area ratio of the original droplet. Various averaging methods are used to characterize the mean droplet size. The arithmetic mean of the

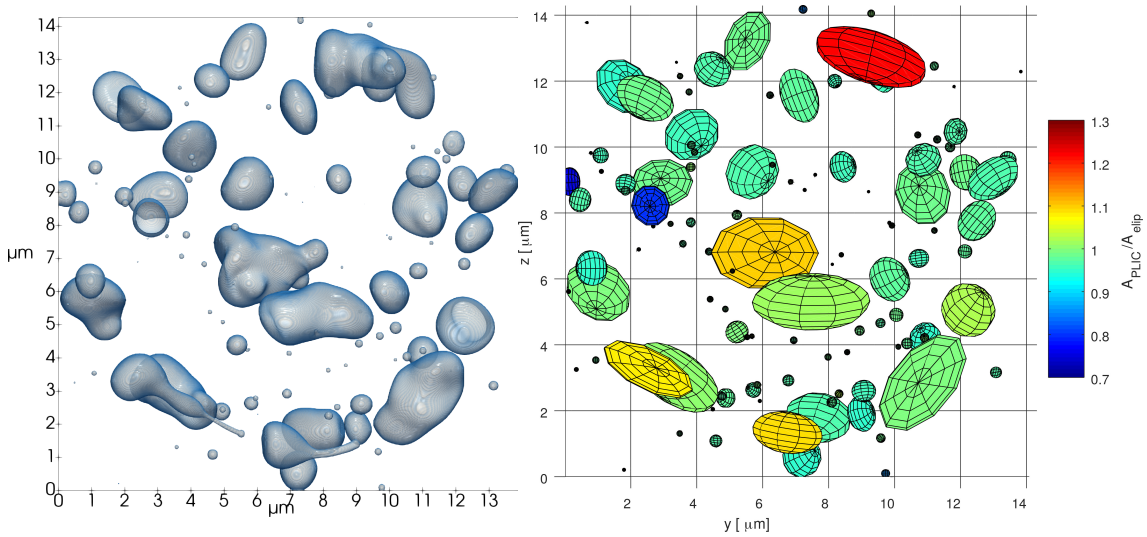

Figure C1: Comparison of the original spray (represented by the f=0.9 iso-surface of the VOF field) with the reduced data represented by equivalent elipsoids. Colour represents the surface area based on PLIC compared to the area of an equivalent ellipsoid. Red/yellow use the PLIC area to compute the equivalent diameter, blue/cyan droplets use the fitted ellipsoid.

droplet diameter is given by

$$\overline{D}_N = \sum_{i=1}^{N} D_i \Big/ N, \tag{C12}$$

with the variance given by

$$\sigma_N^2 = \sum_{i=1}^{N} (D_i - \overline{D}_N)^2 \Big/ N, \tag{C13}$$

Using the area as a weighting factor, we obtain the Sauter mean diameter (SMD)

$$\overline{D}_A = \sum_{i=1}^{N} A_i D_i \Big/ \sum_{i=1}^{N} A_i, \tag{C14}$$

and its variance

$$\sigma_A^2 = \sum_{i=1}^{N} (D_i - \overline{D}_A)^2 A_i \Big/ \sum_{i=1}^{N} A_i. \tag{C15}$$

Finally, the volume (or mass) weighted mean diameter (De Brouckere) is given by,

$$\overline{D}_V = \sum_{i=1}^{N} V_i D_i \Big/ \sum_{i=1}^{N} V_i, \tag{C16}$$

and the volume variance by

$$\sigma_V^2 = \sum_{i=1}^{N} (D_i - \overline{D}_V)^2 V_i \Big/ \sum_{i=1}^{N} V_i. \tag{C17}$$

For each of the variance definitions, the corresponding standard deviation is $\sigma = \sqrt{\sigma^2}$.

It should be noted that when Eq. (C11) is substituted in Eq. (C14), we obtain

$$\overline{D}_A = 6 \sum_{i=1}^{N} V_i \Big/ \sum_{i=1}^{N} A_i, \tag{C18}$$

that is consistent with the physical interpretation of the SMD, as the droplet size with the same volume to area ratio as the entire spray. Using Eq. (C11), an elongated ligament is represented by an equivalent diameter that is generally smaller than a spherical droplet of the same volume. Similarly, liquid structures that are still in the process of breakup are also represented by a diameter that is closer to the mean of the two resulting droplets, having equal contribution to the total spray SMD. This results in a good stability of the results over time and provides good estimates for the mean droplet sizes even while the breakup is not complete.

The arithmetic, Sauter and De Brouckere diameters are often noted as $\overline{D}_{10}$, $\overline{D}_{32}$ and $\overline{D}_{43}$, respectively, where the subscripts denote the powers of the sampled droplet diameters instead of explicit weighting factors

$$\overline{D}_{lk} = \left(\sum_{i=1}^{N} D_i^l \Big/ \sum_{i=1}^{N} D_i^k \right)^{\frac{1}{l-k}}. \tag{C19}$$

These are typically used when droplet sphericity is assumed ($D_i = \sqrt[3]{\frac{6}{\pi} V_i}$) and can be interpreted as approximate values for the (exact) $\overline{D}_N$, $\overline{D}_A$ and $\overline{D}_V$ means.

C4 Evolution of surface area

The temporal evolution of the breakup process shall also be analysed in terms of total surface area generated. For this, the ratio of surface area to liquid volume is defined as

$$\gamma = \sum_{i=1}^{N} A_i \Big/ \sum_{i=1}^{N} V_i, \tag{C20}$$

where N is the total number of droplets or any continuous liquid region identified in the domain, with the respective volume and area again given by Eqs. (C1) and (C10).

For comparison of the various cases, the normalized variable

$$\gamma^* = \gamma/\gamma_{R_f} \tag{C21}$$

can be used, where the reference value, γ_{R_f}, is a purely geometric constant determined for each case representing surface area to volume ratio assuming spherical bubbles of radius R_f at the moment of coalescence. It is given by

$$\gamma_{R_f} = \frac{4\pi R_f^2}{\frac{V_0}{N_{\text{bub}}} - \frac{4}{3}\pi R_f^3 \frac{\rho_v}{\rho_\ell}}, \tag{C22}$$

where the denominator accounts for the initial liquid volume minus the volume consumed to generate the vapour. The expression simplifies to a function of the final void fraction, η_f, viz.

$$\gamma_{R_f} = \frac{3}{R_f\left(\frac{1}{\eta_f} - 1\right)} \approx 3.30 R_f^{-1} \tag{C23}$$

where V_0 is replaced by Eq. (4.17) and $\eta_f = \pi/6$ in the approximated result.

Another reference value based on the setup parameters is $\dot{\gamma}_{R_f}$, i.e. an analytical estimator for the rate of surface area generation, that is the time derivative of the

geometric γ_{R_f}. It can be derived as

$$\begin{aligned}
\dot{\gamma}_{R_f} &\equiv \left.\frac{\mathrm{d}\gamma}{\mathrm{d}t}\right|_{R=R_f} \\
&= \left.\frac{\mathrm{d}\gamma}{\mathrm{d}R}\cdot\frac{\mathrm{d}R}{\mathrm{d}t}\right|_{R=R_f} \\
&= \frac{N_{\mathrm{bub}}\cdot 4\pi R_f\left(2V_0 + N_{\mathrm{bub}}\cdot\frac{4}{3}\pi R_f^3\frac{\rho_v}{\rho_\ell}\right)}{\left(V_0 - N_{\mathrm{bub}}\cdot\frac{4}{3}\pi R_f^3\frac{\rho_v}{\rho_\ell}\right)^2}\cdot\dot{R} \\
&= \frac{6\left(\frac{1}{\eta_f}-1\right)+9\frac{\rho_v}{\rho_\ell}}{R_f^2\left(\frac{1}{\eta_f}-1\right)^2}\cdot\dot{R},
\end{aligned} \tag{C24}$$

where γ_{R_f} is given by Eq. (C22) and the simplified expression is obtained by substituting the constant V_0 with Eq. (4.17). In this work $\eta_f = \pi/6$ is generally assumed. While γ_{R_f} is a purely geometric parameter, $\dot{\gamma}_{R_f}$ depends on the bubble growth rate determined for each case. However, it does not yet take into account the effect of bubble non-sphericity, surface tension or We_b and Oh_b numbers.

Appendix D

List of case setup parameters

The complete list of case setup parameters is provided here. It includes thermodynamic properties calibrated for each R_f^* value according to the RP-e solution and corresponding dimensionless numbers and other relevant variables. Geometric domain parameters according to Sec. 4.2 are also provided, as well as mesh size and resolution factors according to Sec. 5.2. Table D1 covers the series of cases in cubic-lattice array arrangement presented in Sec. 5.1. For the simulations presented in Sec. 5.2.1, the setup parameters are identical to case A-50 of Tab. D1, except for the (variable) mesh resolution factors. Table D2 covers the series of cases in cubic-lattice array arrangement presented in Sec. 5.3.

Table D1: Complete setup parameters for cases in cubic-lattice array arrangement.

DNS case	A-2 Array	A-5 Array	A-10 Array	A-50 Array	C-2 Array	C-5 Array	C-10 Array
p_∞ [Pa]	10^3	10^3	10^3	10^3	10^3	10^3	10^3
T_∞ [K]	120	120	120	120	80	80	80
R_f^*	2	5	10	50	2	5	10
R_f [µm]	0.024 04	0.0601	0.1202	0.601	2.161	5.404	10.81
t_f [µs]	0.002 735	0.003 993	0.007 125	0.036 69	1.074	1.783	3.3
$t_f^{\text{RP-e}}$ [µs]	0.004 026	0.0068	0.010 41	0.038 32	1.439	2.657	4.35
$\dot{R}$ [m/s]	8.789	15.05	16.87	16.38	2.012	3.03	3.276
σ [N/m]	0.006 599	0.007 288	0.007 848	0.009 233	0.015 85	0.016 01	0.016 15
ρ_v [kg/m^3]	34.76	28.84	24.71	16.6	1.388	1.284	1.2
ρ_ℓ [kg/m^3]	968	968	968	968	1190	1190	1190
μ_v [µPas]	9.234	8.958	8.744	8.241	6.113	6.065	6.023
μ_ℓ [µPas]	95.52	95.52	95.52	95.52	261.1	261.1	261.1
We_b [−]	0.54	3.62	8.44	33.80	1.31	7.38	17.10
Oh_b [−]	0.17	0.10	0.07	0.03	0.03	0.02	0.01
Re_b [−]	4.283	18.34	41.1	199.5	39.64	149.3	322.8
$\text{Re}_{b,v}$ [−]	1.591	5.826	11.46	39.65	1.974	6.93	14.11
η_K [µm]	0.016 15	0.013 56	0.014 81	0.022 64	0.2736	0.2531	0.2838
$\eta_{\text{K},v}$ [µm]	0.033 95	0.032 05	0.038 59	0.076 07	2.596	2.53	2.969
D_ref [µm]	0.706	0.2658	0.2279	0.2845	26.33	11.72	10.11
N_bub [#]	125	125	125	125	125	125	125
n [#/m^3]	1.82×10^{22}	1.17×10^{21}	1.47×10^{20}	1.19×10^{18}	2.60×10^{16}	1.66×10^{15}	2.07×10^{14}
V_0 [m^3]	6.88×10^{-21}	1.068×10^{-19}	8.506×10^{-19}	1.054×10^{-16}	4.814×10^{-15}	7.527×10^{-14}	6.025×10^{-13}
V_f [m^3]	1.389×10^{-20}	2.171×10^{-19}	1.737×10^{-18}	2.171×10^{-16}	1.009×10^{-14}	1.578×10^{-13}	1.263×10^{-12}
Δt [ns]	0.000 906 5	0.004 846	0.017 02	0.1064	0.4419	2.575	9.695
Δx [nm]	1.202	3.005	6.01	19.37	108.1	270.2	540.4
$N_{\Delta x}$ [#]	256^3	256^3	256^3	1024^3	256^3	256^3	512^3
$R_f/\Delta x$ [#]	20	20	20	31.03	20	20	20
$D_\text{ref}/\Delta x$ [#]	587.4	88.45	37.91	14.69	243.6	43.39	18.71
$\eta_\text{K}/\Delta x$ [#]	13.44	4.514	2.464	1.169	2.532	0.9367	0.5253

Table D2: Complete setup parameters for cases in randomized cluster arrangement.

DNS case	A-2	A-5	A-10	A-16	A-50	B-2	B-10	C-2	C-5	D-2	D-10	D-50
p_∞ [Pa]	10^3	10^3	10^3	10^3	10^3	10^3	10^3	10^3	10^3	10^5	10^5	10^5
T_∞ [K]	120	120	120	120	120	100	100	80	80	100	100	100
R_f^*	2	5	10	16	50	2	10	2	5	2	10	50
R_f [µm]	0.024 04	0.0601	0.1202	0.1923	0.601	0.1697	0.8487	2.161	5.404	0.2788	1.394	6.971
t_f [µs]	0.002 735	0.003 993	0.007 125	0.011 17	0.036 69	0.032 12	0.094 76	1.074	1.783	0.075 41	0.2469	1.631
$t_f^{\text{RP-e}}$ [µs]	0.004 026	0.0068	0.010 41	0.014 52	0.038 32	0.044 43	0.1282	1.439	2.657	0.1018	0.3099	1.446
$\dot{R}$ [m/s]	8.79	15.05	16.87	17.21	16.38	5.283	8.956	2.012	3.03	3.697	5.646	4.274
σ [N/m]	0.006 599	0.007 288	0.007 848	0.008 242	0.009 233	0.011 06	0.011 81	0.015 85	0.016 01	0.011 08	0.011 83	0.012 58
ρ_v [kg/m^3]	34.76	28.84	24.71	22.12	16.6	9.385	7.264	1.388	1.284	9.307	7.212	5.531
ρ_ℓ [kg/m^3]	968	968	968	968	968	1090	1090	1190	1190	1090	1090	1090
μ_v [µPas]	9.234	8.958	8.744	8.597	8.241	7.622	7.375	6.113	6.065	7.613	7.368	7.13
μ_ℓ [µPas]	95.52	95.52	95.52	95.52	95.52	152.1	152.1	261.1	261.1	152.3	152.3	152.3
We_b [−]	0.54	3.62	8.44	13.38	33.80	0.93	12.56	1.31	7.38	0.75	8.19	22.08
Oh_b [−]	0.17	0.10	0.07	0.05	0.03	0.08	0.03	0.03	0.02	0.06	0.03	0.01
Re_b [−]	4.283	18.34	41.1	67.08	199.5	12.85	108.9	39.64	149.3	14.76	112.7	426.7
$\text{Re}_{b,v}$ [−]	1.591	5.826	11.46	17.03	39.65	2.208	14.97	1.974	6.93	2.52	15.41	46.22
η_K [µm]	0.016 15	0.013 56	0.014 81	0.016 41	0.022 64	0.050 01	0.050 33	0.2736	0.2531	0.074 05	0.080 59	0.1485
$\eta_{\text{K},v}$ [µm]	0.033 94	0.032 05	0.038 59	0.045 88	0.076 07	0.1874	0.223	2.596	2.53	0.2788	0.3585	0.7865
D_ref [µm]	0.7059	0.2658	0.2279	0.23	0.2845	2.907	1.081	26.33	11.72	5.95	2.723	5.051
N_bub [#]	1000	512	512	125	125	1000	512	1000	512	1000	512	125
n [#/m^3]	1.82×10^{22}	1.17×10^{21}	1.47×10^{20}	3.60×10^{19}	1.19×10^{18}	5.32×10^{19}	4.26×10^{17}	2.60×10^{16}	1.66×10^{15}	1.20×10^{19}	9.62×10^{16}	7.70×10^{14}
V_0 [m^3]	5.504×10^{-20}	4.375×10^{-19}	3.484×10^{-18}	3.473×10^{-18}	1.054×10^{-16}	1.88×10^{-17}	1.202×10^{-15}	3.851×10^{-14}	3.083×10^{-13}	8.337×10^{-17}	5.324×10^{-15}	1.623×10^{-13}
V_f [m^3]	1.111×10^{-19}	8.892×10^{-19}	7.113×10^{-18}	7.111×10^{-18}	2.171×10^{-16}	3.91×10^{-17}	2.504×10^{-15}	8.073×10^{-14}	6.464×10^{-13}	1.734×10^{-16}	1.11×10^{-14}	3.388×10^{-13}
Δt [ns]	0.003 626	0.008 615	0.017 02	0.017 63	0.1101	0.059 12	0.2665	1.768	4.578	0.1584	0.6945	4.893
Δx [nm]	2.404	4.007	6.01	6.411	20.03	16.97	42.43	216.1	360.2	27.88	69.71	232.4
$N_{\Delta x}$ [#]	512^3	1024^3	1024^3	1024^3	1024^3	512^3	1024^3	512^3	1024^3	512^3	1024^3	1024^3
$R_f/\Delta x$ [#]	10	15	20	30	30	10	20	10	15	10	20	30
$D_\text{ref}/\Delta x$ [#]	293.6	66.34	37.91	35.88	14.2	171.3	25.47	121.8	32.54	213.4	39.07	21.74
$\eta_\text{K}/\Delta x$ [#]	6.718	3.385	2.464	2.56	1.13	2.946	1.186	1.266	0.7025	2.656	1.156	0.6391
Cost [core-hours]	2.0×10^4	1.1×10^5	1.1×10^5	1.8×10^5	2.2×10^5	1.7×10^4	4.6×10^5	2.3×10^4	3.0×10^5	1.5×10^4	3.3×10^5	3.7×10^5

Appendix E

Reference data for relevant cryogenic fluids

Solutions for the RP-e model, dimensionless numbers and DNS-fitted models are provided here for additional cryogenic fluids, that are typically used as rocket propellants or surrogates. It includes O_2 (Fig. E1), N_2 (Fig. E2), CH_4 (Fig. E3) and H_2 (Fig. E4) as well as water (Fig. E5) for comparative purposes. These are procedurally generated for a range of temperatures between their respective critical and triple points and pressures ranging from ambient, to low-vacuum of 1000 Pa (10 mbar) or otherwise limited to a value close to triple-point pressure. The critical radius R_{crit}, can be inferred from the starting point of each curve. Intermediate thermodynamic variables such as σ and ρ_v are omitted for brevity, but can be immediately obtained via an EOS assuming saturation conditions for a given $T_\Gamma(R)$. The We_b and Oh_b numbers are given as functions of R_f, in line to the approach described in Sec. 4.2, which can be directly correlated with the nuclei number density, n, via Eq. (4.18). The DNS-fitted models for D_A^{fit} (representative of the spray SMD) and peak surface area generation rate $\dot{\gamma}_{\mathrm{max}}^{\mathrm{fit}}$, are given respectively equations by Eqs. (5.7) and (5.8), when evaluated according to the fluid's We_b curve.

The limited data provided for H_2, is due to deficiencies on the procedurally generated database of RP-e solutions, that requires some estimation of initialization parameters for the numerical solution, which is is not always successful.

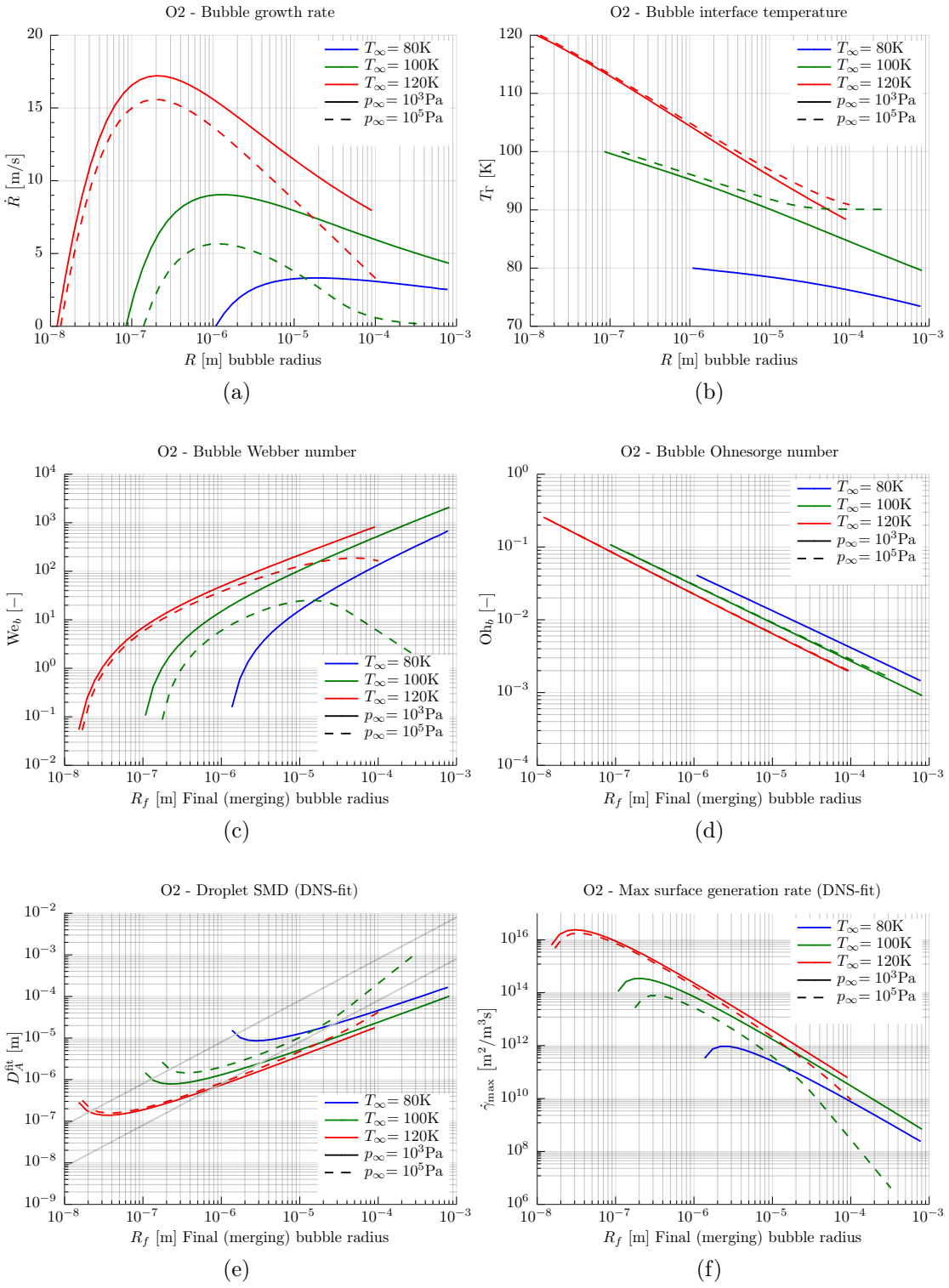

Figure E1: Results of the RP-e model and fitted models for Liquid Oxygen (O_2).

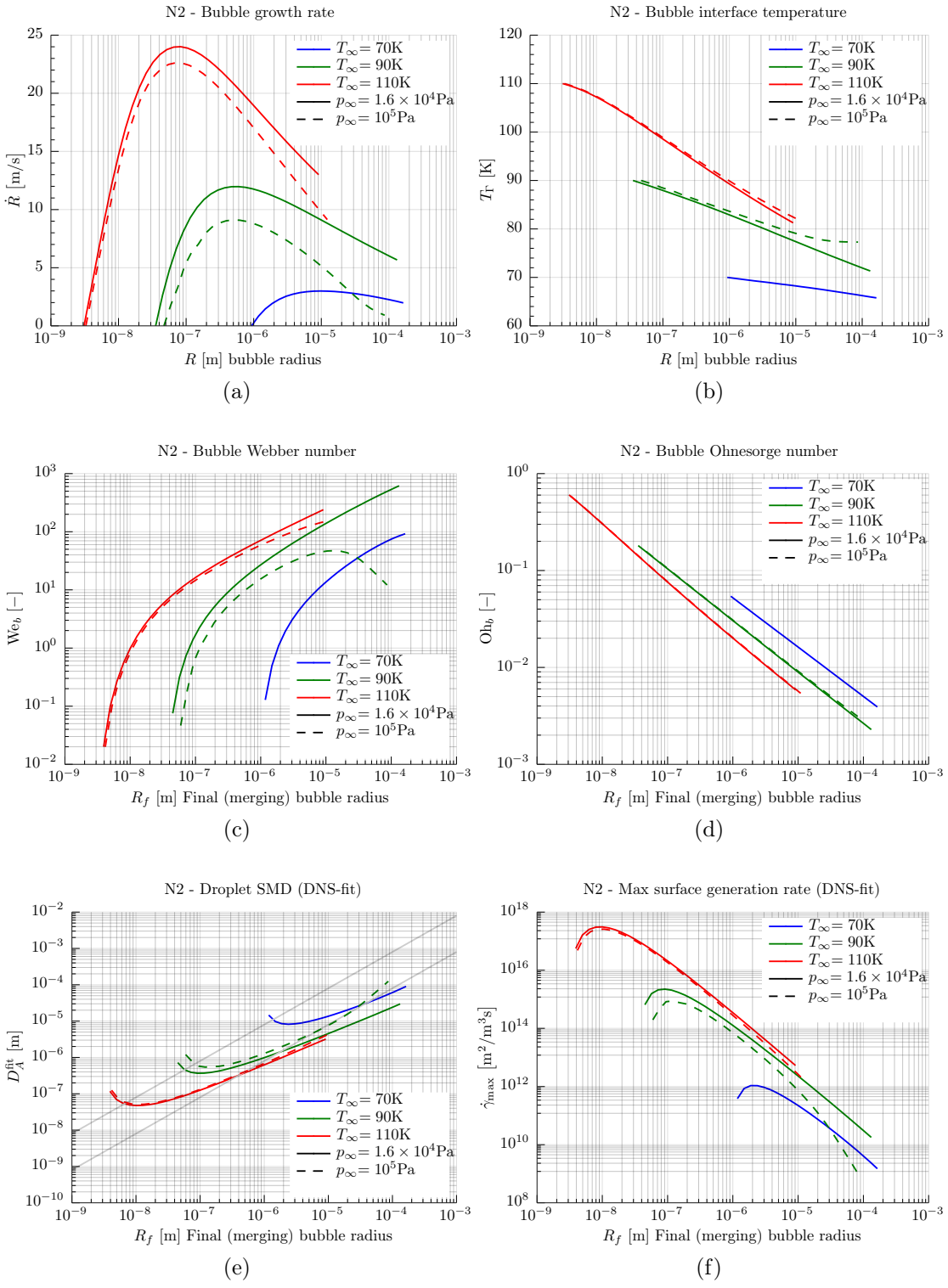

Figure E2: Results of the RP-e model and fitted models for Liquid Nitrogen (N_2).

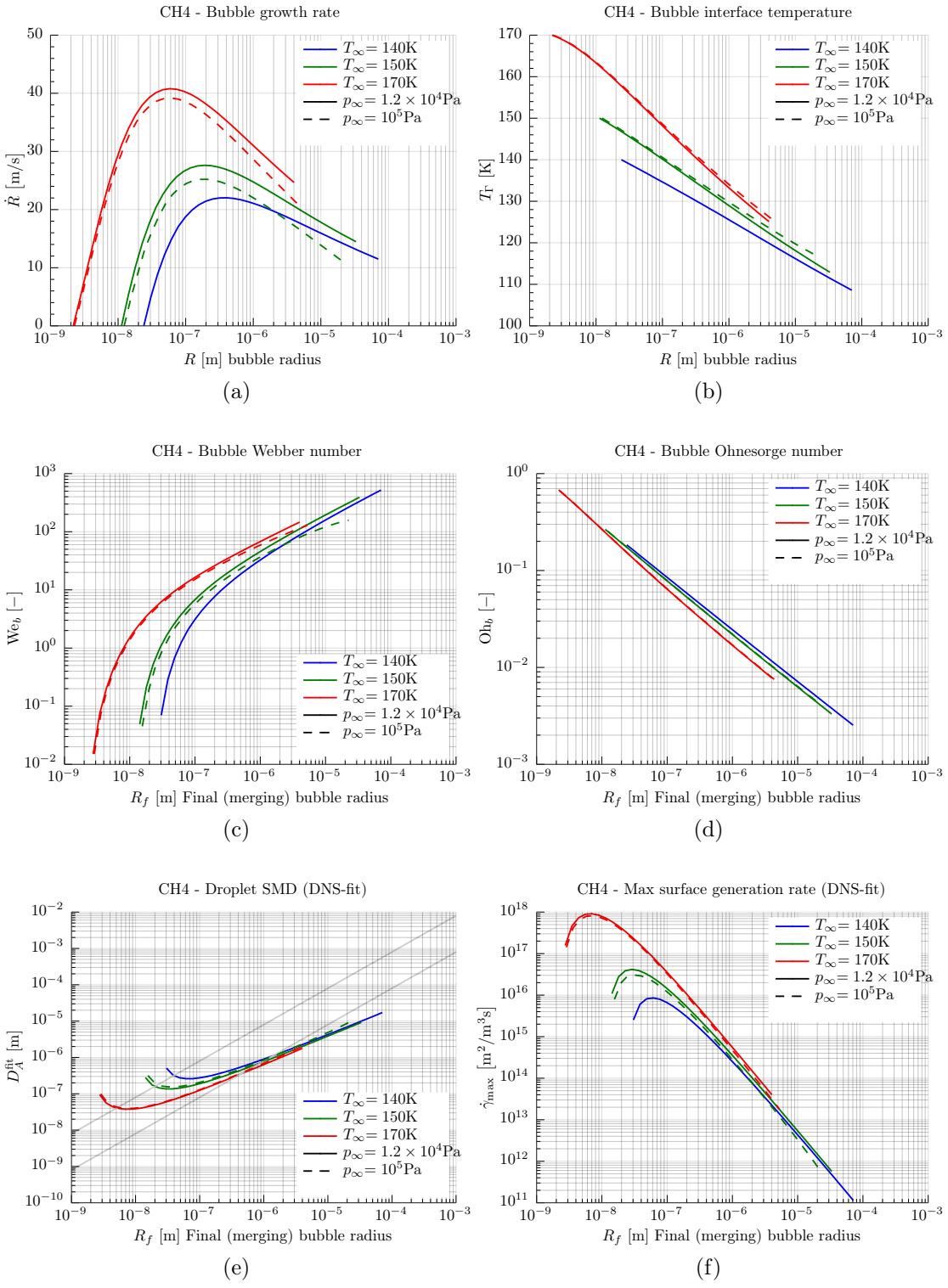

Figure E3: Results of the RP-e model and fitted models for Liquid Methane (CH_4).

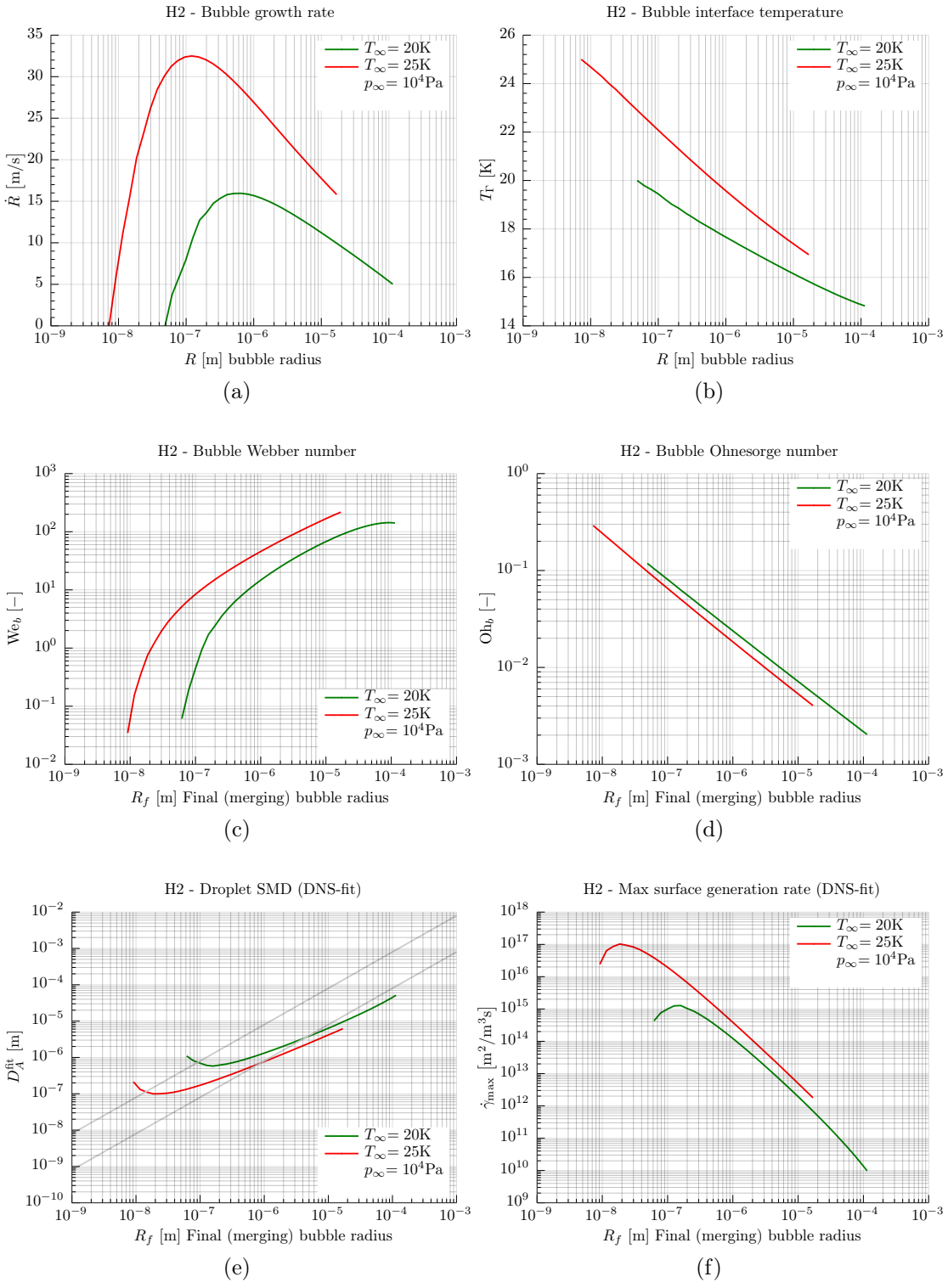

Figure E4: Results of the RP-e model and fitted models for Liquid Hydrogen (H_2) .

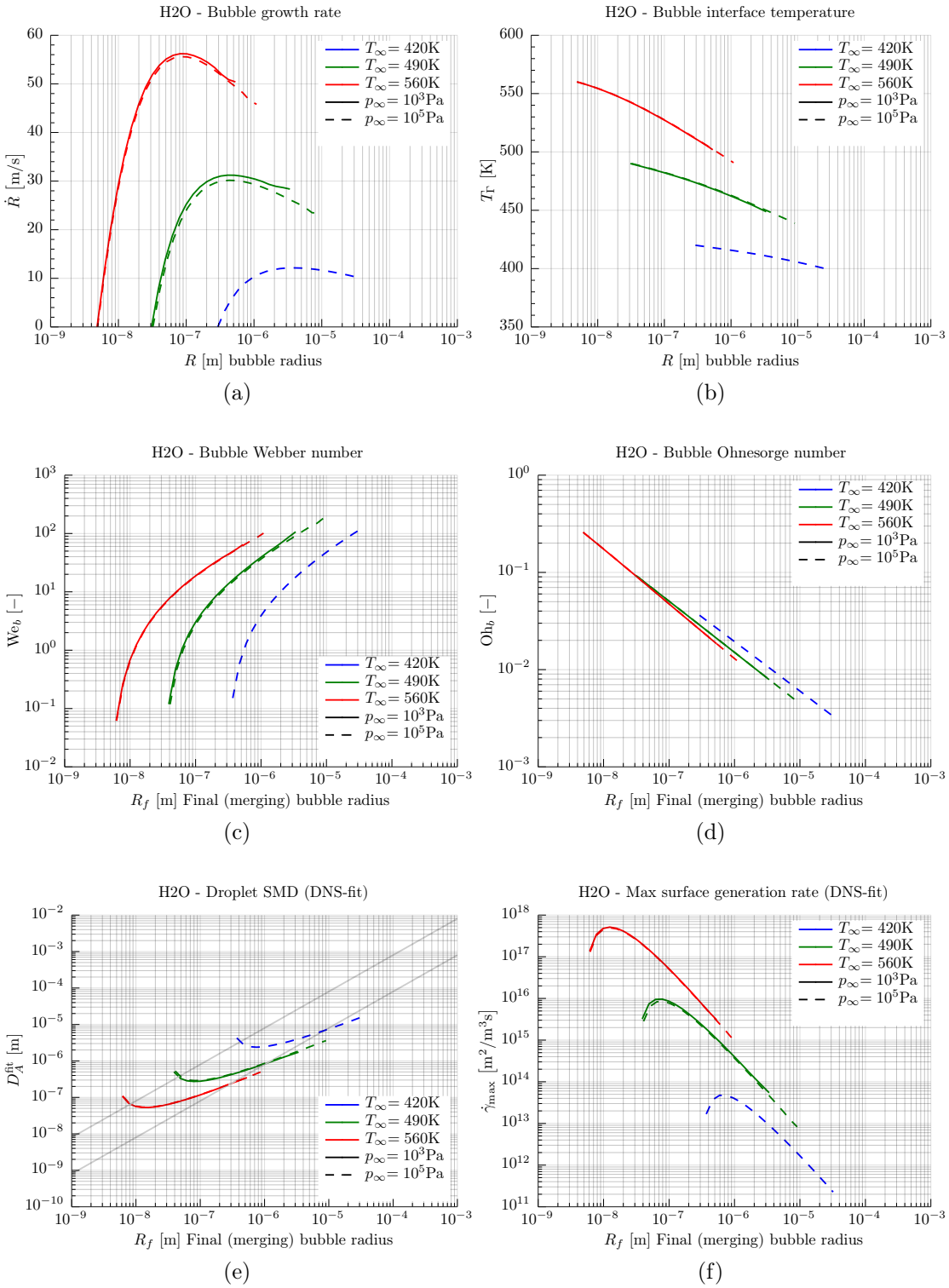

Figure E5: Results of the RP-e model and fitted models for Water (H_2O).

Appendix F

Data storage

The case data for the results presented in this work is stored on the ITV storage repository, under the path `/itv/storage/ITV-DATABASE/ITV/PUBLICATIONS/...`, in accordance to the respective publications as detailed in the following tables. The source files and documentation for each publication is provided in repositories hosted on the `GitHub` server of Uni-Stuttgart. The various codes and scripts employed on all publications are also stored on independent `GitHub` repositories with detailed revision history. In addition the particular revision of the main DNS code directly provided below for each publication, their documentation points to the appropriate revisions of the pre- and post-processing codes listed in Table F6.

Table F1: Case and code used to produce results of Loureiro et al. [1]. The corresponding publication repository is `GitHub/ITV/2018_Loureiro_ICLASS.`

2018_Loureiro_ICLASS		
Data on storage	Case	Code:tag (SHA)
`/CONFERENCE/2018_Loureiro_ICLASS/`	All cases	`FS3D:ICLASS18/D2.3 (#c59a5fd2)`

Table F2: Case and code used to produce results of Loureiro et al. [2]. The corresponding publication repository is `GitHub/ITV/2019_Loureiro_ICMF.`

2019_Loureiro_ICMF		
Data on storage	Case	Code:tag (SHA)
`/CONFERENCE/2019_Loureiro_ICMF/`	All cases	`FS3D:ICMF/D2.4 (#e3dcc6f4)`

Table F3: Case and code used to produce results of Loureiro et al. [3] (subm. 2019). The corresponding publication repository is `GitHub/ITV/2021_Loureiro_HLRS.`

2021_Loureiro_HLRS		
Data on storage	Case	Code:tag (SHA)
`/JOURNAL/2021_Loureiro_HLRS/`	Mesh study	`FS3D:ICMF/D2.4 (#e3dcc6f4)`
`/JOURNAL/2021_Loureiro_HLRS/ HLRS20_Scaling/`	Strong scaling	`FS3D:ICMF/D2.4 (#e3dcc6f4)`

Table F4: Case and code used to produce results of Loureiro et al. [4]. The corresponding publication repository is `GitHub/ITV/2020_Loureiro_IJMF.`

2020_Loureiro_IJMF		
Data on storage	Case	Code:tag (SHA)
`/JOURNAL/2020_Loureiro_IJMF/`	All cases	`FS3D:IJMF-1 (#28186b45)`

Table F5: Case and code used to produce results of Loureiro et al. [5]. The corresponding publication repository is `GitHub/ITV/2021_Loureiro_IJMF.`

2021_Loureiro_IJMF		
Data on storage	Case	Code:tag (SHA)
`/JOURNAL/2021_Loureiro_IJMF/`	All cases	`FS3D:IJMF-2 (#a42f1c4)`

Table F6: Pre- and Post-processing codes used to setup and process the DNS data.

Post-processing codes		
Code	Location	Purpose
`SprayFS3D`	`Gihub/FS3Dspray`	Post-processing of raw HDF data into individual droplet data and spray statistics.
`metaEOS`	`Gihub/metaEOS`	Wrapper for CoolProp [62], fluid properties and equation of state data.
`FlEDGe`	`Gihub/fledge`	Database generator for RP-e data using the `rayleigh-plesset`[70] code.
`Vary`	`Gihub/vary`	Tool for scripting, parametric studies, managing and displaying data with multiple degrees of freedom. Automation for plots, tables and unit conversions.